Development of an Airborne Ka-Band FM-CW Synthetic Aperture Radar

Development of an Airborne Ka-Band FM-CW Synthetic Aperture Radar

Proefschrift

ter verkrijging van de graad van doctor
aan de Technische Universiteit Delft,
op gezag van de Rector Magnificus prof. dr. ir. J. T. Fokkema,
voorzitter van het College voor Promoties,
in het openbaar te verdedigen op maandag 9 mei 2005 om 15.30 uur
door Jacobus Johannes Maria DE WIT
elektrotechnisch ingenieur
geboren te Lopik.

Dit proefschrift is goedgekeurd door de promotoren:

Prof. ir. P. Hoogeboom
Prof. dr. ir. L. P. Ligthart

Samenstelling promotiecommissie:

Rector Magnificus,	voorzitter
Prof. ir. P. Hoogeboom,	Technische Universiteit Delft, promotor
Prof. dr. ir. L. P. Ligthart,	Technische Universiteit Delft, promotor
Prof. dr. ir. P. M. Dewilde,	Technische Universiteit Delft
Prof. Dr.-Ing.habil A. Moreira,	DLR Institut für Hochfrequenztechnik und Radarsysteme
Prof. dr. ir. M. H. G. Verhaegen,	Technische Universiteit Delft
Dr. W. L. van Rossum,	TNO Defensie en Veiligheid

This research was supported by the Technology Foundation STW, applied science division NWO and the technology programme of the Ministry of Economic Affairs. The project was granted under number DTC.5642.
The work was furthermore supported by TNO Defence, Security, and Safety.

The excerpt on page v is taken from:
Desiderius Erasmus, "De lof der zotheid," translated from Latin by A. Dirkzwager and A. C. Nielson, Rotterdam: Uitgeverij Ad. Donker, 1993.
Reproduced with persmission.

ISBN 90-9019360-X

Want zij die bijvoorbeeld een proefschrift schrijven, dat immers alleen bestemd is om aan het oordeel van enige professoren te worden onderworpen, en die de strengste en meest deskundige critici niet vrezen, zijn, dunkt me, meer te beklagen dan te benijden, daar ze zich eindeloos aftobben. Ze voegen toe, veranderen, schrappen, herstellen weer, herzien, werken het weer geheel en al om, laten het graag anderen zien, houden het negen jaar in portefeuille en zijn nooit tevreden met het resultaat. De beloning, die ze er tenslotte voor krijgen –immers de lof van een enkeling– is wel heel duur betaald met al hun zwoegen, zweten en gebrek aan het zoetste, wat er bestaat: de slaap. Voeg hierbij nog dat dit alles gaat ten koste van hun gezondheid, dat ze daardoor humeurig. lelijk, bijziende of zelfs blind worden, tot armoede vervallen, bij ieder uit de gunst zijn, dat ze alle genoegens moeten verzaken, dat ze vóór hun tijd oud zijn, ontijdig sterven en wat dies meer zij.

Doch al deze opofferingen getroosten zij zich gaarne om de goedkeuring weg te dragen van één of twee geleerde boekenwurmen.

De lof der zotheid – Desiderius Erasmus

To my parents.

Contents

Samenvatting

Ontwikkeling van een Ka-band FM-CW synthetische apertuur radar

In het vakgebied van de aardobservatie bestaat er een groeiende behoefte aan kleine en goedkope observatiesensoren van hoge resolutie. Zulke sensoren kunnen een belangrijke rol spelen in kleinschalige *remote sensing* toepassingen, zoals het observeren van rivieren en dijken, snelwegen, of gebieden waarin gaspijpen liggen.
Om succesvol te worden, moeten zulke sensors weinig vermogen verbruiken en licht en compact zijn zodat ze gedragen kunnen worden door kleine, mogelijk zelfs onbemande, vliegtuigen. Bovendien moeten ze goedkoop zijn in aanschaf, gebruik en onderhoud om interessant te zijn voor de civiele markt.
Een belangrijk nadeel van radarsystemen is dat de resolutie dwars op de kijkrichting, de azimut resolutie, slechter wordt met de afstand. Dit komt doordat de breedte van de antennebundel toeneemt met toenemende afstand. Om toch een goede azimut resolutie te verkrijgen moeten *synthetische apertuur radar* (SAR) technieken toegepast worden. Zulke technieken worden al met succes toegepast in de radaraardobservatie met coherente pulsradars. Pulsradars zijn over het algemeen echter complexe en relatief dure systemen die daarom minder geschikt zijn voor gebruik aan boord van kleine vliegtuigen of voor kleinschalige toepassingen.
Frequency modulated continuous wave (FM-CW) radarsystemen verbruiken slechts een bescheiden vermogen en bestaan gewoonlijk uit een beperkt aantal simpele en compacte onderdelen. Een FM-CW SAR systeem zou de voordelen van FM-CW radartechnologie en SAR signaalverwerkingstechnieken moeten combineren, resulterend in een goedkope en compacte observatiesensor van hoge resolutie. Desondanks is vliegtuig-SAR een nieuwe toepassing voor FM-CW radars.
Ondanks het feit dat SAR technieken al succesvol toegepast worden met behulp van pulsradars, staat de bruikbaarheid van FM-CW SAR niet vast. In puls SAR signaalverwerking wordt normaal gesproken aangenomen dat het radarplatform stationair is gedurende het uitzenden van een puls en het ontvangen van de bijbehorende echo. Deze zogenaamde *hollen-of-stilstaan* aanname is geldig omdat de uitgezonden pulsen zeer kort zijn. Omdat FM-CW radars relatief lange frequentiezwaaien uitzenden is de hollen-of-stilstaan aanname niet langer geldig en moet de beweging van het radarplatform tijdens het zenden en ontvangen in rekening gebracht worden.
Het effect van de platformbeweging is onderzocht door de responsie van een FM-CW SAR systeem op een enkel stationair puntdoel af te leiden. Deze afleiding toont aan dat de plat-

formbeweging leidt tot een Doppler-frequentieverschuiving gedurende de SAR observatietijd. Door de afstandsmigratie-compensatie aan te passen kan de frequentieverschuiving tegelijkertijd gecompenseerd worden.
Om de bruikbaarheid van FM-CW SAR in operationele omstandigheden te bewijzen is er een volledig operationeel demonstratiesysteem ontwikkeld. Daarnaast moet het demonstratiesysteem aantonen dat een FM-CW SAR systeem inderdaad op een efficiënte en goedkope manier aangewend kan worden.
De Stemme S10 motorzwever is een klein, relatief goedkoop testplatform. Het ontwerp van het demonstratiesysteem is daarom afgestemd op dit zweefvliegtuig. Voor de Stemme zweefvlieger zijn gestandaardiseerde gondels beschikbaar die onder de vleugels gemonteerd kunnen worden. Deze gondels hebben een diameter van ongeveer 35 cm en ze zijn zo'n 80 cm lang. Het complete demonstratiesysteem is in zo'n gondel geïnstalleerd.
Het hart van het demonstratiesysteem is de 35 GHz FM-CW radar gefabriceerd door Epsilon-Lambda Electronics. Een voorlopige analyse wees uit dat de gevoeligheid van de radar niet goed genoeg zou zijn om SAR beelden van een hoge kwaliteit te kunnen maken. Niettemin zou het maken van een SAR beeld met behulp van radarreflectoren mogelijk moeten zijn. Een scherp SAR beeld van een aantal reflectoren zou genoeg zijn om aan te tonen dat FM-CW SAR een bruikbaar concept is. Daarom is het radarsysteem toch aangeschaft, ook omdat er geen andere kandidaten beschikbaar waren.
Het demonstratiesysteem is uitvoerig getest tijdens de zomer van 2003 en de lente van 2004. De resultaten van deze tests wezen uit dat de gemeten signaal-ruis verhouding (SNR) achterbleef bij de verwachte SNR. De precieze oorzaak kon niet vastgesteld worden, voornamelijk doordat de benodigde 35 GHz meetapparatuur niet voorhanden was. De gemeten resultaten bevestigden wel dat het mogelijk moest zijn SAR beelden te maken met behulp van radarreflectoren. Een vliegtuigcampagne werd daarom voorbereid.
Een succesvolle vliegtuigcampagne werd uitgevoerd op het vliegveld van Strausberg vlakbij Berlijn in juni 2004. Naast de start- en landingsbaan werden vier reflectoren opgesteld. Een aantal meetvluchten werd gemaakt parallel aan de start- en landingbaan op verschillende vlieghoogten. Een SAR beeld van acceptabele kwaliteit kon gemaakt worden met behulp van data gemeten tijdens een meetvlucht op 100 m hoogte.
De succesvolle vliegtuigcampagne heeft bewezen dat FM-CW SAR een bruikbaar en praktisch toepasbaar concept is. Bovendien heeft de campagne aangetoond dat een FM-CW SAR systeem inderdaad op een efficiënte en goedkope manier toegepast kan worden vanaf een relatief klein vliegtuig.

J. J. M. de Wit

Summary

Development of an Airborne Ka-band FM-CW Synthetic Aperture Radar

In the field of airborne earth observation there is a special interest in lightweight, low cost imaging radars of high resolution. Such radar systems could play an essential role in small-scale earth observation applications such as the monitoring of dikes, watercourses or areas in which gas pipes or electrical power lines are buried. In order to be successful, such systems should consume little power and they should be small enough to be mounted on very small airborne platforms. Moreover, in order to be of interest to the civil market, cost effectiveness is mandatory. The novel combination of compact *frequency modulated continuous wave* (FM-CW) radar technology and high resolution *synthetic aperture radar* (SAR) processing techniques should pave the way for the development of such a small and cost effective imaging radar.

Although SAR techniques have already been successfully applied to coherent pulse radars, the practicability of FM-CW SAR is not evident. In pulse SAR signal processing it is assumed that the radar platform is stationary throughout the transmission of a pulse and the reception of the corresponding echo. This so-called *stop-and-go* approximation is valid since the transmitted pulses are very short. FM-CW radars transmit relatively long sweeps which is why the stop-and-go approximation may no longer be valid. In that case, the change of range during the transmission of a sweep and the reception of the corresponding echo should be taken into account.

The effect of the continuous platform motion is investigated by deriving the response of an FM-CW SAR system to a single stationary point target. This investigation shows that the platform motion induces a Doppler frequency shift throughout the SAR observation time. A modification to the range migration compensation is proposed to compensate the Doppler frequency shift at the same time.

In order to show the practicability of FM-CW SAR under operational circumstances, a fully operational airborne demonstrator system has been developed. Additionally, the demonstrator system should prove that an FM-CW SAR system can indeed be operated in an efficient and cost effective manner from a small platform.

The Stemme S10 motor glider provides a relatively cheap test platform. Therefore, the demonstrator system is tailored to this glider. For the Stemme glider standardized under wing pods are available. These pods have a diameter of about 35 cm and an effective length of around 80 cm. The complete demonstrator system has been fitted in such a pod.

The core of the demonstrator system is the 35 GHz FM-CW front end manufactured by

Epsilon-Lambda Electronics Inc. Other manufacturers were approached as well, but they were not prepared to build a single customized front end. A preliminary performance analysis showed that the sensitivity of the front end would not be sufficient to produce high quality SAR images of areas with a low radar cross section (RCS) per unit area. Nevertheless, SAR imaging by using radar reflectors that have a large RCS should be feasible. A well-focused airborne SAR image of several radar reflectors would suffice for at least a proof of principle. Therefore, it was decided to purchase the front end, also because no other candidates were available.

The complete system set up was put to the test during thorough ground-based measurements in the late summer of 2003 and early spring of 2004. The results obtained throughout these measurements showed that the measured signal-to-noise ratio (SNR) lagged behind the expected SNR. The cause of this discrepancy could not be pinpointed, mainly because the required measurement equipment applicable at 35 GHz was not available. Detailed measurements were furthermore complicated by the fact that the front end is a black box. Merely the beat signal could be measured; it was not possible to measure the outputs of the various subcomponents. Nevertheless, the measured results proved that the imaging of a large reflector was indeed feasible and thus an airborne campaign was arranged.

A successful airborne campaign was carried out at the Strausberg airfield just East of Berlin in June 2004. Next to the runway four large reflectors were set up. Several runs were flown parallel to the runway along the reflectors at different altitudes. From the data acquired during a run made at 100 m altitude a SAR image of acceptable quality could be produced.

The successful airborne campaign proved the practicability of airborne FM-CW SAR under operational conditions. Furthermore, it was shown that an FM-CW SAR system can indeed be operated in an efficient and cost effective manner from a relatively small airborne platform.

J. J. M. de Wit

Chapter 1

Introduction

The field of airborne earth observation devotes special attention to small, cost effective, high resolution imaging sensors. Such sensors could play an essential role in small-scale remote sensing applications, such as the monitoring of for instance dikes, watercourses, highways, nature reserves, or areas in which gas pipes or electrical power lines are buried. Furthermore, such sensors are of military interest; a small unmanned aircraft equipped with an imaging sensor can be used for reconnaissance tasks without endangering one's own troops.
In order to be successful, such sensor systems should consume little power and they should be small enough to be operated from small, possibly even unmanned, aircraft. Moreover, in order to be of interest to the civil market, cost effectiveness is mandatory.
Radar-based sensor systems are preferable, since they have some important advantages over optical sensors. Radar systems are capable of monitoring relatively large surfaces, they have all weather capability, and they can be applied in smoke and at night. However, radar systems have some drawbacks as well. One of them is the poor cross range or azimuth resolution. Another drawback, in particular for the armed forces, is the fact that radars can be traced, since they are active instruments.
The problem of poor azimuth resolution can be overcome by applying *synthetic aperture radar* (SAR) techniques. These techniques have already been successfully employed in the field of radar earth observation by using coherent pulse radar systems. However, pulse radars are usually very complex instruments, which are neither cost effective nor very compact. These systems are therefore less suitable for operation from very small (unmanned) aircraft or for low cost solutions.
Frequency modulated continuous wave (FM-CW) radar systems are, on the other hand, generally compact and relatively cheap to purchase and to exploit. Furthermore, FM-CW radar systems consume little power and they require a modest transmit power, which makes them relatively stealthy. Consequently, FM-CW radar technology seems to be of interest to civil and military airborne earth observation applications, particularly in combination with high resolution SAR techniques. The novel combination of FM-CW technology and SAR techniques should lead to the development of a small, lightweight, and cost effective, high resolution imaging sensor.
As already mentioned, SAR techniques have been successfully applied in combination with

coherent pulse radars. The practical feasibility of FM-CW SAR is however not evident. In pulse SAR processing it is assumed that the radar platform is stationary during the transmission of a pulse and the reception of the corresponding echo. This so-called *stop-and-go approximation* is valid because the transmitted pulses are very short. However, FM-CW radars transmit relatively long sweeps, which is why the stop-and-go approximation may no longer be valid. In that case, the change of the range during the transmission of a sweep and the reception of the corresponding echo should be taken into consideration. Other important topics to be dealt with in practice are the direct coupling between the transmitting and receiving antennas and the frequency sweep linearization.
The concept of FM-CW SAR has already been put forward in literature and some experimental systems have been described, [1]-[28]. Nevertheless, the area of airborne earth observation is a very novel application for FM-CW SAR systems. Therefore, at the International Research Centre for Telecommunications-transmission and Radar (IRCTR) of the Delft University of Technology, a project was initiated to investigate the feasibility of FM-CW SAR in the field of airborne earth observation.
The main objective of the project is to show the practicability of FM-CW SAR under operational circumstances. Therefore, a fully operational airborne demonstrator system has been developed. In addition, the demonstrator system should prove that an FM-CW SAR system can indeed be operated in an efficient and cost effective manner from a very small airborne platform. In the course of the project, a detailed system model has been developed in order to estimate and analyze the performance of the demonstrator system. After thorough ground-based and airborne experiments, the performance of the demonstrator system has been evaluated. The findings of this evaluation should facilitate the design of a future higher performance FM-CW SAR system.
Concurrently, special SAR processing algorithms, which take the characteristics of FM-CW signals into account, have been developed. In the final stage of the project, priority will be given to the implementation of a moving target indication (MTI) mode and, in collaboration with Eonic, the realization of real-time processing by using off-the-shelf parallel computer boards. The processing algorithms have been developed by A. Meta M.Sc., [29]-[31]. The development of the algorithms is therefore not treated in this thesis.
The project is carried out in close cooperation with TNO Defence, Security, and Safety (TNO) and it brings together the two main topics of the remote sensing research of the IRCTR and TNO. The IRCTR has a long tradition in developing and employing FM-CW radar systems, [32]-[34], whereas the remote sensing research at TNO concentrates on the development of pulse SAR systems and SAR processing techniques, [35]-[37]. Currently, TNO is working on the design of the miniaturized pulse SAR system MiniSAR, [38].

Outline of this Thesis

In **chapter 2**, the FM-CW radar principle and the SAR principle will be reviewed. Moreover, some practical problems concerning FM-CW radar systems and SAR systems will be discussed.
In **chapter 3**, the response of an FM-CW radar system to a single point target will be derived starting with the ideal situation. Consequently, various system distortions will be introduced and their effect will be investigated. Finally, the findings will be evaluated with the aid of the

results of a computer simulation.

In **chapter 4**, the response of an FM-CW SAR system to a single stationary point target will be derived. This derivation will be based on *range-Doppler* processing. Therefore, the range-Doppler algorithm will be reviewed first. Subsequently, the response will be derived by assuming that the stop-and-go approximation is valid and consequently the continuous platform motion will be taken into account. A modification to the range migration compensation will be proposed in order to compensate the effect of the continuous motion. Finally, the effect of phase errors will be investigated and the theoretical outcomes will be evaluated with the aid of a computer simulation.

In **chapter 5**, expressions for the available noise power, the signal power, and the signal-to-noise ratio (SNR) will be derived.

In **chapter 6**, the initial requirements to the demonstrator system will be given, the design considerations regarding the front end will be discussed (by using the equations derived in chapter 2), the background of the motion recording will be briefly reviewed, and a description of the complete demonstrator system will be given.

In **chapter 7**, the ground-based and airborne measurements will be presented. Moreover, a thorough performance analysis will be made (by using the expressions derived in chapter 5). Finally, the outcome of the performance analysis will weighted against the results obtained with a detailed system simulation.

In **chapter 8**, the main results of this study will be summarized and conclusions will be drawn. Furthermore, recommendations for future work will be given.

Chapter 2

Overview FM-CW Radar and SAR

Overview: In this chapter, the principles of FM-CW radar and SAR will be reviewed. Furthermore, the main practical problems concerning FM-CW radar systems and SAR systems will be addressed.

2.1 The FM-CW Radar Principle

FM-CW radar systems transmit a continuous wave, the frequency of which is modulated. An example of sawtooth frequency modulation is presented in Fig. 2.1(a). Objects or *targets* present in the antenna beam scatter a fraction of the transmitted wave back in the direction of the radar. This backscattered wave or *echo signal* is measured by the radar receiver.
The echo signal of a single stationary target arrives at the radar receiver after a time delay:

$$\Delta t = \frac{2R}{c} \qquad [\mathrm{s}], \tag{2.1}$$

in which R is the range to the target and c is the speed of light.
In the receiver the echo signal is demodulated with a nondelayed replica of the transmitted signal and subsequently low-pass filtered. The resulting signal after demodulation and low-pass filtering is called the beat signal, shown in Fig. 2.1(b). The frequency of the beat signal, the *beat frequency*, depends on the time delay. Thus the beat frequency is a measure for the range to the target. From Fig. 2.1(a) it can be seen that the beat frequency follows as:

$$f_b = \frac{\Delta f}{PRI}\Delta t \qquad [\mathrm{Hz}], \tag{2.2}$$

where Δf is the frequency sweep and PRI is the sweep repetition interval. The beat frequency, and therefore the range to the target, can be determined by applying a Fourier transform to the beat signal. Applying a Fourier transform to the beat signal results in a frequency spectrum which corresponds to a range spectrum. The range spectrum of a target is usually referred to as the *response* of a target. The response of a single stationary target is shown in Fig. 2.1(c).
When several targets are present, the final range spectrum will be the superposition of the responses of the individual targets. Note that in this case the sidelobes of the response of a strong target may conceal the response of another weaker target. The sidelobe level of the

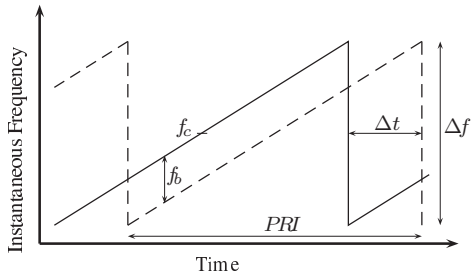

(a) The instantaneous frequency of the transmitted signal (solid) and that of the received signal (dashed) in the case of sawtooth frequency modulation, f_c is the carrier frequency. (Note that in practice $\Delta t \ll PRI$.)

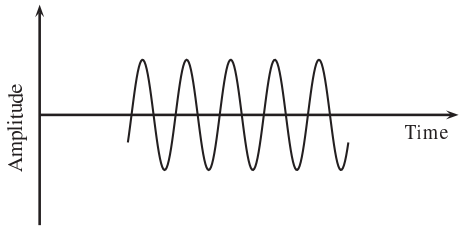

(b) The beat signal, the frequency of which is proportional to the range to the target.

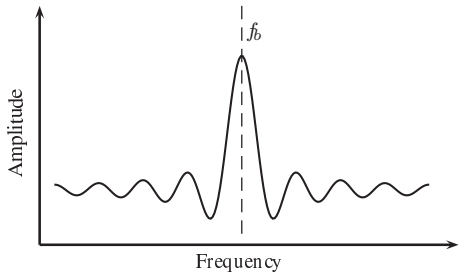

(c) The frequency spectrum of a single stationary point target. In FM-CW radar, the frequency spectrum is equivalent to a range spectrum.

Figure 2.1: A brief overview of the FM-CW radar principle.

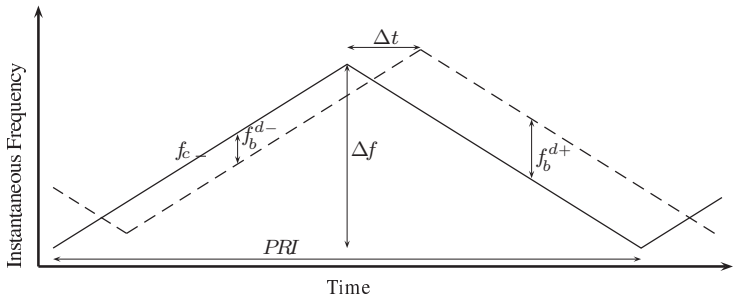

Figure 2.2: An example of triangular frequency modulation when a moving target is present. In this case, the difference between the instantaneous frequency of the transmitted signal (solid) and that of the echo signal (dashed) is not constant throughout the sweep.

response could be reduced by applying a windowing function to the beat signal prior to the Fourier transform, [39].

In current radar systems, the beat signal is generally digitized and a (discrete) fast Fourier transform (FFT) is applied to calculate the range spectrum. In this case, only a finite number of discrete beat frequencies can therefore be computed. As a result, the range spectrum is divided in a finite number of *range resolution cells*. Applying an FFT to a real-valued signal will result in a symmetrical frequency spectrum, just half of which is required to retrieve the range information. Therefore, when the digitized beat signal consists of n_s samples, only $n_s/2$ range resolution cells are available.

According to the Nyquist criterion, the maximum beat frequency that can be unambiguously measured is half the sample frequency. The maximum range is therefore determined by the sample frequency. With the aid of (2.1) and (2.2), the maximum range follows as:

$$R_{max} = \frac{cPRI}{2\Delta f}\frac{f_s}{2} = \frac{c}{2\Delta f}\frac{n_s}{2} \qquad [\mathrm{m}], \tag{2.3}$$

in which f_s is the sample frequency and n_s is the number of samples in the digitized beat signal. By recalling that $n_s/2$ samples are available in the range spectrum, the range resolution is given as:

$$\delta r = \frac{c}{2\Delta f} \qquad [\mathrm{m}]. \tag{2.4}$$

Presence of a Moving Target

When the target is moving relative to the radar, an additional Doppler frequency shift f_d is superimposed on the beat frequency, leading to an invalid range measurement. The Doppler frequency shift is given as, [40]:

$$f_d = \frac{2}{\lambda}\frac{\mathrm{d}R}{\mathrm{d}t} = \frac{2v_d}{\lambda} \qquad [\mathrm{Hz}], \tag{2.5}$$

where λ is the wavelength of the transmitted signal and v_d is the radial velocity.

The Doppler frequency shift may be extracted by using a triangular frequency modulation, see Fig. 2.2. Assume that a target is approaching the radar. In that case, the frequency difference

between the transmitted and the echo signal during the upslope will be the difference between the beat frequency due to the range and the Doppler frequency shift. Similarly, during the downslope the difference frequency is the sum of the beat frequency due to the range and the Doppler frequency shift:

$$\begin{aligned} \text{upslope:} \quad & f_b^{d-} = f_b - f_d \qquad [\text{Hz}], \\ \text{downslope:} \quad & f_b^{d+} = f_b + f_d \qquad [\text{Hz}]. \end{aligned} \tag{2.6}$$

The beat frequency due to the range may be extracted by taking the average of the frequency difference when $f_b > f_d$, [40].
Moving targets may also be detected by applying sweep-to-sweep processing, [41]-[43]. The simplest form of sweep-to-sweep processing is a canceller that subtracts successive sweeps. Then, stationary targets are cancelled out and only moving targets remain. The phase difference between successive sweeps can be used to estimate the velocity of moving targets. This is however only feasible for slow moving targets.

2.2 FM-CW Radar Practical Considerations

Oscillator Phase Noise and Direct Coupling

A free-running ideal oscillator generates a perfectly sinusoidal signal. In that case, the spectrum of the oscillator's output signal exhibits a single peak at the carrier frequency. The output of a practical oscillator jitters, on the other hand, in amplitude as well as in phase. Therefore, the spectrum of a practical oscillator's output is composed of a peak at the carrier frequency with broad sidebands. In practical oscillators, the effect of amplitude jitter is usually negligible compared to the effect of phase jitter, [44]. The remainder of this subsection will therefore focus on the phase jitter or *oscillator phase noise*. Oscillator phase noise and its effects have been studied extensively over the years, [41]-[59].
Oscillator phase noise proves important to FM-CW radars, since the phase noise sidebands associated with a large (unwanted) signal effectively raise the noise floor. This may be the case even if the main spectral component of that signal is outside the frequency band of interest. Within this context, the direct coupling between the transmitting and receiving antennas is a well-known problem in FM-CW radars. The total propagation path of the direct-coupled signal is very short. Therefore, its main spectral component is at very low frequencies after demodulation; that is far outside the frequency band of interest for most applications. However, the phase noise sidebands may extend well into the frequency band of interest. This is an important problem, since the direct coupling is usually much stronger than the echo signals.
The effect is significantly reduced when a fraction of the transmitted signal is used as local oscillator (LO) signal in the receiver, since in that case the phase noise of the echo signal is correlated with the phase noise of the LO signal, [60]-[67]. This *range correlation effect* can be maximized by tuning the path length of the LO signal to the propagation path of the direct coupling, [41]-[42].
The phase noise power can be reduced in other ways as well. Obviously, the use of an oscillator with superior phase noise specifications decreases the phase noise power, [68]. Furthermore, it is possible to partially compensate the effect of phase noise with special signal

processing techniques, [43], [69]-[70].

Frequency Sweep Nonlinearity

Another important system parameter is the frequency sweep nonlinearity, [69]-[80], which is usually expressed as a percentage of the total sweep. When the sweep is nonlinear, the beat frequency is not constant throughout the sweep interval and the range response is broadened. The effect of sweep nonlinearities is reduced when a portion of the transmitted signal is used as LO signal, since in that case the sweep nonlinearity of the echo signal is correlated with the sweep nonlinearity of the LO signal, [79]. This is particularly true for echoes coming from targets at a short range. An analytical development of the effect of sweep nonlinearities will be given in section 3.2.
The effect of sweep nonlinearities may be reduced by applying a linearizer circuit. The linearizer circuit should however be fast enough to follow the frequency transitions at the end of each sweep, [80].

Frequency Sweep Transitions

At the beginning of a new sweep, the beat frequency equals the large difference between the instantaneous received frequency and the instantaneous transmitted frequency, see Fig. 2.1(a). This frequency is usually outside the receiver's bandwidth. Moreover, the frequency transitions between the sweeps are typically nonlinear and the transit times are finite, causing distortions in the beat signal. In practice, the parts of the beat signal around the sweep transitions are therefore discarded, [73], [80]-[81].

2.3 The Synthetic Aperture Radar Principle

In conventional radar systems the azimuth resolution deteriorates as range increases, since the antenna beam widens. The azimuth resolution is given as:

$$\delta Az \approx \theta_{Az} R \qquad [\mathrm{m}], \tag{2.7}$$

in which θ_{Az} is the azimuth 3-dB antenna beamwidth. The antenna beamwidth depends on the antenna length l, [40]:

$$\theta_{Az} \approx \frac{\lambda}{l}, \quad l \gg \lambda \qquad [\mathrm{rad}]. \tag{2.8}$$

As can be seen from (2.7) and (2.8), the azimuth resolution improves as the antenna length increases.
In synthetic aperture radar a large antenna length is synthesized by making use of the motion of the radar platform. In Fig. 2.3 the airborne stripmap-mode SAR geometry is shown. The antenna beam is oriented normal to the flight track; hence a strip of land parallel to the flight track is illuminated. As the radar platform flies by, a target on the ground is illuminated for a certain period of time depending upon the real antenna beamwidth. During this period a number of sweeps are transmitted and the corresponding echoes are received.
The coherent integration of n_e echoes yields a synthetic aperture of length:

$$L_{sar} = \frac{n_e v}{PRF} = v T_{sar} \qquad [\mathrm{m}], \tag{2.9}$$

where v is the radar platform velocity, *PRF* is the sweep repetition frequency, and T_{sar} is the SAR observation time. By combining (2.8) and (2.9), the synthetic antenna beamwidth follows as:

$$\theta_{sar} = \frac{\lambda}{2L_{sar}} \qquad [\text{rad}]. \tag{2.10}$$

The factor of 2 in the denominator is introduced to account for the fact that the antenna beam is formed after the waves have traveled to the target and back, [40].
The phase relationship between the successive echoes, or *azimuth phase history*, is a function of the range to the target:

$$\varphi_{Az}(t) = \frac{4\pi R(t)}{\lambda} \qquad [\text{rad}]. \tag{2.11}$$

The range to the target throughout the SAR observation time can be written as:

$$R(t) = \sqrt{R_0^2 + v^2 t^2} \qquad [\text{m}], \tag{2.12}$$

in which R_0 is the shortest distance to the target and t is time. The time t is defined on the interval $[-\frac{1}{2}T_{sar},\ \frac{1}{2}T_{sar}]$. Usually, (2.12) is approximated by the first terms of its Taylor series expansion, [82]:

$$R(t) \approx R_0 + \frac{v^2 t^2}{2R_0} \qquad [\text{m}]. \tag{2.13}$$

As can be seen from (2.13), the range to the target is not constant during the SAR observation time. Therefore, the azimuth phase history is not constant and the number of echoes that can be coherently integrated is limited.
In *focused SAR*, the relative phase between the successive echoes is compensated with the aid of the known phase history (2.11). In the case of focused SAR, the maximum number of echoes:

$$n_{e,max} = \frac{\theta_{Az} R_0}{vPRI} \qquad [\,], \tag{2.14}$$

can therefore be coherently integrated. The maximum number of echoes that can be integrated depends on the time that the target is illuminated and thus on the real antenna beamwidth.
When indeed the maximum number of echoes is integrated, the synthetic antenna beamwidth follows as (by using (2.9), (2.10), and (2.14)):

$$\theta_{sar} = \frac{\lambda}{2\theta_{Az} R_0} \qquad [\text{rad}]. \tag{2.15}$$

And finally, the SAR azimuth resolution can be written as:

$$\delta Az_{sar} = \frac{\lambda}{2\theta_{Az}} = \frac{l}{2} \qquad [\text{m}]. \tag{2.16}$$

It should be noted that the azimuth resolution after focused SAR processing has become independent of range.

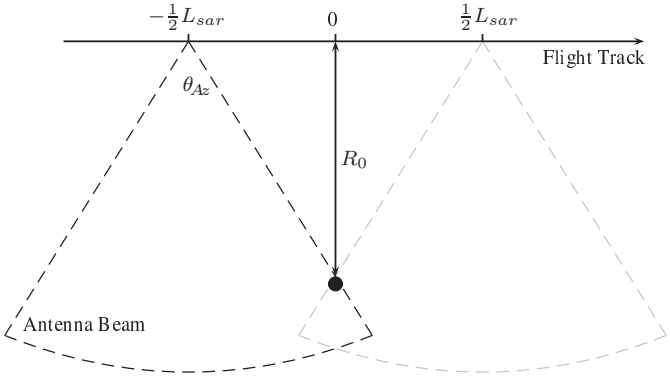

Figure 2.3: Topview of the stripmap mode SAR geometry. The antenna beam is directed normal to the flight track; hence a strip of land parallel to the flight track is illuminated. The black dot represents a target illuminated by the radar.

Azimuth Sampling

Due to the radar platform motion, even the echo of a stationary object exhibits a Doppler frequency shift. This Doppler frequency shift depends on the radial velocity. The radial velocity varies throughout the SAR observation time and its absolute value is maximal when the object is at the rims of the real antenna beam.
When the object is at the rim of the real antenna beam, the radial velocity can be written as:

$$v_{d,max} = v\sin\left(\frac{\theta_{Az}}{2}\right) \approx \frac{v\theta_{Az}}{2} \qquad [\mathrm{ms}^{-1}], \tag{2.17}$$

and, by using (2.5), the corresponding Doppler frequency shift follows as:

$$f_{d,max} \approx \frac{v\theta_{Az}}{\lambda} \qquad [\mathrm{Hz}]. \tag{2.18}$$

The sample rate in azimuth direction should be high enough to be able to unambiguously measure the Doppler frequency shift. Effectively, the *PRF* represents the azimuth sample rate. The *PRF* should therefore be at least:

$$PRF \geq 2f_{d,max} \approx \frac{2v\theta_{Az}}{\lambda} \qquad [\mathrm{Hz}]. \tag{2.19}$$

2.4 SAR Practical Considerations

SAR processing makes use of the known azimuth phase history (2.11). The phase history is however distorted by *phase errors*, degrading the SAR image quality. An in-depth reading of phase errors will be given in section 4.4.
The main sources for phase errors are platform motion errors. The effects of platform motion

errors have been the subject of many studies, [83]-[92]. In this section, the upper limits to different classes of uncompensated motion errors will be reviewed. The derivations of the upper limits will be repeated in appendix A.
The cross-track velocity component is directed normal to the along-track direction in the slant-range plane. The along-track velocity is defined in the along-track direction.

Along-Track Velocity Error

The along-track velocity of the radar platform may be assumed to vary slowly compared to the SAR observation time. The error may therefore be considered constant throughout the SAR observation time. The error should be bounded by:

$$\mathrm{d}v_{at} \leq \frac{v}{\lambda R_0}\delta A z_{sar}^2 \qquad [\mathrm{ms}^{-1}], \tag{2.20}$$

in order to limit the quadratic phase error to $\pi/4$, [92]. A long-term along-track velocity error causes a geometric scaling error.

Cross-Track Velocity Error

A cross-track velocity component may be assumed to be of short term duration, since a long-term component can only exist if the platform navigation fails. Such a velocity component leads to an azimuth displacement. In order to limit the displacement to less than an azimuth resolution cell, the component should be restricted to, [92]:

$$v_{ct} \leq \frac{v}{R_0}\delta A z_{sar} \qquad [\mathrm{ms}^{-1}]. \tag{2.21}$$

Cross-Track Acceleration Error

The cross-track acceleration should be bounded by:

$$a_{ct} \leq \frac{2v^2}{\lambda R_0^2}\delta A z_{sar}^2 \qquad [\mathrm{ms}^{-2}], \tag{2.22}$$

in order to limit the quadratic phase error to $\pi/4$, [92]. A short-term acceleration leads to defocusing, whereas a long-term acceleration results in azimuth scaling errors and finally in absolute positioning errors.

Angular Motion

Strictly speaking, attitude variations of the platform do not give rise to phase errors. This is true when the antenna phase center (APC) is located at the motion center (MC) of the platform. However, due to angular motion, the antenna gain may vary during the SAR observation time. Angular motion may therefore introduce amplitude variations.
In practice, a lever arm is usually present between the APC and the platform MC. In that case, angular motion will introduce additional along-track and cross-track velocity components.

Sinusoidal Motion Errors

During the SAR observation time, the radar platform is likely to deviate from the ideal track. The phase errors caused by the deviations depend on the absolute divergence from the ideal track, but also on the frequency of the deviations f_e. In order to investigate the frequency dependence of the phase errors, the actual flight track is assumed to be sinusoidal.

In the case of low-frequency sinusoidal motion ($f_e < 2/T_{sar}$), the motion may be approximated as either linear or quadratic, [92]. If the motion is assumed to be linear, a cross-track velocity component is present. The main effect is an azimuth displacement and the upper bound to the cross-track velocity is again given by (2.21), [87].
When the sinusoidal motion is, on the other hand, assumed to be quadratic, the velocity in the slant-range direction should be limited to, [92]:

$$v_{ct} \leq \frac{\lambda}{4\pi f_e T_{sar}^2} \qquad [\mathrm{ms}^{-1}], \tag{2.23}$$

in order to restrict the quadratic phase error to $\pi/4$.
High-frequency sinusoidal motion ($f_e > 2/T_{sar}$) gives rise to spurious sidelobes. For a peak sidelobe level to peak mainlobe level ratio of p, the velocity in the slant-range direction should be bounded by, [87]:

$$v_{ct} \leq \lambda f_e \sqrt{p} \qquad [\mathrm{ms}^{-1}]. \tag{2.24}$$

Recapitulation: The basic equations related to the FM-CW radar and SAR principles were given. In section 6.2, these equations will be used to determine the demonstrator system parameters. Moreover, the major system imperfections of FM-CW radars, being the direct coupling and frequency sweep nonlinearities, were reviewed. The effect of sweep nonlinearities will be investigated in more detail in section 3.2. The main practical difficulty in SAR systems are the motion errors. The upper limits to the different categories of motion errors were given. These upper limits will be utilized in section 6.3 to evaluate the performance of the selected combination of motion sensors.

Chapter 3

Impulse Response of an FM-CW Radar

Overview: In this chapter, the response of an FM-CW radar system to a single point target will be derived, starting with the ideal case. Subsequently, several system distortions will be introduced and their effect will be investigated. Finally, the theoretical findings will be evaluated with the aid of a computer simulation.

3.1 Ideal Case

The response to a point target will be derived by assuming that the FM-CW radar system is ideal. When sawtooth frequency modulation is applied, the transmitted signal can be expressed as (refer to Fig. 2.1(a)):

$$s_t(t) = V_t \cos\big(2\pi f_c t + \frac{\pi \Delta f}{PRI} t^2 + \varphi_0\big), \tag{3.1}$$

in which V_t is the transmitted signal's amplitude, f_c is the carrier frequency, and φ_0 is the initial phase. For the sake of clarity, the initial phase is assumed to be zero.
The response will be derived for a single sweep. The time t is therefore defined on the interval $[-\frac{1}{2}PRI,\ \frac{1}{2}PRI]$. Furthermore, the nonlinear effects around the sweep transitions, discussed in section 2.2, are ignored.
The echo signal from a stationary point target can be written as a time-delayed and attenuated version of the transmitted signal:

$$s_r(t) = V_r \cos\big(2\pi f_c (t - \Delta t) + \frac{\pi \Delta f}{PRI} (t - \Delta t)^2\big), \tag{3.2}$$

where V_r is the amplitude of the echo signal.
In the receiver the echo signal is demodulated by mixing it with the LO signal, leading to the beat signal. In FM-CW radars, the LO signal is usually a nondelayed replica of the transmitted signal. After demodulation, the beat signal follows as:

$$s_b(t) = s_r(t) \cdot s_t(t) = \frac{V_r V_{LO}}{2} \big(\cos(\varphi_{LO} - \varphi_r) + \cos(\varphi_{LO} + \varphi_r)\big), \tag{3.3}$$

where V_{LO} is the amplitude of the LO signal. The variables φ_{LO} and φ_r represent the phase of the LO signal and the echo signal respectively. Note that φ_{LO} and φ_r are time dependent.

The beat signal comprises a down-conversion component at baseband and an up-conversion component around $2f_c$. In practice, the up-conversion component is outside the receiver's bandwidth and it is usually filtered out with a low-pass filter. In that case, the beat signal reduces to:

$$s_b(t) = V_b \cos\big(2\pi f_c \Delta t + \frac{\pi \Delta f}{PRI}(2\Delta t \cdot t - \Delta t^2)\big), \tag{3.4}$$

in which $V_b = \frac{1}{2} V_r V_{LO}$.
Subsequently, the beat signal is converted to the frequency domain by applying a Fourier transform to (3.4):

$$S_b(f_R) = \int_{-\gamma}^{\gamma} s_b(t) \exp[-\mathrm{j}2\pi f_R t]\mathrm{d}t, \tag{3.5}$$

where f_R denotes range-frequency, which can be converted to range with the aid of (2.1) and (2.2), and:

$$\gamma = \frac{PRI}{2}. \tag{3.6}$$

Finally, the evaluation of (3.5) results in the response to a single point target:

$$\begin{aligned} S_b(f_R) = {} & \gamma V_b \exp[\,\mathrm{j}(\varphi_1 + \varphi_2)]\mathrm{sinc}\big(2\pi\gamma(f_b - f_R)\big) \\ & + \gamma V_b \exp[-\mathrm{j}(\varphi_1 + \varphi_2)]\mathrm{sinc}\big(2\pi\gamma(f_b + f_R)\big), \end{aligned} \tag{3.7}$$

in which:

$$\varphi_1 = 2\pi f_c \Delta t, \tag{3.8}$$

and:

$$\varphi_2 = -\frac{\pi \Delta f}{PRI}\Delta t^2. \tag{3.9}$$

The range to the target can now be found by determining the maximum of the response. The maximum of (3.7) on the interval $[0, \frac{1}{2} f_s]$ is located at:

$$f_R = f_b, \tag{3.10}$$

which is consistent with (2.2).

3.2 Frequency Sweep Nonlinearity

The response in the presence of a sweep nonlinearity will be developed. First by assuming that the nonlinearity is sinusoidal and consequently by assuming that the nonlinearity is quadratic.

Sinusoidal Sweep Nonlinearity

When the frequency sweep nonlinearity is assumed to be sinusoidal, the instantaneous frequency of the transmitted signal can be written as:

$$f_{t,i}(t) = f_c + \frac{\Delta f}{PRI}t + \Delta f_e \cos\big(2\pi f_m t + \varphi_e\big), \tag{3.11}$$

where Δf_e is the maximum absolute deviation from the linear sweep, f_m is the frequency of the nonlinearity, and φ_e is the initial phase of the nonlinearity. The nonlinearity's initial phase is assumed to be zero. In this case, the transmitted signal follows as:

$$s_t(t) = V_t \cos\big(2\pi f_c t + \frac{\pi \Delta f}{PRI}t^2 + D_m \sin(2\pi f_m t)\big), \tag{3.12}$$

in which:

$$D_m = \frac{\Delta f_e}{f_m}, \tag{3.13}$$

is the peak angular deviation. The echo signal can again be expressed as a time-delayed and attenuated version of the transmitted signal:

$$s_r(t) = V_r \cos\big(2\pi f_c(t-\Delta t) + \frac{\pi \Delta f}{PRI}(t-\Delta t)^2 + D_m \sin(2\pi f_m(t-\Delta t))\big). \tag{3.14}$$

In the receiver the echo signal is demodulated with a nondelayed fraction of the transmitted signal (thus the LO signal exhibits the same sweep nonlinearity as the echo signals). By discarding the up-conversion component, the beat signal follows as:

$$\begin{aligned} s_b(t) = V_b \cos\big(&2\pi f_c \Delta t + \frac{\pi \Delta f}{PRI}(2\Delta t \cdot t - \Delta t^2) \\ &+ D_m \sin(2\pi f_m t) - D_m \sin(2\pi f_m(t-\Delta t))\big), \end{aligned} \tag{3.15}$$

which can be rewritten as:

$$s_b(t) = V_b \cos\big(2\pi f_c \Delta t + \frac{\pi \Delta f}{PRI}(2\Delta t \cdot t - \Delta t^2) + D'_m \cos(2\pi f_m(t - \frac{\Delta t}{2}))\big), \tag{3.16}$$

where:

$$D'_m = 2D_m \sin(\pi f_m \Delta t). \tag{3.17}$$

By assuming *narrowband angle modulation*, the beat signal can be approximated by, [93]:

$$\begin{aligned} s_b(t) \approx V_b \cos\big(&2\pi f_c \Delta t + \frac{\pi \Delta f}{PRI}(2\Delta t \cdot t - \Delta t^2)\big) - V_b D'_m \cos\big(2\pi f_m(t - \frac{\Delta t}{2})\big) \\ &\sin\big(2\pi f_c \Delta t + \frac{\pi \Delta f}{PRI}(2\Delta t \cdot t - \Delta t^2)\big). \end{aligned} \tag{3.18}$$

This approximation is valid for small values of D_m. Finally, the application of a Fourier transform results in the response:

$$\begin{aligned} S_b(f_R) = &\gamma V_b \exp[\,\mathrm{j}(\varphi_1 + \varphi_2)]\mathrm{sinc}\big(2\pi\gamma(f_b - f_R)\big) \\ &+ \gamma V_b \exp[-\mathrm{j}(\varphi_1 + \varphi_2)]\mathrm{sinc}\big(2\pi\gamma(f_b + f_R)\big) \end{aligned}$$

$$
\begin{aligned}
&- \frac{\gamma V_b D'_m}{2\mathrm{j}} \exp[-\mathrm{j}\varphi_3]\mathrm{sinc}\big(2\pi\gamma(f_b^{m-} - f_R)\big) \\
&+ \frac{\gamma V_b D'_m}{2\mathrm{j}} \exp[\,\mathrm{j}\varphi_3]\mathrm{sinc}\big(2\pi\gamma(f_b^{m-} + f_R)\big) \\
&- \frac{\gamma V_b D'_m}{2\mathrm{j}} \exp[\,\mathrm{j}\varphi_4]\mathrm{sinc}\big(2\pi\gamma(f_b^{m+} - f_R)\big) \\
&+ \frac{\gamma V_b D'_m}{2\mathrm{j}} \exp[-\mathrm{j}\varphi_4]\mathrm{sinc}\big(2\pi\gamma(f_b^{m+} + f_R)\big),
\end{aligned} \tag{3.19}
$$

in which:

$$f_b^{m-} = f_b - f_m, \tag{3.20}$$

$$f_b^{m+} = f_b + f_m, \tag{3.21}$$

$$\varphi_3 = -\varphi_1 - \varphi_2 - \pi f_m \Delta t, \tag{3.22}$$

and:

$$\varphi_4 = \varphi_1 + \varphi_2 - \pi f_m \Delta t. \tag{3.23}$$

From (3.19) it can be concluded that a sinusoidal sweep nonlinearity produces spurious sidelobes or *paired echoes* around the original response. However, one should bear in mind that in reducing (3.16) to (3.18), narrowband angle modulation was assumed. In practice, a sinusoidal sweep nonlinearity will produce an infinite number of harmonics.
Moreover, the amplitude of the paired echoes depends upon the time delay. Therefore, for short delay times, the amplitude is reduced significantly. This effect is due to the fact that a portion of the transmitted signal has been used as LO signal, as was already discussed in section 2.2.
In practice, the modulating frequency f_m will be very low compared to the PRF. The sweep nonlinearity will therefore broaden the response rather than produce distinct paired echoes.

Quadratic Sweep Nonlinearity

In the case of a quadratic sweep nonlinearity, the instantaneous frequency of the transmitted signal can be expressed as:

$$f_{t,i}(t) = f_c - \Delta f_e + \frac{\Delta f}{PRI}t + \frac{4\Delta f_e}{PRI^2}t^2. \tag{3.24}$$

The nonlinearity has been defined in such a way that the maximum deviation from the linear sweep occurs in the middle of the sweep.
The phase of the transmitted signal follows as the primitive function of (3.24) multiplied by 2π:

$$\varphi_t(t) = 2\pi(f_c - \Delta f_e)t + \frac{\pi\Delta f}{PRI}t^2 + \frac{8\pi\Delta f_e}{3PRI^2}t^3. \tag{3.25}$$

The phase of the echo signal can be written as a time-delayed version of (3.25):

$$\varphi_r(t) = 2\pi(f_c - \Delta f_e)(t - \Delta t) + \frac{\pi\Delta f}{PRI}(t - \Delta t)^2 + \frac{8\pi\Delta f_e}{3PRI^2}(t - \Delta t)^3. \tag{3.26}$$

The echo signals are again demodulated with a nondelayed fraction of the transmitted signal. Then the phase of the down-conversion component is given as:

$$\varphi_b(t) = 2\pi f_c \Delta t - \frac{\pi \Delta f}{PRI}\Delta t^2 + \frac{2\pi \Delta f}{PRI}\Delta t \cdot t \\ - 2\pi \Delta f_e \Delta t - \frac{8\pi \Delta f_e}{3PRI^2}\left(-3\Delta t \cdot t^2 + 3\Delta t^2 \cdot t - \Delta t^3\right). \tag{3.27}$$

Consequently, the instantaneous beat frequency follows as the derivative of (3.27) divided by 2π:

$$f_{b,i}(t) = f_b - \frac{4\Delta f_e \Delta t^2}{PRI^2} + \frac{8\Delta f_e \Delta t}{PRI^2}t. \tag{3.28}$$

With the aid of (3.28), the variation of the beat frequency throughout a single sweep can be calculated. On the interval $[-\frac{1}{2}PRI,\ \frac{1}{2}PRI]$, the full beat frequency variation is:

$$\Delta f_b = f_{b,i}(t = PRI/2) - f_{b,i}(t = -PRI/2) = \frac{8\Delta f_e}{PRI}\Delta t. \tag{3.29}$$

The spectral width of the final response can be estimated by the square root of the sum of the squares of the spectral width of the ideal response (that is $1/PRI$) and the beat frequency's spectral width Δf_b, [73], [94]:

$$\sqrt{\left(\frac{1}{PRI}\right)^2 + \Delta f_b^2}. \tag{3.30}$$

Subsequently, a limit to the maximum absolute deviation from the linear sweep can be specified by making use of (3.30). Let's assume that a maximum resolution loss of 10 % is allowed, then:

$$\frac{\sqrt{\left(\frac{1}{PRI}\right)^2 + \Delta f_b^2}}{\sqrt{\left(\frac{1}{PRI}\right)^2}} \leq 1.1. \tag{3.31}$$

Finally, by using (3.29), (3.31) can be rewritten as:

$$\Delta f_e \leq \frac{\sqrt{0.21}c}{16R_{max}}, \tag{3.32}$$

providing an upper limit to the nonlinearity as a function of range. As can be seen, the specification for the nonlinearity is less stringent for short ranges. Please note that (3.32) provides only a rough upper limit, since (3.30) is just an estimate of the spectral width. Furthermore, practical nonlinearities are not likely to be (perfectly) quadratic.
By comparing (3.10) and (3.28) it can be seen that the beat frequency is affected by the sweep nonlinearity. Thus, apart from a loss of resolution, the presence of frequency sweep nonlinearities also results in an invalid range measurement.

3.3 Amplitude Variations

In the previous sections it was assumed that the amplitude of the echo signal is constant. However, when the amplitude of the echo signal varies with time, for instance due to variations of the target's radar cross section, the response will be affected.

When it is assumed that the amplitude variation is sinusoidal, the echo signal can be written as:

$$s_r(t) = \big\{V_r + V_m \cos\big(2\pi f_m t\big)\big\} \cos\big(2\pi f_c (t - \Delta t) + \frac{\pi \Delta f}{PRI}(t - \Delta t)^2\big), \tag{3.33}$$

where V_m is the amplitude of the variation and f_m is the modulating frequency. If it is assumed that $f_m \ll f_c$, then the up-conversion component can be discarded again and the beat signal follows as:

$$s_b(t) = \frac{V_{LO}}{2}\big\{V_r + V_m \cos\big(2\pi f_m t\big)\big\} \cos\big(2\pi f_c \Delta t + \frac{\pi \Delta f}{PRI}(2\Delta t \cdot t - \Delta t^2)\big), \tag{3.34}$$

which can be expanded as:

$$\begin{aligned} s_b(t) = {} & V_b \cos\big(2\pi f_c \Delta t + \frac{\pi \Delta f}{PRI}(2\Delta t \cdot t - \Delta t^2)\big) \\ & + \frac{V_{LO} V_m}{4} \cos\big(2\pi f_c \Delta t + \frac{\pi \Delta f}{PRI}(2\Delta t \cdot t - \Delta t^2) - 2\pi f_m t\big) \\ & + \frac{V_{LO} V_m}{4} \cos\big(2\pi f_c \Delta t + \frac{\pi \Delta f}{PRI}(2\Delta t \cdot t - \Delta t^2) + 2\pi f_m t\big). \end{aligned} \tag{3.35}$$

Note that the amplitude of the LO signal is considered to be constant. After transformation to the frequency domain, the response follows as:

$$\begin{aligned} S_b(f_R) = {} & \gamma V_b \exp\big[\,\mathrm{j}(\varphi_1 + \varphi_2)\big] \mathrm{sinc}\big(2\pi\gamma(f_b - f_R)\big) \\ & + \gamma V_b \exp[-\mathrm{j}(\varphi_1 + \varphi_2)] \mathrm{sinc}\big(2\pi\gamma(f_b + f_R)\big) \\ & + \frac{\gamma V_{LO} V_m}{4} \exp\big[\,\mathrm{j}(\varphi_1 + \varphi_2)\big] \mathrm{sinc}\big(2\pi\gamma(f_b^{m-} - f_R)\big) \\ & + \frac{\gamma V_{LO} V_m}{4} \exp\big[-\mathrm{j}(\varphi_1 + \varphi_2)\big] \mathrm{sinc}\big(2\pi\gamma(f_b^{m-} + f_R)\big) \\ & + \frac{\gamma V_{LO} V_m}{4} \exp\big[\,\mathrm{j}(\varphi_1 + \varphi_2)\big] \mathrm{sinc}\big(2\pi\gamma(f_b^{m+} - f_R)\big) \\ & + \frac{\gamma V_{LO} V_m}{4} \exp\big[-\mathrm{j}(\varphi_1 + \varphi_2)\big] \mathrm{sinc}\big(2\pi\gamma(f_b^{m+} + f_R)\big). \end{aligned} \tag{3.36}$$

From (3.36) it can be seen that high-frequency amplitude variations lead to paired echoes around the original response. Low-frequency amplitude variations will result in a loss of resolution.

3.4 Moving Target

As was already discussed in section 2.1, a moving target induces a Doppler frequency shift. This Doppler frequency shift has its effect on the response.
In the case of a moving target, the time delay can be expanded as, [95]:

$$\Delta t(t) \approx \Delta t_0 + \frac{f_d}{f_c}(t - \Delta t_0), \tag{3.37}$$

in which Δt_0 is the time delay at $t = 0$ and it is assumed that the acceleration of the target is negligible.
When taking the target motion into account, the echo signal becomes:

$$s_r(t) = V_r \cos\big(2\pi f_c(t - \Delta t(t)) + \frac{\pi \Delta f}{PRI}(t - \Delta t(t))^2\big). \tag{3.38}$$

With the aid of (3.37), (3.38) can be rewritten as:

$$s_r(t) = V_r \cos\big(2\pi f_c(\mu t - \mu \Delta t_0) + \frac{\pi \Delta f}{PRI}(\mu t - \mu \Delta t_0)^2\big), \tag{3.39}$$

where $\mu = 1 - f_d/f_c$. After demodulation and by discarding the up-conversion component again, the beat signal follows as:

$$\begin{aligned} s_b(t) = V_b \cos\big(&\frac{\pi \Delta f}{PRI}(1 - \mu^2)t^2 + \frac{2\pi \Delta f}{PRI}\mu \Delta t_0\, t + 2\pi f_c(1 - \mu)t \\ &+2\pi f_c\, \mu \Delta t_0 - \frac{\pi \Delta f}{PRI}\mu^2 \Delta t_0^2\big). \end{aligned} \tag{3.40}$$

The comparison of (3.4) and (3.40) shows that the target motion gives rise to a quadratic term (the first term of the cosine's argument) and a Doppler frequency shift (the third term of the cosine's argument). Furthermore, the other terms are modified by either μ or μ^2.
The main effect of the motion is the Doppler frequency shift. The quadratic term is negligible as well as the effect on the other terms (in practice: $f_d \ll f_c$). By taking solely the Doppler frequency shift into account, (3.40) reduces to:

$$s_b(t) \approx V_b \cos\big(\frac{2\pi \Delta f}{PRI}\Delta t_0\, t + 2\pi f_d t + 2\pi f_c \Delta t_0 - \frac{\pi \Delta f}{PRI}\Delta t_0^2\big). \tag{3.41}$$

Finally, after conversion to the frequency domain, the response follows as:

$$\begin{aligned} S_b(f_R) = &\gamma V_b \exp[\,\mathrm{j}(\varphi_1 + \varphi_2)]\mathrm{sinc}\big(2\pi\gamma(f_b^{d+} - f_R)\big) \\ &+ \gamma V_b \exp[-\mathrm{j}(\varphi_1 + \varphi_2)]\mathrm{sinc}\big(2\pi\gamma(f_b^{d+} + f_R)\big). \end{aligned} \tag{3.42}$$

From (3.42) it can be concluded that the response is shifted in frequency, and thus in range, due to the target motion. The shape of the response is however not affected, as long as the radial velocity of the target is constant. When the target is accelerating, the response will be broadened, [96].

3.5 Impulse Response Simulation

In order to evaluate the theoretical results, the response of an FM-CW radar to a single point target has been simulated. The system parameters used in the simulation are listed in table 3.1. They resemble those of the FM-CW SAR demonstrator system, see chapter 6. The system disturbances discussed in the previous sections have been introduced in the simulation.

Table 3.1: The system parameters and measurement geometry used in the simulation of the impulse response.

Carrier Frequency f_c:	35 GHz	Range Resolution δr:	30 cm
Frequency Sweep Δf:	500 MHz	Slant Range R_0:	700 m
PRF:	1 kHz	SAR Length L_{sar}:	25 m
Modulation:	Sawtooth	Azimuth Resolution δAz_{sar}:	12 cm

Sinusoidal Sweep Nonlinearity

In Fig. 3.1(a) the response of an FM-CW radar is shown when a sinusoidal sweep nonlinearity is present. The response is shown for a low-frequency nonlinearity, $f_m = PRF$, and for a high-frequency nonlinearity, $f_m = 5PRF$. The maximum deviation Δf_e is in both cases 150 kHz; that is 0.03 % of the frequency sweep.

The paired echoes are apparent. By using (3.19) it can be calculated that, in the case of low-frequency modulation, the position of the paired echoes should be $\pm$0.3 m relative to the location of the mainlobe and that, for high-frequency modulation, the positions of the paired echoes should be $\pm$1.5 m relative to the location of the mainlobe. The peak level of the paired echoes should be approximately -9.1 dB relative to the peak level of the mainlobe. From Fig. 3.1(a) it can be concluded that these values correspond very well with the simulated results. Furthermore, it can be seen that the effect on the mainlobe itself is quite small.

Quadratic Sweep Nonlinearity

The effect of a quadratic sweep nonlinearity is presented in Fig. 3.5. The response is shown for a maximum deviation Δf_e of 50 kHz and 100 kHz; that is 0.01 % and 0.02 % of the frequency sweep respectively.

It is noticeable that the effect on the mainlobe is much larger than in the case of a sinusoidal sweep nonlinearity, although the maximum deviation Δf_e is smaller.

Amplitude Modulation

Fig. 3.5 shows the response when the amplitude of the echo signal is sinusoidally modulated. Again the response is shown for low-frequency modulation, $f_m = PRF$, and for high-frequency modulation, $f_m = 5PRF$. The amplitude of the modulation V_m is in both cases $V_b/4$.

Again the paired echoes are evident. Their positions should be $\pm$0.3 m (low-frequency modulation) and $\pm$1.5 m (high-frequency modulation) relative to the location of the mainlobe. With the aid of (3.36) it can be calculated that the peak level of the paired echoes should be -18 dB relative to the peak level of the mainlobe.

As can be seen from Fig. 3.5, the theoretical values agree very well with the results of the simulation in the case of high-frequency modulation. For low-frequency modulation, the peak level of the paired echoes is much higher than -18 dB. This due to the fact that the peak level is now dominated by the first sidelobes of the original response, which are -13 dB relative to the mainlobe, rather than by the paired echoes.

Moving Target

From Fig. 3.5 it is clear that the shape of the response is not affected when the target is moving. Therefore, the assumptions made to reduce (3.40) to (3.41) seem to be reasonable.
With the aid of (2.5), (2.2), and (2.1), the frequency shift and the corresponding range displacement can be computed from the target's radial velocity. When the target is moving at 45 ms^{-1}, the Doppler frequency shift is 10.5 kHz, resulting in a range displacement of 3.15 m. When the radial velocity is 60 ms^{-1}, the Doppler frequency shift is 14 kHz, leading to a range displacement of 4.2 m. Again the theoretical values agree very well with the results of the simulation.

Recapitulation: The response of an FM-CW radar system to a single point target was derived. Several distortions were introduced and their effects were investigated and, if possible, quantified. The main effects of the system distortions are a loss of resolution (frequency sweep nonlinearities), the appearance of paired echoes (amplitude variations), and the shift in range-frequency of the complete response (moving target). The theoretical findings were validated with a computer simulation. The models used for the system distortions will be implemented in a system simulation in order to estimate and analyze the performance of the FM-CW SAR demonstrator system. The system simulation will be discussed in section 7.4.

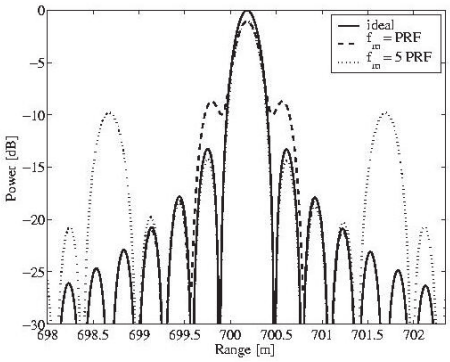

(a) The response of an FM-CW radar when a sinusoidal frequency sweep nonlinearity exists.

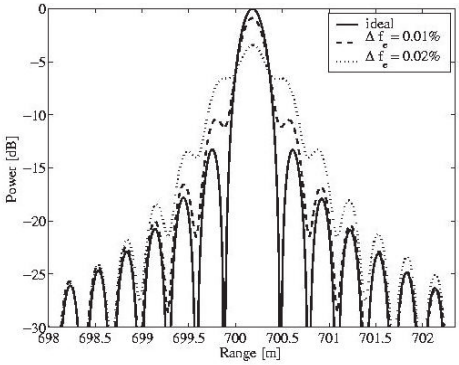

(b) The response of an FM-CW radar when a quadratic frequency sweep nonlinearity exists.

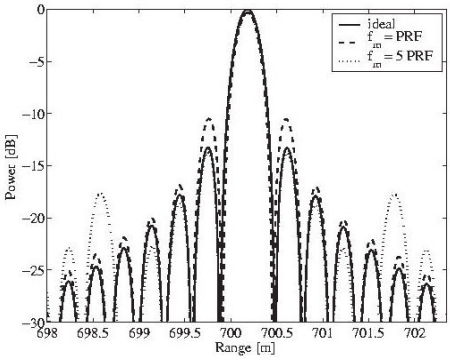

(c) The response of an FM-CW radar when the amplitude of the echo signal is sinusoidally modulated.

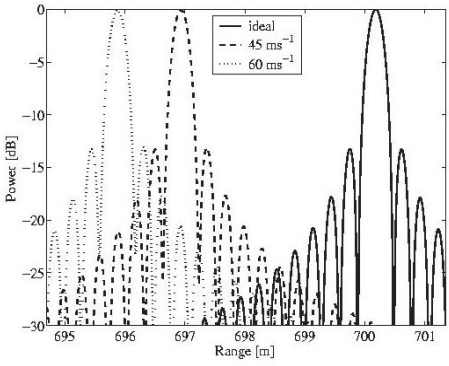

(d) The response of an FM-CW radar when the target is moving.

Figure 3.1: The response of an FM-CW radar to a point target in the presence of different system disturbances.

Chapter 4

Impulse Response of an FM-CW SAR

Overview: In this chapter, the response of an FM-CW SAR system to a single stationary point target will be derived. This derivation will be based on range-Doppler processing. Therefore, in the first section, an overview of the range-Doppler algorithm will be given. In the second section, the response of an FM-CW SAR system will be derived by assuming that the stop-and-go approximation is valid. In the third section, the response will be derived by taking the continuous platform motion into account. An adaptation to the range migration compensation will be proposed in order to compensate the effect of the continuous platform motion. In the final two sections, the effect of phase errors over the SAR observation time will be investigated and the theoretical results will be evaluated with the aid of a computer simulation.

4.1 SAR Processing

As already explained in the introduction, conventional SAR algorithms exploit the stop-and-go approximation. In the case of FM-CW SAR, this approximation may no longer be valid due to the relatively long sweeps that are transmitted.
An FM-CW SAR inverse method taking the continuous motion into account has been developed by Soumekh, [12]. This method is based on the application of a Fourier transform to the complete data set. It takes the *modulated* echo signal as an input. If this method were to be used, the complete bandwidth of the signal should be sampled. For high range resolution applications this would lead to data rates that cannot be handled by current off-the-shelf data acquisition equipment. This FM-CW SAR inverse method seems therefore only practical for low-resolution applications.
When conventional SAR algorithms, such as the range-Doppler algorithm or the ω-k algorithm, [97], are to be applied, the continuous motion should be considered. In order to investigate the effect of continuous motion on the SAR processing, the response of an FM-CW SAR system to a single stationary point target will be derived. This derivation will be based on range-Doppler processing.

Brief Overview of Range-Doppler Processing

The range-Doppler algorithm and modifications to it have already been described by several

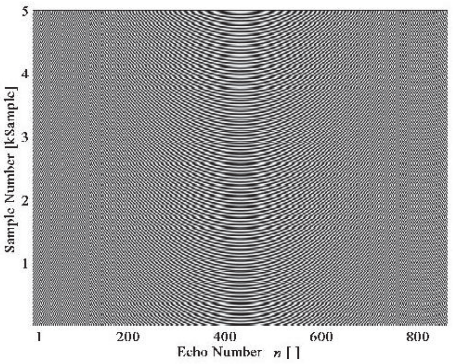

(a) Step 1: The successive demodulated echoes are placed in the columns of the signal matrix. The real part of the signal matrix is shown.

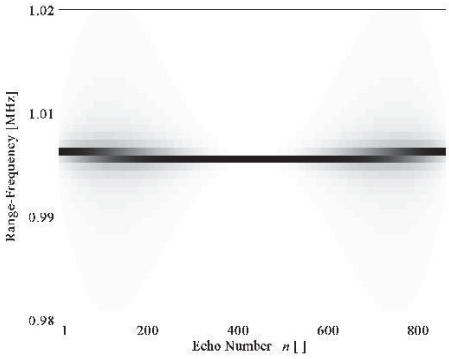

(b) Step 2: The signal matrix is converted to the frequency domain (the absolute value is shown). It can be clearly seen that the response migrates through several range cells during the SAR observation time.

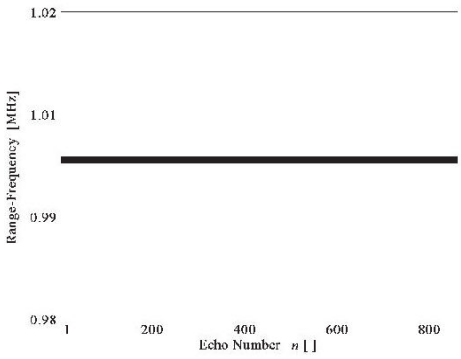

(c) Step 3: The range migration is compensated (the absolute value is shown). The response is now confined to a single range cell for all azimuth positions.

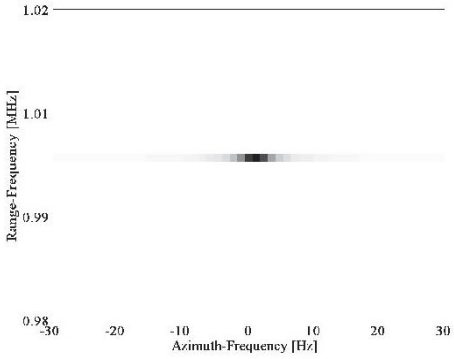

(d) Step 4 and 5: The azimuth phase history is compensated and the signal matrix is converted to the range-Doppler domain (the absolute value is shown).

Figure 4.1: Range-Doppler processing when a single stationary point target is present.

authors, [96]-[99]. In this section, a qualitative, step-by-step review of range-Doppler processing will be given.
As the radar platform flies by the target area, a number of sweeps are transmitted and the corresponding echoes are received. In conventional range-Doppler processing it is assumed that the radar platform is stationary during the transmission of a sweep and the reception of the corresponding echo; the so-called stop-and-go approximation. The received echoes are demodulated and stored. Consequently, a number of echoes are processed to obtain the SAR image. The maximum number of echoes that can be processed depends on the time that the target area is illuminated and thus on the real antenna beamwidth (assuming that the target area is coherent during this time).
The first processing step consists of placing the successive (demodulated) echoes in the columns of a *signal matrix*. This matrix is presented in Fig. 4.1(a). The rows and columns of the signal matrix represent the range cells and azimuth cells respectively.
The second step is the application of a Fourier transform to the columns of the matrix. The demodulated echoes are now converted to the frequency domain, see Fig. 4.1(b).
Since the range to the target is not constant throughout the SAR observation time, the response of a target may migrate through several range cells (several rows of the signal matrix). In that case, the response of the target is spread in range direction in the final SAR image. Therefore, when *range migration* is present, it should be compensated before further processing. The compensation of the range migration is the third processing step. The signal matrix after range migration compensation is shown in Fig. 4.1(c).
Subsequently, the relative phase between the echoes (the columns of the signal matrix) is compensated. The phase compensation is done by multiplication with a reference phase function. The reference phase function can be derived by making use of the known azimuth phase history (2.11). The phase compensation forms the fourth processing step.
Finally, in the fifth step, the signal matrix is converted to the range-Doppler domain by applying a Fourier transform to the rows of the matrix. The final SAR image is shown in Fig. 4.1(d).

4.2 Stop-and-Go Approximation

The response of an FM-CW SAR system to a stationary point target will be developed by assuming that the stop-and-go approximation is valid. Thus the range to the target is supposed to be constant during the transmission of a sweep and the reception of the corresponding echo. The point target is located in the middle of the SAR observation length at a range R_0.
As described in the previous section, in the first step of range-Doppler processing, the consecutive demodulated echoes are placed in a signal matrix. Thus column n contains the beat signal of the echo corresponding to the sweep the transmission of which started at position Az_n. The (discrete) azimuth positions are defined on the interval $[-\frac{1}{2}L_{sar}, \frac{1}{2}L_{sar}]$.
In the second step, a Fourier transform is applied to the columns of the matrix in order to convert the beat signals to the frequency domain. Therefore, at this point, the signals in the columns are given by the response (3.7):

$$S_b(f_R, Az_n) = \gamma V_b \exp[\,\mathrm{j}(\varphi_1 + \varphi_2)]\mathrm{sinc}\big(2\pi\gamma(f_b - f_R)\big)$$

$$+ \gamma V_b \exp[-\mathrm{j}(\varphi_1 + \varphi_2)]\mathrm{sinc}\big(2\pi\gamma(f_b + f_R)\big). \tag{4.1}$$

It should be noted that the time delay is a function of azimuth position and therefore φ_1, φ_2, and f_b are functions of azimuth position as well.
The time instances at which the sweeps were transmitted can be derived from the azimuth positions by:

$$T_n = \frac{Az_n}{v}. \tag{4.2}$$

Thus T_n denotes the time at which the transmission of sweep n started. The time instances are defined on the interval $[-\frac{1}{2}T_{sar}, \frac{1}{2}T_{sar}]$. In the remainder of this chapter, the azimuth dependency will be embodied by T_n rather than Az_n.
In the third processing step, the range migration is compensated. The range migration compensation can be carried out in the range-Doppler domain, since the relation between the Doppler frequency shift and the range migration is unique for each target position, [99].
In order to compensate the range migration, the signal matrix is first converted to the range-Doppler domain by applying a Fourier transform to the rows of the matrix. Subsequently, the range migration is compensated by shifting the range cells by, see appendix B:

$$R_m(R, f_d) = R - R\cos\big(\Phi\big), \tag{4.3}$$

where:

$$\cos\big(\Phi\big) = \sqrt{1 - \Big(\frac{\lambda f_d}{2v}\Big)^2}. \tag{4.4}$$

By taking the SAR geometry into account, the Doppler frequency shift can be expressed as:

$$f_d(T_n) = \frac{2v^2 T_n}{\lambda R}. \tag{4.5}$$

After the completion of the range migration compensation, the signal matrix is converted back to the range-time domain. The maximum of (4.1) on the interval $[0, \frac{1}{2}f_s]$ should now be confined to a single range cell (a single row of the signal matrix) for all azimuth positions.
Since the response is now confined to a single range cell, the response in azimuth direction can be derived. To do so, the maximum of (4.1) on the interval $[0, \frac{1}{2}f_s]$, that is $f_R = f_b$, should be considered:

$$\begin{aligned} s_{Az}(T_n) &= \gamma V_b \exp[\,\mathrm{j}(\varphi_1 + \varphi_2)] \\ &\quad + \gamma V_b \exp[-\mathrm{j}(\varphi_1 + \varphi_2)]\mathrm{sinc}\big(4\pi\gamma f_b\big). \end{aligned} \tag{4.6}$$

In order to clarify the derivation, (4.6) is approximated by:

$$s_{Az}(T_n) \approx \gamma V_b \exp[\,\mathrm{j}(\varphi_1 + \varphi_2)]. \tag{4.7}$$

This approximation seems reasonable, since the second term on the right hand side of (4.6) is very small.
The amplitude of (4.7) is assumed to be constant throughout the SAR observation time. The phase terms φ_1 and φ_2 are however not constant, hence they affect the azimuth resolution.

Consequently, these phase terms should be accounted for.
The term φ_2 is a consequence of the demodulation process, similar to the *residual video phase* (RVP) in dechirp-on-receive pulse SAR systems, [83]. Compensation of the RVP is possible, but in most situations the effect of the RVP is negligible. For reasons of clarity, it is assumed that the RVP is compensated. In that case, by making use of (3.8), (2.13), and (2.1), (4.7) can be reduced to:

$$s_{Az}(T_n) \approx \gamma V_b \exp\big[\,\mathrm{j}\frac{4\pi}{\lambda}\big(R_0 + \frac{v^2 T_n^2}{2R_0}\big)\big]. \tag{4.8}$$

As can be seen, the phase of (4.8) is indeed equal to the azimuth phase history (2.11).
The fourth step of range-Doppler processing consists of the compensation of the relative phase between the successive echoes; that is the compensation of the quadratic phase term of (4.8). The quadratic phase term is easily compensated by multiplication with the azimuth reference phase function:

$$\varphi_{Az}^{ref}(T_n) = \exp\big[-\mathrm{j}\frac{4\pi}{\lambda}\frac{v^2 T_n^2}{2R_0}\big], \tag{4.9}$$

which can be derived from (2.11) and (4.8). The compensation of the relative phase between the echoes reduces (4.8) to:

$$s_{Az}(T_n) \approx \gamma V_b \exp\big[\,\mathrm{j}\frac{4\pi}{\lambda}R_0\big]. \tag{4.10}$$

Now it is interesting to note the similarity between FM-CW signaling and SAR signaling. The 'echo' signal in azimuth direction (4.8) has, just as the echo signal in range direction (3.2), a linearly modulated frequency. The procedure of compensating the relative phase between the successive echoes (in azimuth direction) is equivalent to the demodulation of the echo signal with a nondelayed replica of the transmitted signal (in range direction).
The fifth and final step of range-Doppler processing is the conversion to the range-Doppler domain. The signal matrix is transformed to the range-Doppler domain by applying a Fourier transform with respect to T_n to the rows of the matrix. Thus finally, the response in azimuth direction follows as:

$$S_{Az}(f_{Az}) = \gamma V_b T_{sar} \exp\big[\,\mathrm{j}\frac{4\pi R_0}{\lambda}\big]\mathrm{sinc}\big(\pi T_{sar} f_{Az}\big), \tag{4.11}$$

where f_{Az} denotes azimuth-frequency, defined on the interval $[-\frac{1}{2}PRF, \frac{1}{2}PRF]$. As can be seen, the maximum of (4.11) is located at $f_{Az} = 0$; that is indeed in the middle of the SAR image.
Thus far it was assumed that the point target is located in the middle of the SAR observation length at a range R_0. In the following subsection, the response to a target that is located at the same range R_0, but that is displaced in azimuth direction, will be derived.

Target Displaced in Azimuth Direction

When a target is displaced in azimuth direction, the range to the target is still described by (2.13), apart from a shift in time. The time shift depends on the target's azimuth position:

$$R_N(T_n) \approx R_0 + \frac{v^2(T_n + Az_N/v)^2}{2R_0}, \tag{4.12}$$

in which Az_N is the target's azimuth position.
By using (4.12), the 'echo' signal in azimuth direction (4.8) can be rewritten as:

$$s_{Az}(T_n) \approx \gamma V_b \exp\big[\,\mathrm{j}\frac{4\pi}{\lambda}\big(R_0 + \frac{v^2(T_n + Az_N/v)^2}{2R_0}\big)\big]. \tag{4.13}$$

Subsequently, the compensation of the relative phase between the consecutive echoes, with the aid of (4.9), results in:

$$s_{Az}(T_n) \approx \gamma V_b \exp\big[\,\mathrm{j}\frac{4\pi}{\lambda}\big(R_0 + \frac{Az_N^2}{2R_0}\big)\big] \exp\big[\,\mathrm{j}\frac{4\pi}{\lambda}\frac{vAz_N}{R_0}T_n\big]. \tag{4.14}$$

Finally, after conversion to the range-Doppler domain, the response in azimuth direction follows as:

$$S_{Az}(f_{Az}) = \gamma V_b T_{sar} \exp\big[\,\mathrm{j}\frac{4\pi}{\lambda}\big(R_0 + \frac{Az_N^2}{2R_0}\big)\big]\mathrm{sinc}\big(\pi T_{sar}\big(\frac{2vAz_N}{\lambda R_0} - f_{Az}\big)\big). \tag{4.15}$$

As can be seen, the maximum of (4.15) is located at $f_{Az} = 2vAz_N/(\lambda R_0)$. The azimuth-frequency can be converted to azimuth position with the aid of the inverse of (4.5):

$$f_{Az} = \frac{2v^2T_n}{\lambda R_0} = \frac{2vAz_n}{\lambda R_0} \Longrightarrow Az_n = \frac{\lambda R_0}{2v} f_{Az}, \tag{4.16}$$

and thus the maximum of (4.15) is indeed located at Az_N. It should be noted that the conversion from Doppler frequency shift to azimuth position depends upon the target's range.

4.3 Continuous Motion

The response to a single stationary point target will be derived by taking the continuous motion of the radar platform into account. Again it is assumed that the point target is located in the middle of the SAR observation length at a range R_0.
The situation of a moving platform is similar to the situation of a moving target. Therefore, the derivation starts with the beat signal in the case that a moving target is present, (3.41):

$$s_b(t) = V_b \cos\big(\frac{2\pi\Delta f}{PRI}\Delta t_0\, t + 2\pi f_d t + 2\pi f_c \Delta t_0 - \frac{\pi\Delta f}{PRI}\Delta t_0^2\big). \tag{4.17}$$

The Doppler frequency shift is assumed to be constant during the transmission of a sweep and the reception of the corresponding echo. In that case, as it was already concluded in section 3.4, the response is shifted in range, but the shape of the response is not affected. Since the range shift depends on the Doppler frequency shift, it varies during the SAR observation time. By taking the range shift into account, the *measured* range throughout the SAR observation time can be written as:

$$R(t) = \sqrt{R_0^2 + v^2t^2} + \frac{cPRI}{2\Delta f} f_d. \tag{4.18}$$

As can be seen, the range shift is a function of the Doppler frequency shift only (no dependence on R_0). Therefore, the range shift can be compensated in the range-Doppler domain.

This is an important observation, since the range shift can now be treated as an additional term to the range migration.
By adapting the range migration compensation (4.3) to:

$$R_m(R, f_d)' = R - R\cos(\Phi) + \frac{cPRI}{2\Delta f} f_d, \tag{4.19}$$

the range migration and the range shift due to the Doppler frequency shift are compensated in the same procedure, without introducing an additional processing step. Furthermore, it should be possible to implement a similar adaptation to the range migration compensation in other SAR processing algorithms such as the ω-k algorithm.
Finally, when the Doppler frequency shift is compensated, the response after SAR processing is again given as (4.11). The theoretical results will be evaluated with the aid of a computer simulation in section 4.5.

4.4 SAR Phase Errors

Successful SAR processing relies on the fact that there is a known phase relationship between successive sweeps. In practice, undesirable phase effects or *phase errors* distort the phase history. Possible causes for such undesirable phase effects are, among others, atmospheric influences on the propagation path, frequency dispersion in system components, and transmission line reflections. However, these effects are generally very small and usually they are neglected. As already mentioned in section 2.4, the main sources of phase errors are inaccuracies in the measurements of the platform position, velocity, and acceleration.
Phase errors degrade the image quality in several ways depending upon their nature. They are classified as either low-frequency or high-frequency. Low-frequency phase errors vary slowly compared to the SAR observation time, whereas high-frequency errors vary very fast compared to the SAR observation time. In this section, the upper limits to different classes of uncompensated phase errors will be derived, by making use of the similarities between FM-CW signaling and SAR signaling.

Low-Frequency Linear Phase Error

When a low-frequency linear phase error exists over the SAR observation time, then the phase of (4.10) should be adapted to:

$$\varphi_b(T_n) = \frac{4\pi}{\lambda} R_0 + \frac{\varphi_e}{T_{sar}} T_n, \tag{4.20}$$

where φ_e is the full phase error over the SAR observation time. The form of (4.20) is similar to the phase of (3.41). It can therefore be concluded that a linear phase error results in an azimuth displacement, but that it does not degrade image quality. Only if the phase error varies with target position, the SAR image will be distorted.
The linear phase error results in a frequency shift of:

$$f_e = \frac{1}{2\pi} \frac{\varphi_e}{T_{sar}}, \tag{4.21}$$

that leads to an azimuth displacement of:

$$\Delta Az = \frac{\lambda R_0}{4\pi v}\frac{\varphi_e}{T_{sar}}. \tag{4.22}$$

In order to limit the azimuth displacement to a resolution cell, the full phase error over the SAR observation time should be limited to:

$$\varphi_e \leq 2\pi. \tag{4.23}$$

Low-Frequency Quadratic Phase Error

When a low-frequency quadratic phase error is present, the phase of (4.10) should be rewritten as:

$$\varphi_b(T_n) = \frac{4\pi}{\lambda}R_0 + \frac{\varphi_e}{\left(T_{sar}/2\right)^2}T_n^2, \tag{4.24}$$

where φ_e is the maximum of the quadratic phase error. As can be seen, (4.24) has the same form as (3.27). Therefore, a quadratic phase error over the SAR observation time leads to a loss of resolution. The loss of resolution can be estimated in a similar way as was done in section 3.2.
The instantaneous beat frequency follows as the derivative of (4.24) divided by 2π:

$$f_{b,i}(T_n) = \frac{\varphi_e}{\pi\left(T_{sar}/2\right)^2}T_n. \tag{4.25}$$

Then the total variation of the beat frequency over the SAR observation interval $[-\frac{1}{2}T_{sar}, \frac{1}{2}T_{sar}]$ can be calculated:

$$\Delta f_b = \frac{4\varphi_e}{\pi T_{sar}}. \tag{4.26}$$

Thus for a maximum resolution loss of 10 %:

$$\frac{\sqrt{\left(1/T_{sar}\right)^2 + \Delta f_b^2}}{\sqrt{\left(1/T_{sar}\right)^2}} \leq 1.1, \tag{4.27}$$

which can be rewritten as:

$$\varphi_e \leq \frac{\sqrt{0.21}\,\pi}{4}, \tag{4.28}$$

with the aid of (4.26).
The application of a windowing function reduces the effective measurement time and therefore it reduces the effect of a quadratic phase error as well. When windowing is applied, the quadratic phase error should be bounded by $\pi/2$ to limit the loss of resolution to 10 %, [94].

Low-Frequency Cubic Phase Error

Low-frequency cubic phase errors cause asymmetric sidelobes in azimuth direction, [83]. They should be bounded by π, [85].

High-Frequency Sinusoidal Phase Error

A sinusoidal phase error can be written as:

$$\varphi_e = \frac{4\pi A_{vib}}{\lambda}\cos\big(2\pi f_m t\big), \tag{4.29}$$

which is of the same form as the phase error caused by a sinusoidal sweep nonlinearity. Thus, a high-frequency sinusoidal phase error over the SAR observation time results in paired echoes around the original response.
With the aid of (3.16) and (3.19), the sidelobe peak level to mainlobe peak level ratio follows as:

$$20\cdot{}^{10}\log\big(\frac{4\pi A_{vib}}{2\lambda}\big). \tag{4.30}$$

Therefore, in order to limit the peak sidelobe level to p dB relative to the peak main lobe level, the amplitude of the vibrations should be bounded by:

$$A_{vib} = \frac{\lambda}{2\pi}10^{\frac{p}{20}}. \tag{4.31}$$

However, in practice, system vibrations are likely to vary with azimuth position. SAR processing will therefore not focus the paired echoes, [83].

High-Frequency Wideband Phase Error

Wideband phase errors smear out the energy, causing image contrast degradation. This effect is usually quantified by the increase in the integrated-sidelobe-ratio (ISLR). The increase in ISLR due to a wideband phase error is approximately, [83]:

$$\frac{\text{increase in sidelobe energy}}{\text{mainlobe energy}} \approx \sigma_e^2, \tag{4.32}$$

where σ_e^2 is the root mean square value of the wideband phase error. The root mean square value should be significantly smaller than $\pi/2$.

4.5 Impulse Response Simulation

The response of an FM-CW SAR system to a single stationary point target has been simulated in order to validate the theoretical results. The system parameters and measurement geometry used in the simulation are listed in table 3.1. In the simulation range-Doppler processing is applied.
The simulation has been carried out for different platform velocities ranging from 30 m/s to 120 m/s. For the system parameters used in the simulation the maximum velocity is 120 m/s. At higher velocities the data are undersampled in azimuth direction.
From Fig. 4.2(a) it can be seen that the shape of the response in range direction is not affected by the platform motion. Even at a velocity as high as 240 m/s, the response is not degraded. The expected shift in range due to the Doppler frequency shift is however apparent. Therefore, the assumptions made to reduce (3.40) to (3.41) seem to be valid for a wide range of platform velocities.

In azimuth direction the response degrades at higher velocities when range-Doppler processing without range migration compensation is applied, as can be seen from Fig. 4.2(b). Energy is lost (ideally the peak level should be 0 dB), since the responses are not confined to a single range cell. At higher platform velocities more energy is lost because the variation of the Doppler frequency shift throughout the SAR observation time is larger.
When the range migration is compensated no energy is lost at 30 m/s, see Fig. 4.2(c). Thus at 30 m/s the effect of the continuous motion is in fact negligible. At the higher velocities, the responses still migrate through several range cells due to the Doppler frequency shift. Therefore, some energy is still lost at the higher platform velocities.
Finally, from Fig. 4.2(d) can be concluded that no energy is lost when both the range migration and the Doppler frequency shift are compensated. The responses are now confined to a single range cell at all velocities. Furthermore, the figure shows that, as expected from the SAR theory, the azimuth resolution is independent of platform velocity.
Under normal conditions, the FM-CW SAR demonstrator system will be flown at 30 m/s. In that case, the continuous platform motion has only a minor effect (see Fig. 4.2(b)). Even at the glider's maximum cruise speed of 61 m/s, the effect should be small. The compensation of the Doppler frequency shift may however be necessary whenk other types of aircraft are used. The cruise speed of for instance the Cessna Citation II, used to fly the PHARUS system, is around 150 m/s.

Recapitulation: The response of an FM-CW SAR system to a single stationary point target was developed. Due to the relatively long sweeps that an FM-CW radar transmits, the stop-and-go approximation is no longer valid. Therefore, the continuous platform motion, inducing a Doppler frequency shift throughout the SAR observation time, should be taken into account. (However, for the FM-CW SAR demonstrator system the Doppler frequency shift will be negligible due to the very low platform velocity.) An adaptation to the range migration compensation procedure was proposed in order to compensate the Doppler frequency shift in the same process. The adapted range migration compensation was implemented in a range-Doppler algorithm, but it should be feasible to make a comparable modification to other SAR algorithms. Finally, the bounds to different classes of phase errors were established by making use of the similarities between FM-CW and SAR signaling. The theoretical results were validated with the aid of a computer simulation.

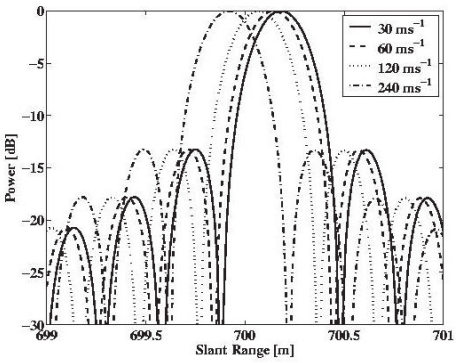

(a) Cross section in range direction after range-Doppler processing.

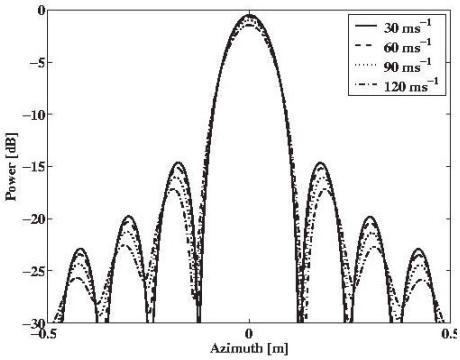

(b) Cross section in azimuth direction after range-Doppler processing.

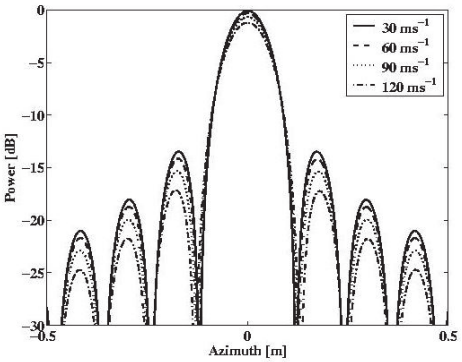

(c) Cross section in azimuth direction after range-Doppler processing and range migration compensation.

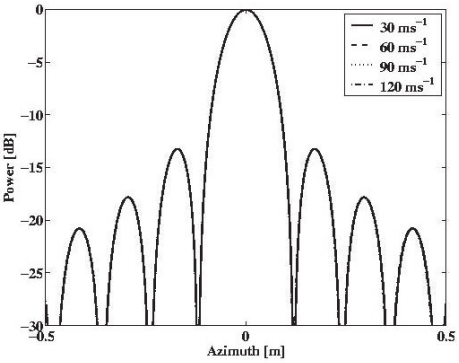

(d) Cross section in azimuth direction after range-Doppler processing and range migration and Doppler frequency shift compensation.

Figure 4.2: Cross sections of the responses.

Chapter 5

Signal-to-Noise Ratio

Overview: In this chapter, expressions for the different noise constituents and the available signal power will be developed. With the aid of these expressions, the SNR will be derived and subsequently the effect of SAR processing on the SNR will be quantified.

5.1 Total Available Noise Power

The expressions for the different noise constituents will be derived by making use of the schematic receiver chain shown in Fig. 5.1. The gains and noise figures of the separate blocks and the overall gain and overall noise figure are pointed out in the diagram.

Thermal Noise Power

The thermal noise power available at the input of the A/D board (that is point 3 in the block diagram) can be written as, [40]:

$$N_t = k\,T_0\,B \cdot F \cdot G \qquad [\mathrm{W}], \tag{5.1}$$

where k is Boltzmann's constant, $T_0 = 290$ K is the standard temperature, and B, F, and G are the bandwidth, the overall noise figure, and the overall gain of the complete receiver chain respectively.

Phase Noise Power

In the computation of the phase noise it is assumed that the direct coupling is the main contributor to the phase noise in the frequency band of interest. The phase noise power related to the direct coupling at the input of the receiver/mixer combination (that is point 1) is given as:

$$N_{p1} = \frac{P_t N_{osc}(f_m)}{\chi} \qquad [\mathrm{W/Hz}], \tag{5.2}$$

in which P_t is the transmitted power, $N_{osc}(f_m)$ is the oscillator phase noise at a frequency offset f_m relative to the carrier frequency, and χ is the antenna isolation.
As already explained in section 2.2, the phase noise is reduced due to the range correlation effect if a fraction of the transmitted signal is used as LO signal in the receiver. Due to the

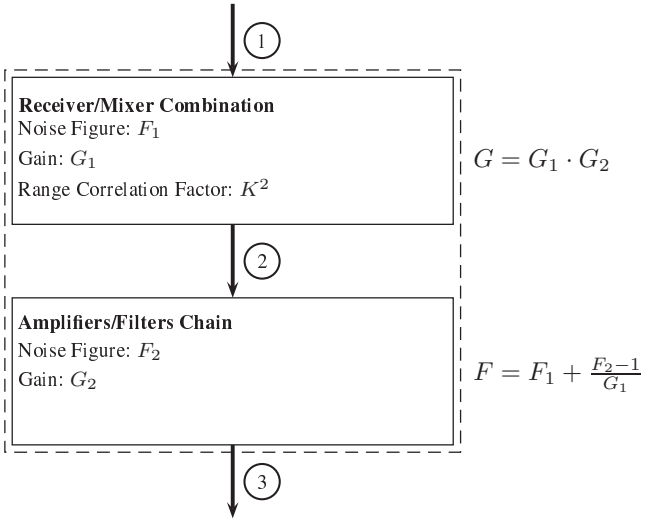

Figure 5.1: The noise figures and the gains of the different blocks of the receiver chain.

range correlation effect, the phase noise power is modified by the *range correlation factor*, [60]-[67]:

$$K^2 = 4\sin^2(\pi f_m \Delta t) \qquad [\,], \tag{5.3}$$

in which Δt is the total time delay of the direct-coupled signal. The derivation of the range correlation factor will be reviewed in appendix C.
The phase noise power at the input of the A/D board (that is point 3) follows as:

$$N_p = N_{p1} B \cdot K^2 \cdot G \qquad [\mathrm{W}]. \tag{5.4}$$

In the derivation of (5.4) it is assumed that the phase noise contribution of the components of the receiver chain is negligible compared to the phase noise related to the direct coupling.

Quantization Noise Power

The quantization noise power can be written as, [101]:

$$N_q = \frac{q^2}{12} \qquad [\mathrm{W}], \tag{5.5}$$

where q is the quantization interval. In general, (5.5) is valid if the signal is fairly random and if a large number of quantization steps are available.

Total Noise Power

By combining (5.1), (5.4), and (5.5), the total available noise power after digitalization of the beat signal can be written as:

$$N_{AD} = N_t + N_p + N_q \qquad [\mathrm{W}]. \tag{5.6}$$

5.2 Available Signal Power

An expression for the available signal power at the A/D board's input will be derived. The signal power at the input of the receiver/mixer combination (that is point 1) is given as, [40]:

$$P_r = \frac{P_t\, G_{ant}^2 \lambda^2 \sigma}{(4\pi)^3 R^4 L_a} \qquad [\mathrm{W}], \tag{5.7}$$

where G_{ant} is the antenna gain, σ is the target's radar cross section (RCS), and L_a represents attenuation by atmospheric gasses.
Subsequently, the signal power at the input of the A/D board (that is point 3) follows as:

$$P_{AD} = P_r \cdot G \qquad [\mathrm{W}]. \tag{5.8}$$

5.3 Signal-to-Noise Ratio

By combining (5.6) and (5.8), the SNR after the digitalization of the beat signal can be written as:

$$SNR_{AD} = \frac{P_{AD}}{N_{AD}} \qquad [\,]. \tag{5.9}$$

Eq. 5.9 represents the SNR before any signal processing has been applied. In order to obtain an estimation of the SNR of the final SAR image, the effects of the signal processing should be taken into account. In the following subsections, the effects of the different processing steps of the range-Doppler algorithm, as already described in section 4.1, will be quantified.

The SNR after the Application of an FFT

In the first processing step, the successive demodulated echoes are placed in a matrix. In the second step, the signal matrix is converted to the frequency domain by performing an FFT.
If a rectangular windowing function is applied, the FFT[†] introduces a *coherent power gain* of $(n_s/2)^2$, [102]. Note that only $n_s/2$ samples are taken into account, since applying an FFT to a real-valued signal leads to a symmetrical frequency spectrum. Consequently, after the application of an FFT, the signal peak power is given as:

$$P_{FFT} = P_{AD} \cdot \left(\frac{n_s}{2}\right)^2 \qquad [\mathrm{W}]. \tag{5.10}$$

The FFT introduces a *dc gain* of a factor of only $n_s/2$, [102]. Therefore, the noise power after the application of an FFT follows as:

$$N_{FFT} = N_{AD} \cdot \frac{n_s}{2} \qquad [\mathrm{W}]. \tag{5.11}$$

Finally, with the aid of (5.10) and (5.11), the SNR after the application of the FFT can be written as:

$$SNR_{FFT} = SNR_{AD} \cdot \frac{2n_s^2}{4n_s} \qquad [\,]. \tag{5.12}$$

[†]The signal processing algorithms were implemented in The Mathworks Matlab. In Matlab, the discrete Fourier transform is defined as:
$x(f) = \sum_{n=1}^{N} x(n) \exp[-j2\pi(f-1)(n-1)/N]$.

The SNR after SAR Processing

In terms of SNR, focused SAR processing of n_e echoes is equivalent to the coherent summation of n_e echoes. If the signal is fully coherent from one echo to the other, focused SAR processing increases the signal peak power by a factor of n_e^2, [103]:

$$P_{sar} = P_{FFT} \cdot n_e^2 \qquad [\mathrm{W}]. \tag{5.13}$$

Since the noise is incoherent from echo to echo, focused SAR processing increases the noise power by a factor of only n_e, [103]:

$$N_{sar} = N_{FFT} \cdot n_e \qquad [\mathrm{W}]. \tag{5.14}$$

The echoes from a stationary target such as a corner reflector are assumed to be coherent from one echo to the other. Therefore, focused SAR processing increases the SNR by a factor of n_e:

$$SNR_{sar} = SNR_{FFT} \cdot \frac{n_e^2}{n_e} \qquad [\,]. \tag{5.15}$$

Recapitulation: Expressions for the different noise constituents, the available signal power, and the SNR before and after FM-CW SAR signal processing were derived. These expressions will be used in chapter 7 to calculate the expected SNR for several specific measurement geometries.

Chapter 6

FM-CW SAR System Description

Overview: In this chapter, the initial requirements to the FM-CW SAR demonstrator system will be given. Subsequently, the design of the front end and the selection of the motion sensors will be discussed. Finally, a description of the complete FM-CW SAR demonstrator system will be given.

6.1 Requirements and Boundary Conditions

The main objective of the project is to show the feasibility of FM-CW SAR in the field of airborne earth observation. Additionally, an operational demonstrator system should prove that an FM-CW SAR system could indeed be operated in an efficient and cost effective manner from a very small airborne platform.
The demonstrator system should be capable of operating in two modes: a high-resolution mode and a survey mode. In the high-resolution mode the resolution in range direction as well as in azimuth direction should be 30 cm. The ground swath should be at least 500 m. In the survey mode the ground swath should be larger at the cost of resolution.
It is assumed that the velocity of existing small aircraft is between 100 and 250 km/hr and that the operational altitude of such platforms is between 300 m and 5 km. The Stemme S10 motor glider, manufactured by Stemme GmbH, fulfills these requirements and moreover it provides a relatively cheap test platform. Therefore, the demonstrator system should be tailored to this glider.
The S10 is a twin seat, light surveillance glider that can stay airborne for 8 hours, [38]. The maximum altitude is about 7.5 km, the minimum velocity is around 30 m/s, and the maximum velocity is 61 m/s. For the glider standardized under wing pods are available. These pods have a diameter of about 35 cm and an effective length of 80 cm. The maximum payload is 50 kg. The complete demonstrator system should be fitted in such a pod. Nevertheless, it should be possible to monitor and control the system from the cockpit. To this end, some cables can be pulled through the wing to the cockpit.
After the airborne experiments, the performance of the demonstrator system should be evaluated and the system design should be improved. This improved system design should then facilitate the development of a future higher performance FM-CW SAR system. The requirements to the FM-CW SAR demonstrator system and the future target system are summarized

Table 6.1: The FM-CW SAR demonstrator system requirements.

	High Res. Mode	**Survey Mode**	**Target System**
Imaging Mode:	Stripmap	Stripmap	Stripmap
Range Res.:	30 cm	50 cm	$\leq$ 30 cm
Azimuth Res.:	30 cm	50 cm	$\leq$ 30 cm
Ground Swath:	500 m	$>$ 500 m	$\geq$ 1000 m
Min. Range:	350 m		
Max. Range:	800 m		
Altitude:	250 m		250 to 1000 m
Velocity:	150 km/hr	150 km/hr	50 to 250 km/hr

in table 6.1.

6.2 The 35 GHz Front End Design

The 35 GHz FM-CW front end was manufactured by Epsilon-Lambda Electronics Inc. Other manufacturers were approached as well, but they were not prepared to build a single customized front end. Developing the front end in-house was expected to take too long and to be more expensive.
The specifications of the front end are listed in table 6.2. In close consultation with Epsilon-Lambda, the front end was, to some extend, customized to our needs. The system parameters that could be customized were the antenna beamwidth (in both azimuth and range direction) and the maximum frequency sweep. In the following subsections, the design considerations regarding these parameters will be discussed.

Azimuth: Beamwidth and Sampling Requirements

In the high-resolution mode, the practical resolution should be 30 cm. In the system design, a theoretical resolution of 10 cm is anticipated. In that case, three resolution cells can be averaged in order to reduce speckle. In order to obtain 10 cm resolution, the antenna beamwidth in azimuth direction should be (by using (2.16)):

$$\theta_{Az} \geq \frac{\lambda}{2\delta Az_{sar}} = 2.5^{\circ}. \tag{6.1}$$

However, according to the preliminary antenna design, the front end would be too large to fit in the pod when the beamwidth were to be 2.5°. Moreover, when the beamwidth is just sufficient to obtain the required resolution, yaw variations of the platform cannot be compensated. Therefore, in consultation with the manufacturer, a wider beam of 6° was agreed upon.
By taking the beamwidth of 6° into consideration and by making use of (2.19), the required

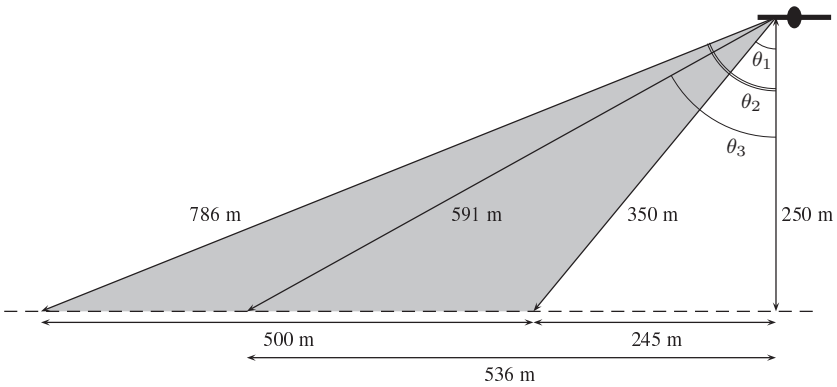

Figure 6.1: Front view of the SAR geometry in the high-resolution mode.

sample rate in azimuth direction is:

$$PRF \geq \frac{2v\theta_{Az}}{\lambda} = 733 \text{ Hz}, \tag{6.2}$$

where $v = 30$ m/s. It was decided to use a 1 kHz sawtooth frequency modulation. For a *PRF* of 1 kHz, the maximum platform velocity is around 40 m/s.

Range: Beamwidth and Sampling Requirements

The measurement geometry in the case of the high-resolution mode is depicted in Fig. 6.1. With the aid of this figure it can be easily calculated that the angle of incidence for near range is:

$$\cos(\theta_1) = \frac{250}{350} \Longrightarrow \theta_1 = 44^\circ, \tag{6.3}$$

whereas the angle of incidence for far range is:

$$\tan(\theta_2) = \frac{500 + 245}{250} \Longrightarrow \theta_2 = 71^\circ. \tag{6.4}$$

Hence the required beamwidth in range direction is 27°.
The angle of incidence to the middle of the ground swath is 63°. It was decided to direct the antenna main beam slightly towards the far end of the swath. In that case, the antenna gain is higher for far range than for near range, partly compensating the difference in received power due to the difference in range. The angle of incidence of the antenna main beam, indicated by θ_3 in Fig. 6.1, was chosen to be 65°.
In the high-resolution mode, the range resolution should be 30 cm. Then, by applying (2.4), the required frequency sweep follows as:

$$\Delta f \geq \frac{c}{2\delta r} = 500 \text{ MHz}. \tag{6.5}$$

For a 1 kHz sawtooth modulation and a frequency sweep of 500 MHz, the required sweep rate is 500 MHz/ms. Thus the required sweep rate complies with the specifications of the front end, see table 6.2.
By making use of (2.2) and (2.1), the maximum beat frequency follows as:

$$f_{b,max} = \frac{\Delta f}{PRI}\frac{2R_{max}}{c} = 2.62\,\text{MHz}. \tag{6.6}$$

The sample rate was set to 6.6 MHz. However, the first laboratory tests with the complete system set up showed that the demonstrator system could not handle the high data rates and as a result the system became unstable. This problem was solved by lowering the sample rate to 5 MHz. As a consequence, the maximum beat frequency that can be unambiguously sampled is only 2.5 MHz. Therefore, in the high-resolution mode, the measurement range is limited to 731 m.
The minimum beat frequency is:

$$f_{b,min} = \frac{\Delta f}{PRI}\frac{2R_{min}}{c} = 1.16\,\text{MHz}. \tag{6.7}$$

Consequently, the required IF band is 1.16 MHz to 2.5 MHz, which is in compliance with the specifications of the front end, see table 6.2.
At far range, the range migration is about 19 cm; that is of the order of half a resolution cell. Therefore, a SAR image of good quality may be obtained even without range migration compensation.

The Front End's Linearization Loop

The tuning characteristic of the VCO is highly nonlinear. Therefore, the front end is supplied with a linearization loop that phase-locks the VCO to a stable dielectric resonant oscillator. The linearization loop is however very slow, after fast frequency transitions, it requires a re-lock time of the order of a third of the *PRI*, [104]. The manufacturer was asked to provide the possibility to switch off the linearization loop, also because it was anticipated that the nonlinear behavior could be compensated by applying an adapted sweep control signal, see section 7.1.

Preliminary Performance Analysis

With the aid of the system specifications listed in table 6.2, a preliminary performance analysis was made, [105]-[106]. From this analysis it was concluded that the sensitivity of the front end is not sufficient to produce SAR images of acceptable quality of areas that have a low RCS per unit area, such as grasslands, shrubbery, or wooded areas. Nevertheless, SAR imaging by using radar reflectors that have a large RCS should be feasible. A high quality SAR image of several reflectors would suffice for at least a proof of principle. Therefore, it was decided to purchase the front end, also because no other candidates were available.

6.3 Motion Recording

As already explained, SAR processing makes use of the known phase history between the successive echoes. The phase history is however distorted when the radar platform deviates

Table 6.2: The specifications of the Epsilon-Lambda front end. The specifications marked with * only apply if the linearization loop is used.

Parameter	**Front End Design**
*Center Frequency:	35.25 GHz
*Max. Frequency Sweep:	500 MHz
Max. Sweep Rate:	500 MHz/ms
*Linearity:	< 0.3 %
*Linearizer Relock Time:	< 340 μs
Transmitted Power:	18.5 dBm
Power Variation:	$\pm$ 0.7 dB over Sweep
Phase Noise at 100 kHz: (free running oscillator)	-75 dBc/Hz
*Phase Noise at 1 MHz:	-93 dBc/Hz
Phase Noise at 10 MHz:	-105 dBc/Hz
Receiver Noise Figure:	6.9 dB
System Losses:	< 1.5 dB
Conversion Loss:	< 8 dB
Return Loss:	< 15 dB
Dynamic Range:	> 80 dB
IF Band:	0.5 to 3 MHz
IF Impedance:	50 Ω
Preamplifier Gain:	21 dB
Preamplifier Noise Figure:	2.2 dB
Antenna Type:	Horn Lens
Antenna Gain:	> 24.3 dB
Antenna Isolation:	52 dB
Beamwidth Azimuth:	6°
Beamwidth Range:	28°
First Sidelobe:	> 17.5 dB down
Overall Size:	23.3 x 14 x 9 cm

from the ideal straight flight track. In order to compensate the phase of the echoes for these deviations, it is required to precisely measure the position, velocity, and attitude of the platform throughout the SAR observation time.
The position and velocity of the glider can be accurately measured with the aid of a Global Positioning System (GPS) receiver. However, just a GPS receiver would not suffice; low-cost GPS receivers update their position and velocity only once every second, [107]. For the SAR processing, it is required that the position of the glider is accurately known for each transmitted sweep. Moreover, with a single GPS receiver, the attitude of the glider can not be determined.
Therefore, the demonstrator system should be extended with analog gyroscopes and analog accelerometers. By integrating the measurements of the accelerometers twice and those of the gyroscopes once, the position and the attitude of the glider can be determined. Although accelerometers and gyroscopes are generally very accurate, the errors in the calculated position and attitude may accumulate rapidly due to the integration. Hence, the use of only gyroscopes and accelerometers is not sufficient to obtain an accurate assessment of the position and attitude on a long-term (moreover, the *absolute* position and attitude cannot be determined with just an accelerometer and gyroscopes).
The position calculated from the accelerometer data can be regularly updated using the readings of the GPS receiver. The calculated attitude can be updated by using measurements of a magnetometer. However, low-cost magnetometers are not accurate enough to obtain useful measurements of the attitude. Due to the limited utility it was decided not to purchase a magnetometer. Fortunately, precise knowledge of the attitude of the glider is not mandatory for successful SAR processing.
Roll affects the SAR processing if the roll angle is so large that the antenna main beam is no longer pointing at the area of interest. In the case of the FM-CW SAR demonstrator, the antenna beam in range direction is very wide. Thus moderate roll angles will not affect the SAR processing.
Yaw and pitch give rise to an additional Doppler frequency shift throughout the SAR observation time (yaw being the most important). As a consequence, the complete azimuth response (4.11) is shifted in frequency. Therefore, a large yaw angle may lead to undersampling in azimuth direction. A modest yaw angle will not affect the SAR processing. Moreover, a small yaw angle can be estimated from the measured data themselves and consequently it can be compensated, [31].

Selection of the Motion Sensors

In the design stage of the project, an extensive survey of off-the-shelf motion sensors was made, [108]. In order to be able to select a suitable combination of gyroscopes and accelerometers, their performance should be evaluated with the aid of the upper limits established in section 2.4. In [92], a method is described to calculate the error spectrums of a gyroscope/accelerometer combination for the different angular and lateral motion components. Subsequently, the error spectrums can be weighted against the upper limits set to the different motion components. This method will be briefly reviewed in appendix D.
After the evaluation of several gyroscope/accelerometer combinations, the Systron AQRS gyroscope and the Crossbow CLX02LF3 accelerometer were selected, [104]. The error spec-

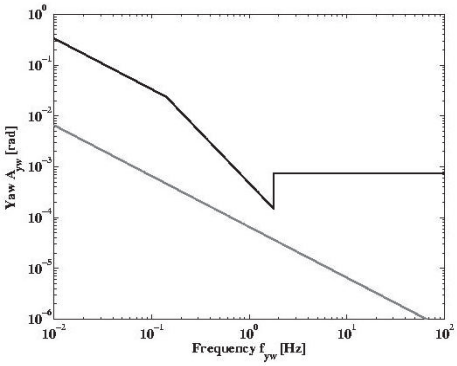

(a) The upper bound to the amplitude of sinusoidal yaw variations (black) and the error spectrum of the angle of the selected combination of motion sensors (gray).

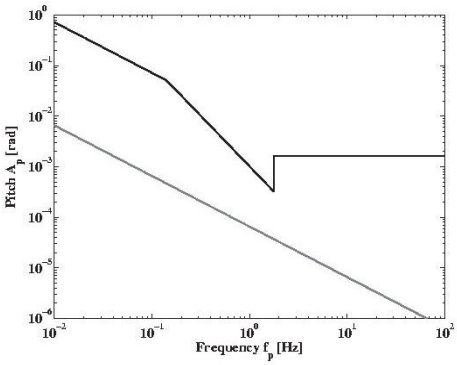

(b) The upper limit to the amplitude of sinusoidal pitch variations (black) and the error spectrum of the angle of the selected combination of motion sensors (gray).

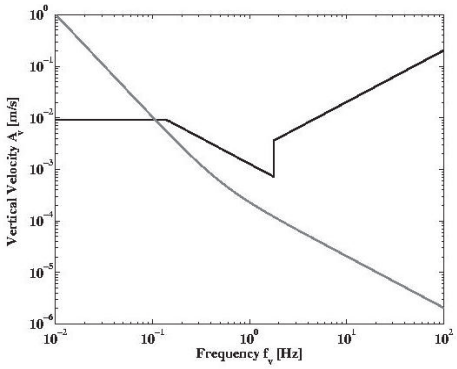

(c) The upper bound to the amplitude of a sinusoidal vertical velocity component (black) and the error spectrum of the velocity of the selected combination of motion sensors (gray).

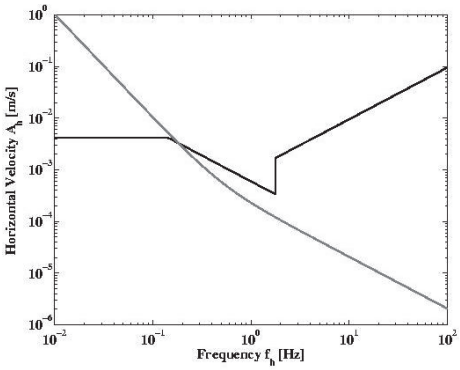

(d) The upper limit to the amplitude of a sinusoidal horizontal velocity component (black) and the error spectrum of the velocity of the selected combination of motion sensors (gray).

Figure 6.2: The upper limits to the amplitudes of sinusoidal angular motion and sinusoidal lateral velocity components (RMS values) and the error spectrums of the selected combination of motion sensors.

trums of the angle and the velocity assessed with the aid of this sensor combination are plotted in Fig. 6.2.
From Fig. 6.2(a) and Fig. 6.2(b) it can be seen that the error spectrum of the angle is always below the upper limits.
As can be seen from Fig. 6.2(c) and Fig. 6.2(d), the error spectrums for the lateral velocity components intersect the upper limits; for the vertical velocity component the intersection occurs around 0.1 Hz, whereas the intersection occurs about 0.2 Hz for the horizontal velocity component. This should not be a problem since the Garmin GPS35-HVS GPS receiver adequately measures motion of such low frequencies.
By taking this into account it was concluded that the selected combination of motion sensors lives up to requirements of the demonstrator system. Moreover, this combination was economical with respect to other combinations of motion sensors of comparable accuracy.

MiniSAR's Integrated Navigation System

The Stemme S10 is also the intended platform for the MiniSAR system. MiniSAR is a miniaturized SAR system currently being developed by TNO, [38]. The motion sensors applied in the MiniSAR integrated navigation system (INS) are more accurate than the motion sensors selected for the FM-CW demonstrator system. Moreover, the MiniSAR INS incorporates a magnetometer, [109]-[111]. Hence, it was decided to use the INS under development for MiniSAR for the FM-CW SAR demonstrator system as well. The MiniSAR INS incorporates three Honeywell QA-700 Q-Flex accelerometers, three Fizoptika VG941-3AM gyroscopes, a Wuntronic APS-536 Fluxgate magnetometer, and a Novatel Euro4 L1/L2 GPS board fitted with a Novatel 512-C antenna.

6.4 Overview of the Complete System

The block diagram and a picture of the complete FM-CW SAR demonstrator system are shown in Fig. 6.3 and Fig. 6.4 respectively. As can be seen, the core of the demonstrator system is a PXI chassis manufactured by National Instruments. The PXI chassis incorporates several advanced triggering and synchronization features. One of them is the 10 MHz system reference clock, which is available to all boards through the backplane of the chassis. The internal clocks of the different boards are all phase-locked to the system reference clock. The following boards are integrated in the PXI chassis:

The PXI-8176 1.26 GHz Pentium III controller and the PXI-8210 wide ultra SCSI interface, which transfers the measured data to the external 36.9 Gbyte hard drive;

The PXI-5411 11-bit, 4 MHz D/A board generates the waveform to control the output frequency of the VCO. At the beginning of each new period of the waveform, the D/A board generates a trigger signal. This trigger is routed to both A/D boards;

The PXI-6115 12-bit, 5 MHz A/D board samples the radar data. When it receives the first trigger from the D/A board it starts sampling the radar data continuously until the measurement is stopped. Synchronization with the D/A board is maintained since the internal clocks are all phase-locked to the system reference clock. The minimum input range of the PXI-6115

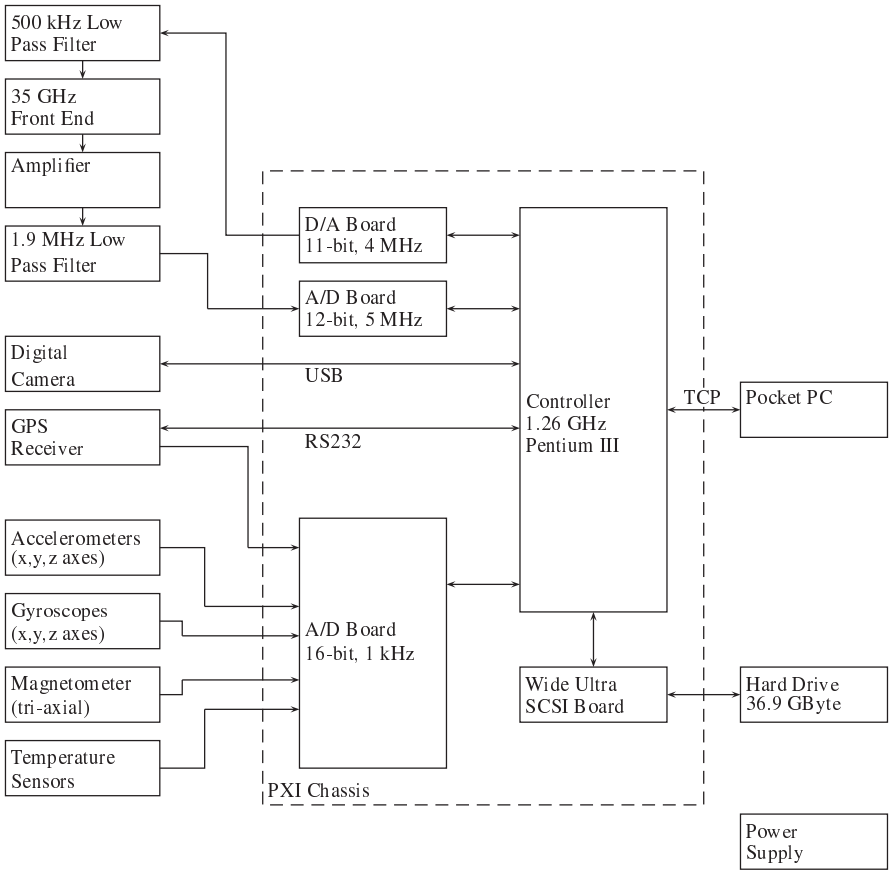

Figure 6.3: The block diagram of the complete FM-CW SAR demonstrator system.

is ± 200 mV. Thus the quantization interval follows as:

$$q = \frac{400}{2^{12}} = 0.0977\,\mathrm{mV}; \tag{6.8}$$

The PXI-6030E 16-bit, 1 kHz A/D board samples the sensor data. The board takes a sample of all input channels every time it receives a trigger from the D/A board; that is a single sample every *PRI*. Therefore, an estimate of the position and attitude of the platform can be obtained for each transmitted sweep.

The GPS receiver updates its position once per second through an RS232 serial connection. It is synchronized with the rest of the system by making use of the pulse train produced at the *Variable Frequency* output of the GPS board. This pulse train is sampled by the PXI-6030E A/D board as well. Once the GPS time of the first pulse is known, a GPS time stamp can be given to all samples. The GPS time of the first pulse is obtained by feeding the pulse train back to the GPS board through the *Mark Input*. The board logs the GPS times of the pulses

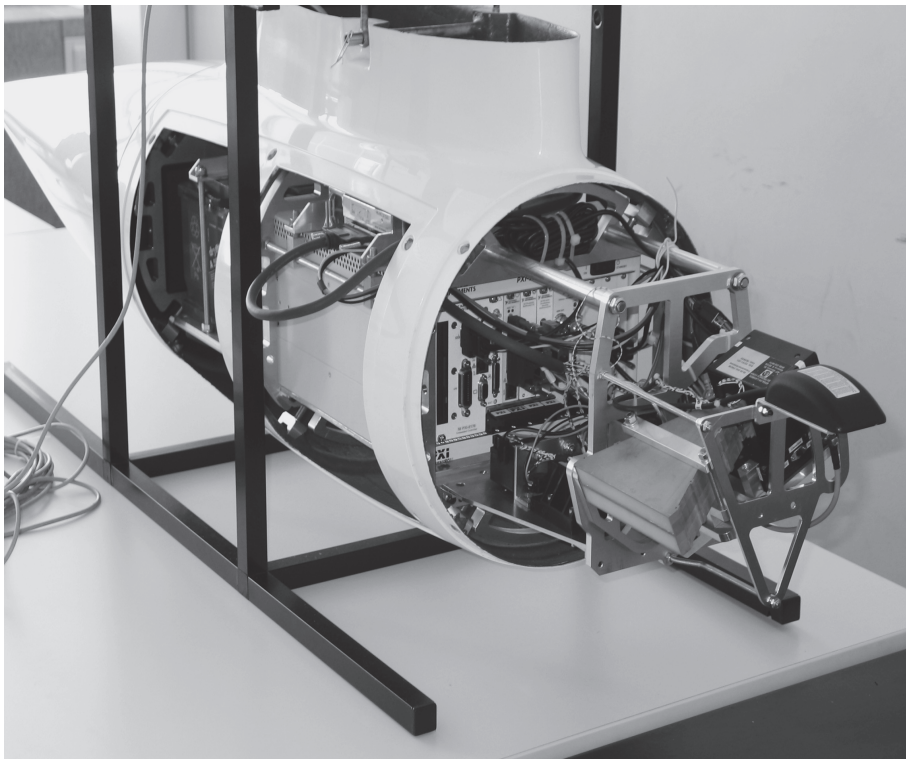

Figure 6.4: A picture of the FM-CW SAR demonstrator system in the pod. From back to front, the PXI chassis in the middle of the pod, the motion sensors in front of the PXI chassis, the FM-CW front end, and the GPS receiver can be seen.

received through the *Mark Input* and outputs them through the serial connection.
Initially, the digital camera was governed by the controller as is shown in the block diagram. However, the interaction with the camera turned out to be too demanding for the controller, resulting in buffer overflows of the A/D boards. In order to solve this problem, the camera is set to take pictures at regular time intervals independent of the rest of the system. To some extend synchronization is still possible by synchronizing the camera's time with the controller's system time.
During the flights, the demonstrator system can be controlled and monitored from the cockpit by means of a pocket PC. The demonstrator system is self-supporting; it is fed by a battery that is installed in the under wing pod as well. On a fully charged battery, the demonstrator system can run for approximately 2.5 hours. Further system details can be found in [104], [112]-[113].
A detailed overview of the receiver chain is given in Fig. 6.5. The range correlation factor was calculated at an offset frequency of 1.2 MHz, that is at the lower end of the beat spectrum. In

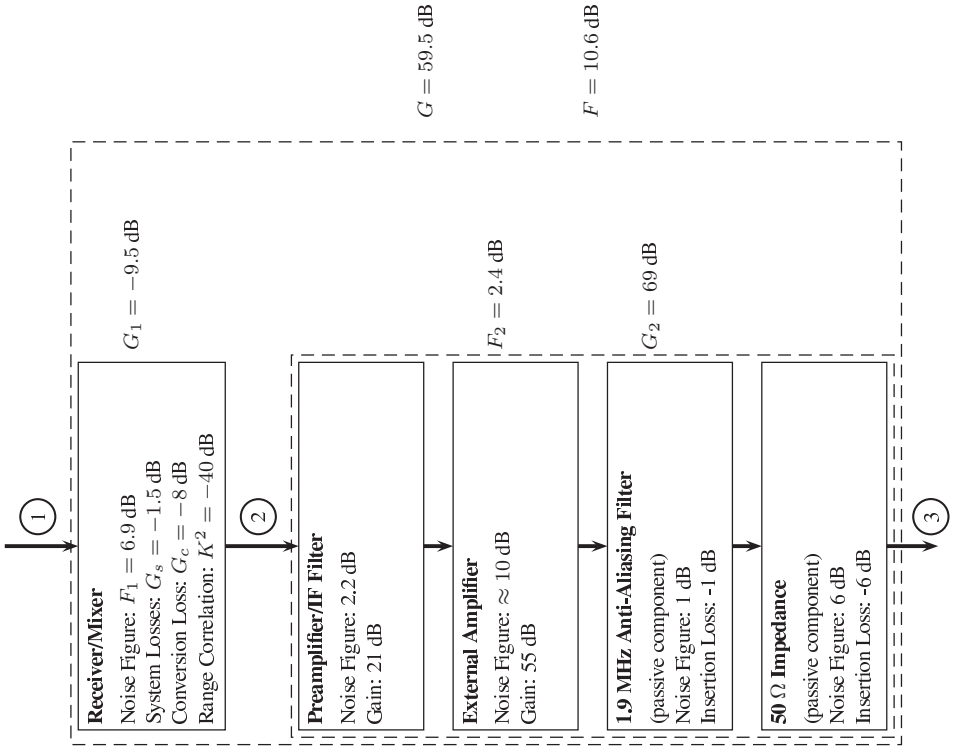

Figure 6.5: Schematic overview of the complete receiver chain.

the calculation it was assumed that the total propagation path of the direct coupling is 40 cm. Subsequently, in order to compute the phase noise power related to the direct coupling, the oscillator phase noise at an offset of 1.2 MHz should be estimated. By taking into account that the oscillator phase noise is -75 dBc/Hz at 100 kHz and by assuming a $1/f$ decay, -86 dBc/Hz is a reasonable estimate for the oscillator phase noise at 1.2 MHz.

Recapitulation: The initial requirements to the FM-CW SAR demonstrator system were reviewed, the choice of the motion sensors was argued, and the front end's design considerations were discussed. In order to speed up the development, it was decided to purchase an off-the-shelf front end that could be partially customized to our needs. A preliminary performance analysis was briefly reported. From the outcome of this analysis it was concluded that the sensitivity of the front end is not sufficient to produce high quality SAR images of areas which have a low RCS per unit area. Nevertheless, it should be feasible to give a proof of principle by making use of radar reflectors that have a large RCS. In the next chapter, a thorough performance analysis, taking the complete system set up into account, will be made.

Chapter 7

FM-CW SAR System Performance Analysis

Overview: In this chapter, a description of the ground-based and airborne measurements will be given. Moreover, the expected SNR will be calculated and compared to the actually measured SNR. The performance of the complete demonstrator system will be analyzed in order to explain the discrepancy between the expected and the measured SNR. Finally, the results of a system simulation will be presented in order to validate the conclusions drawn from the performance analysis.

7.1 Overview of the Ground-Based Test Trials

The first ground-based experiments with the complete system set up were carried out during the summer of 2003. Throughout these experiments, the demonstrator system was placed on the roof of the building of the Faculty of Electrical Engineering, Mathematics, and Computer Science at an altitude of approximately 90 m. A 40 dBm^2 corner reflector was set up at the ground at a slant-range of about 370 m. The angle of incidence was around 76°. A picture of the measurement area can be seen in Fig. 7.1.
Some results obtained during the ground-based measurements are presented in Fig. 7.2. These results were obtained after the coherent summing of 1024 echoes. Furthermore, the first 200 samples and the last 200 samples of each echo were discarded. The total number of samples in each echo is 5120, thus around 8% of the samples is discarded.
During these measurements, a nonlinearized sawtooth frequency modulation was applied, the PRF was 1 kHz, and the frequency sweep was 500 MHz. The response to the reflector can be clearly seen. The spreading in range due to the sweep nonlinearity is apparent. Moreover, what is noticeable about these results is that large harmonics are present at 310 m and 620 m, corresponding to range-frequencies of 1 MHz and 2 MHz respectively.

Frequency Sweep Nonlinearity

As already mentioned in section 6.2, it was expected that the sweep nonlinearity could be compensated by applying an adapted or *linearized* sweep control signal. If the nonlinear behavior of the VCO is measured, such a linearized control signal can be derived. The nonlinear behavior was measured by assessing the spectrogram of the response to the reflector, see Fig. 7.3(a) (the response is visible around 1.2 MHz). The spectrogram is assessed by di-

Figure 7.1: A picture of the measurement area in which the ground-based experiments were carried out. The reflector is indicated by the white circle.

viding the echo in small parts and subsequently calculating the beat frequency for each part. In this way, the beat frequency variation throughout the echo can be tracked.
The results of this assessment were used to calculate the deviation from the linear sweep and derive a linearized sweep control signal, [104]. In Fig. 7.3(b), the spectrogram of the response to the reflector is shown if the linearized sweep control signal is applied (the response is visible around 0.6 MHz). As can be seen, the beat frequency is now constant throughout the echo.
This type of linearization has an important disadvantage compared to the use of a dynamic linearization loop; variations of the nonlinear behavior, for instance due to temperature dependencies, cannot be taken into account. However, the nonlinear behavior of the VCO appeared to be fairly steady throughout the ground-based measurements.

Harmonics at 1 MHz and 2 MHz

The main reason for the harmonics being present is the quantized nature of the sweep control signal. Although the sweep control signal is low-pass filtered before it is being fed to

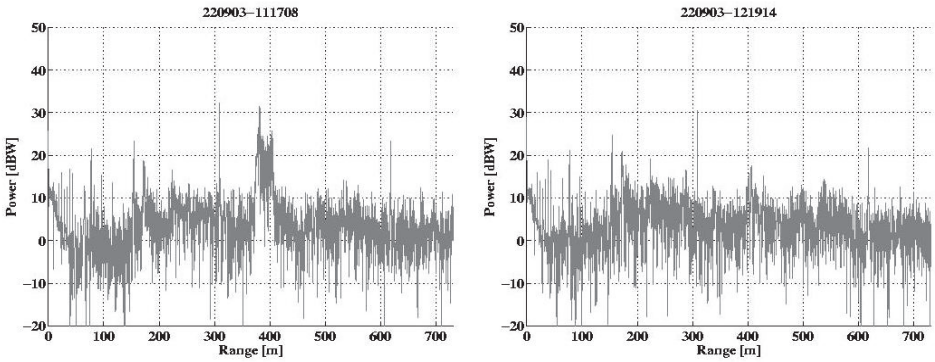

(a) The response to the reflector.

(b) The range spectrum of the same area when the reflector is removed.

Figure 7.2: Some results of the ground-based measurements.

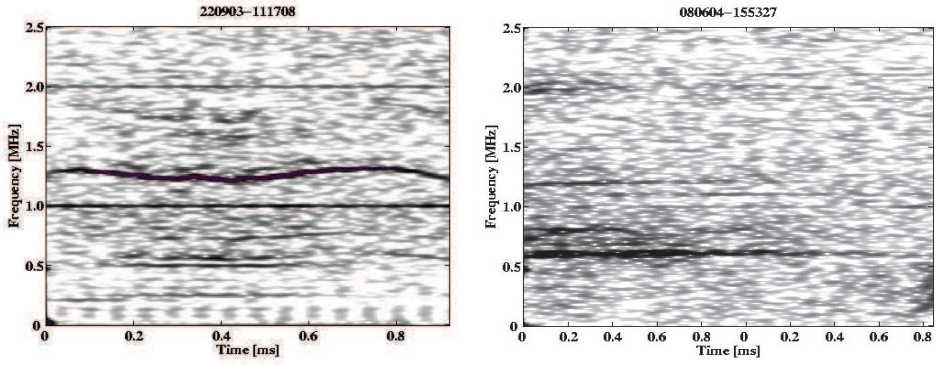

(a) An example of a spectrogram when non-linearized sawtooth modulation is applied.

(b) An example of a spectrogram when linearized sawtooth modulation is applied.

Figure 7.3: Some examples of spectrograms of the response to the reflector.

the VCO, residual amplitude steps may still remain. Another reason for the presence of the harmonics could be cross talk in the system. This idea is strengthened by the measurement of the noise spectrum of the PXI chassis, [104].
Since the harmonics are due to a combination of several effects, it is not likely that they can be easily eliminated. However, their influence should be small, since the harmonics are very narrow and their positions are known. Therefore, it was decided to undertake no further action to eliminate these two harmonics.

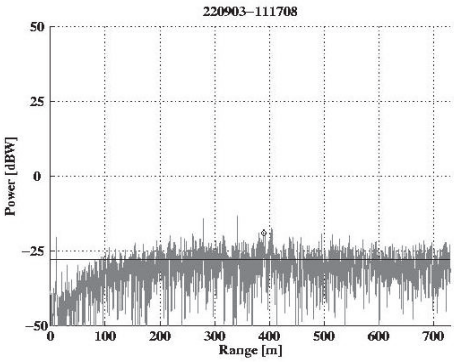

(a) The response when a single echo is processed.

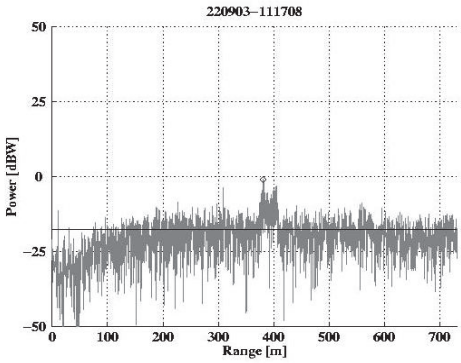

(b) The response when 10 echoes are processed.

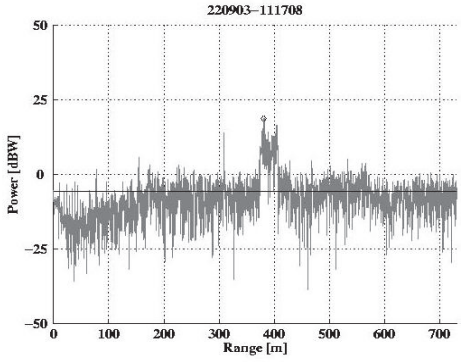

(c) The response when 100 echoes are processed.

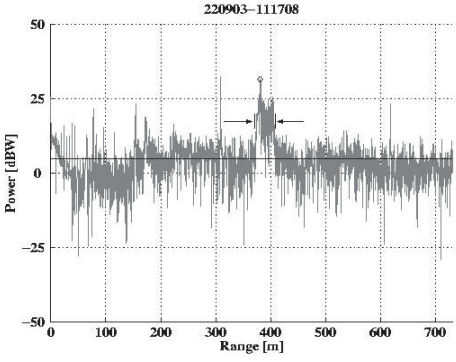

(d) The response when 1024 echoes are processed.

Figure 7.4: The response to the 40 dBm^2 reflector for different values of n_e. The signal peak power and the average noise level are indicated by the diamond and the solid line respectively.

MiniSAR INS and Radome

During the airborne measurements, the front end is covered by a radome. The effect of the radome was investigated during the ground-based measurements. If the radome is in place, the range spectrum becomes noisier, but the increase of the average noise level is small; of the order of 1 dB.
Moreover, the MiniSAR INS is incorporated in the FM-CW SAR demonstrator system throughout the airborne campaign. The power supply of the MiniSAR INS is based on dc-dc couplers, the operation of which could lead to contamination of the measurements. The influence of the power supply was also investigated during the ground-based measurements. If the power supply is switched on the range spectrum becomes noisier, but again the increase of the average noise level is small; around 1 dB.

7.2 Signal-to-Noise Ratio Evaluation

Expected and Measured Signal-to-Noise Ratio

The expected SNR was calculated by making use of the expressions derived in chapter 5 and the system parameters mentioned in chapter 6. In this calculation, the complete system set up and the geometry of the ground-based measurements were taken into account. The expected values of the total available noise power and of the signal peak power are summarized in table 7.1.
The measured average noise level and signal peak power are indicated in Fig. 7.4 for different values of n_e, the actual values are listed in table 7.1. The measured SNR is about 62 dB lower than the expected SNR for the case that n_e is 1024.
The discrepancy between the expected and the measured SNR is partially caused by the measured noise level being around 4 dB higher than expected. A possible reason for the high measured noise level could be the sidebands related to relatively strong echoes from objects near by, for instance the fence around the roof or the roof itself.
However, the discrepancy is mainly due to the large difference between the expected and measured signal peak power. The measured peak power is around 56 dB lower than expected. There are several effects that could cause the peak power being lower than expected. In the following subsections, these effects will be discussed and, if possible, quantified.

Transmitted Power

One reason for the low signal power could be the transmitted power being lower than specified. Therefore, the transmitted power was examined by using a separate receive antenna and a spectrum analyzer and power meter. These measurements were carried out in CW mode and the signal power was measured directly at 35 GHz. This method has the significant shortcoming that all received power ends up at 35 GHz in the range spectrum. Hence, it is not possible to make a distinction between the power received directly from the transmitter and the power backscattered by the objects present in the measurement area.
These measurements were carried out on the roof of the Faculty building in order to have a clear measurement area. Nevertheless, a small brick wall and some metal fences were present around the area. During the measurements it turned out that multipath effects had an important influence on the measured results. The results were therefore considered untrustworthy.

Table 7.1: The signal peak power, the average noise level, and the SNR for different values of n_e. The expected values (E) as well as the measured values (M) are given.

n_e	Signal Peak Power [dBW]		Average Noise Level [dBW]		SNR [dB]	
	E	M	E	M	E	M
1	27.1	-19.0	-30.0	-28.0	58.1	9.0
10		-1.0		-17.7		16.7
100		18.7		-5.6		24.3
1024	87.3	31.5	0.4	4.9	88.1	26.6

Table 7.2: The signal peak power, the average noise level, and the SNR for different values of n_e. In this table, the values are normalized to the values obtained when n_e is equal to one. The theoretical values are given between brackets.

n_e	Signal Peak Power [dB]	Average Noise Level [dB]	SNR [dB]
1	0	0	0
10	18 (20)	10.3 (10)	7.7 (10)
100	38 (40)	22.4 (20)	15.3 (20)
1024	51 (60)	33.0 (30)	17.6 (30)

However, the outcome of similar laboratory measurements made at very short range hinted at the transmitted power being close to the system specifications or less than 1 dB lower. Therefore, it is assumed that the front end lives up to the specifications regarding the transmitted power.

Oscillator Stability

The behavior of the oscillator's output signal was monitored in CW mode. From this measurement it became clear that the carrier frequency varies approximately 200 MHz over time periods of the order of the SAR observation time. Moreover, sudden jumps of the carrier frequency were observed occasionally.

Unwanted (random) variations of the phase of the oscillator's output signal during the transmission of a sweep and the reception of the corresponding echo result in an erroneous demodulation of the echo signal. As a consequence, the phase of the beat signal is distorted and the beat frequency varies throughout the echo. The sweep nonlinearity is an example of such unwanted phase variations.

In the calculation of the expected signal peak power it was assumed that all the energy of the response is mapped onto a single FFT bin. However, when the beat frequency is not constant throughout the echo, the energy of the response is spread over several FFT bins. This spreading or *spectral leakage* results in a decrease of the signal peak power.

The loss of signal peak power due to spectral leakage can be quantified by integrating the energy over the complete response. In order to obtain the energy contained in the complete response, the range spectrum was integrated over the interval indicated by the arrows in Fig. 7.4(d). The signal power contained in the complete response is 41.6 dBW. Therefore, it can be concluded that 10 dB of signal peak power is lost because of spectral leakage.

As already explained, due to the erroneous demodulation, the phase of the beat signal is distorted. Therefore, the typical azimuth phase history that SAR processing relies on is distorted and as a consequence the SAR processing gain is less than n_e^2. Although the phase distortions are assumed to be small, they may have a considerable effect if the SAR observation time increases.
This is confirmed by table 7.2. In this table, the measured signal power, average noise level, and SNR are listed for different values of n_e, but now they are normalized to the values measured in the case that n_e is one. The theoretical values are given between brackets.
The increase of the signal power follows the theory very well for small values of n_e (reflecting relatively short SAR observations times). However, in the case that n_e is 1024, the SAR processing gain lags behind the theoretical value. This verifies the idea that the echo to echo coherency is lost over longer periods of time. Around 10 dB of SAR processing gain is lost in the case that n_e is 1024.
Furthermore, from table 7.2 it can be seen that the increase of the noise level is higher than theoretically anticipated. This strengthens the idea that the noise floor is increased by the (partially coherent) sidebands related to echoes coming from objects near by.

Note that, just like the effect of the sweep nonlinearity, the effect of relatively slow random phase variations should be range dependent. This idea was confirmed by the results of further ground-based measurements. At the test grounds of the Institute of Wind Energy some short-range measurements were carried out; the reflector was placed at a range of about 70 m. The normalized values of the measured signal peak power, the average noise level, and the SNR are summarized in table 7.3. As can be seen, at such a short range the SAR processing gain indeed follows the theoretical value even for large values of n_e[†].

System Specifications and Measurement Geometry

The front end is well specified within the work band of 1 to 2.5 MHz. Nevertheless, the magnitude of some system characteristics, such as the oscillator phase noise and the range correlation factor, had to be estimated.
Furthermore, some uncertainties in the measurement geometry exist. For example, the range to the reflector could not be accurately measured and there were no means to precisely align the reflector and the antenna main beam.
The difference between the expected and measured signal peak power could be partly due to these uncertainties. However, the difference due to these uncertainties is assumed to be small; may be of the order of 5 dB.

[†]This can be understood by considering the background of the front end; the front end is a customized version of a car collision-avoidance radar with a maximum measurement range of 150 m.

Table 7.3: The measured signal peak power, the noise level, and the SNR for different values of n_e. In this table, the values are normalized to the values obtained when n_e is equal to one. The theoretical values are given between brackets (Measurements at the Institute of Wind Energy).

n_e	Signal Peak Power [dB]	Average Noise Level [dB]	SNR [dB]
1	0	0	0
10	19.6 (20)	8.5 (10)	11.1 (10)
100	38.9 (40)	20.5 (20)	18.4 (20)
1024	58.8 (60)	27.9 (30)	30.9 (30)

Accuracy Reflector

The 40 dBm^2 corner reflector used during the ground-based measurements was originally manufactured for 10 GHz applications, thus it may not be accurate enough for usage at 35 GHz. Therefore, it was necessary to calibrate the 40 dBm^2 reflector. The reflector was calibrated by using the front end as a transmitter and a separate receive antenna and spectrum analyzer. The receive antenna was set up some distance from the front end in order to minimize the direct coupling. The results of these measurements gave an inkling of the actual RCS of the reflector being about 5 dB lower than the theoretical RCS.
However, these measurements should be interpreted with care; mutual coupling between the reflector and its surroundings may have affected the RCS measurements, [114]. Moreover, these measurements were carried out in CW mode, hence it was not possible to distinguish the power backscattered by the reflector from the power backscattered by other objects in the measurement area.
In addition, the 40 dBm^2 reflector has 64 cm ribbons. Thus the reflector is larger than a range resolution cell, resulting in spectral leakage.

Conclusion

As explained, the measured SNR is about 62 dB lower than the expected SNR. The main reason for this discrepancy is the measured signal peak power being 56 dB lower than expected. Several reasons for the low measured signal power were discussed and quantified. It was argued that the following losses and reservations should be taken into account: a 10 dB loss caused by spectral leakage, a 10 dB loss due to loss of coherency, a 5 dB difference because of system uncertainties, and finally a 5 dB loss due to reflector inaccuracies, but that still leaves another 26 dB unaccounted for.
The 26 dB gap may be partly caused by the cautious estimation of the losses. In order to really pinpoint the cause, accurate and detailed measurements of the echo signal are required. At this point, such measurements are practically impossible because of the following reasons:

- Necessary measurement equipment applicable at 35 GHz, such as a delay line, a transponder, or a calibrated reflector, is not available;
- The surroundings affect the measurements, even on the roof of the Faculty building. The IRCTR anechoic chamber could not be used for the calibration measurements, since it is

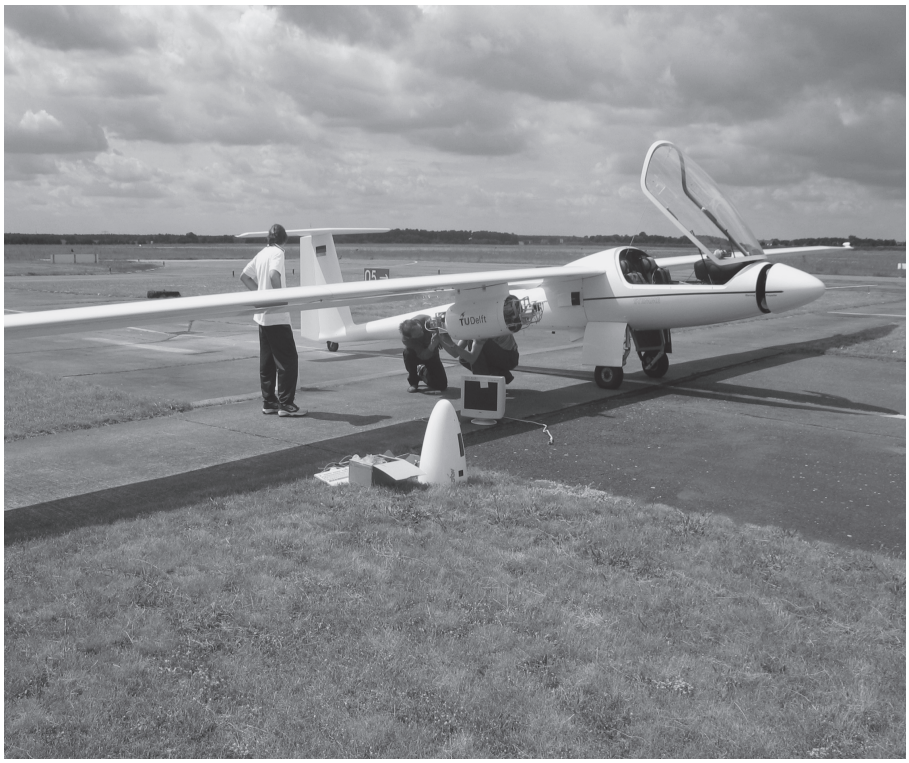

Figure 7.5: An impression of the airborne campaign.

only 6 m long (that far outside the work band the front end is not specified);

- The front end is a black box; just the beat signal can be measured. It is not possible to measure the outputs of the various subcomponents. Moreover, no specifications are given for the subcomponents;

- The transmitter and the receiver can not be switched on and off separately;

- The spectrum analyzer cannot store the measured data and moreover it does not preserve the phase of the measured signal.

Without a considerable investment in time and equipment, a full characterization of the front end cannot be made. However, the manufacturing of a reflector calibrated at 35 GHz may be worthwhile. A calibrated reflector is the least that is needed to allow more accurate calibration measurements.

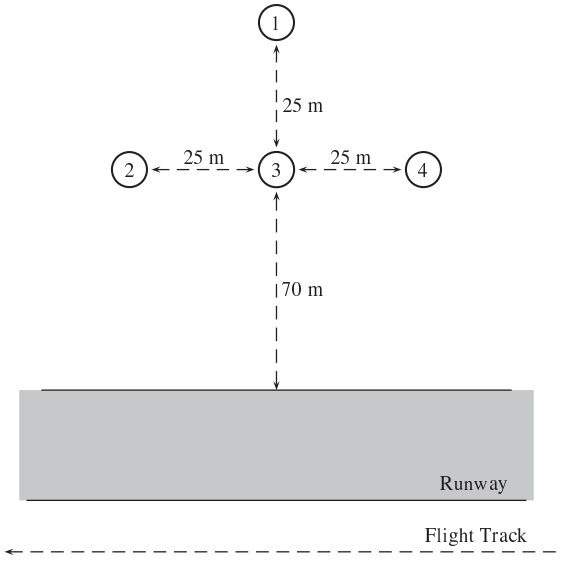

Figure 7.6: Top view of the geometry of the reflectors (numbered 1 to 4). The GPS ground station was set up next to reflector number 3.

7.3 Overview of the Airborne Measurements

The airborne campaign was carried out at the Strausberg airfield just East of Berlin on June 22nd and 23rd 2004, an impression is given in Fig. 7.5. Next to the runway four corner reflectors were placed and their GPS coordinates were measured, see Fig. 7.6. Two small 33 dBm^2 reflectors (1 and 2) and two large 40 dBm^2 reflectors (3 and 4) were set up. Moreover, a GPS ground station was installed in the middle of the scene (at position 3). An airborne picture of the measurement area can be seen in Fig. 7.7.
Several runs were flown parallel to the runway along the reflectors at 100 m, 150 m, and 300 m altitude. In addition, some flights were made at 200 m and 300 m altitude, during which the engine of the glider was switched off. On the second day of the campaign the angle of incidence was decreased from 65° to 55°. Finally, an experiment was performed to investigate the influence of the engine vibrations.
The weather was quite turbulent. Some heavy rain showers passed the airfield during which the glider could not take off. The wind was directed practically perpendicular to the runway. Hence, a squint angle due to aircraft yaw was present during the measurements.
Throughout the campaign, the demonstrator system performed to satisfaction and practicable radar data as well as motion data were recorded.

Evaluation of the First Airborne FM-CW SAR Image

The first airborne FM-CW SAR image is presented in Fig. 7.8. This image is generated with data acquired during a flight made at 100 m altitude. The angle of incidence was 65°, the

Figure 7.7: An airborne picture of the measurement area. The position of the reflectors is indicated by the white triangle. Note the shadow of the glider in the foreground.

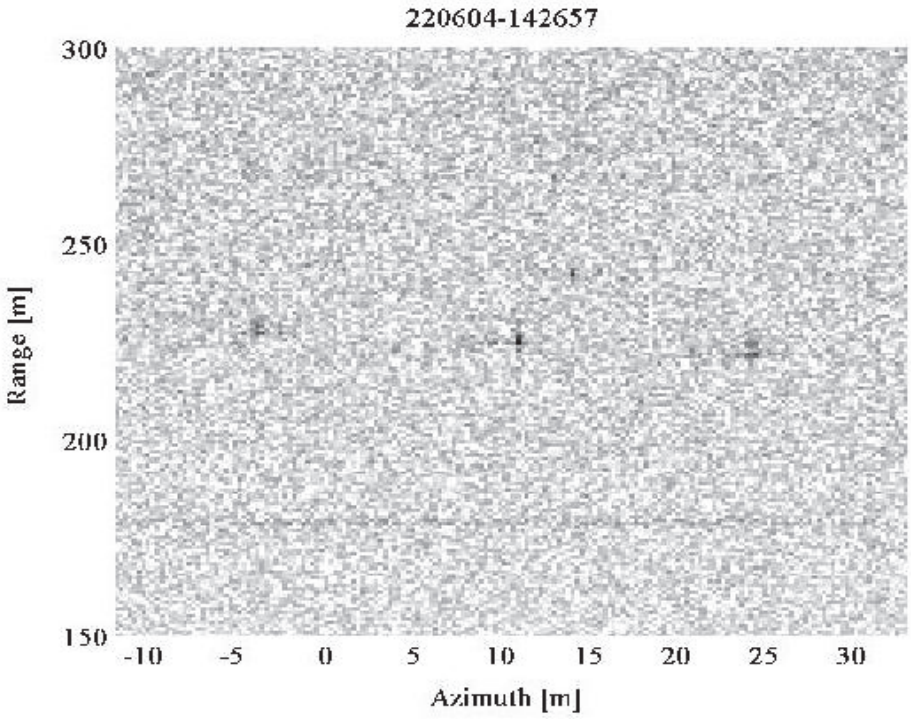

Figure 7.8: First airborne FM-CW SAR image.

slant-range to the middle of the scene was around 240 m, and the velocity of the glider was around 30 m/s. During this run, linearized sawtooth frequency modulation was applied, the *PRF* was 1 kHz, and the frequency sweep was 190 MHz. The SAR image was obtained by using the FM-CW SAR processor developed within the framework of the project. In order to enhance the image contrast, 16 azimuth resolution cells are incoherently summed.
The responses to the four reflectors are observable. The geometry corresponds very well to the actual geometry, which is shown in Fig. 7.6. The attributes of the responses are summarized in table 7.4. It should be noted that the attributes were determined before the summing of azimuth cells and that the resolutions were determined at the -3 dB points of the responses. As can be seen, the performance of the demonstrator system in terms of resolution is good.
In order to evaluate the SNR of the FM-CW SAR image, the expected SNR was calculated following the approach described in chapter 5. The expected values of the available noise power, the signal peak power, and the SNR are listed in table 7.4 as well. The expected and measured SNR will be compared by using the attributes of reflector 3 as a reference.
The measured noise level is around 7 dB higher than expected. This is probably due to the combined effect of the engine vibrations, the radome, and the MiniSAR INS. In the next subsection it is shown that the increase of the average noise level due to the engine vibrations is around 1 dB. Therefore, the combined effect of the engine vibrations, the radome, and the

Table 7.4: The signal peak power, the average noise level, the SNR, and the resolution of the airborne FM-CW SAR image.

	Expected Values	**Reflectors**			
		# 1	# 2	# 3	# 4
Range [m]:	240	242	227	225	222
Range Resolution [m]:	0.79	1.03	0.71	1.01	0.73
Azimuth Position [m]:		14	-4	11	24
Azimuth Resolution [m]:	0.05	0.08	0.07	0.06	0.11
RCS [dBm^2]:	40	33	33	40	40
Signal Peak Power [dBW]:	98.8	35.4	34.6	41.6	37.6
Average Noise Level [dBW]:	13.1	19.9	19.9	19.9	19.9
SNR [dB]:	85.7	15.5	14.7	21.7	17.7

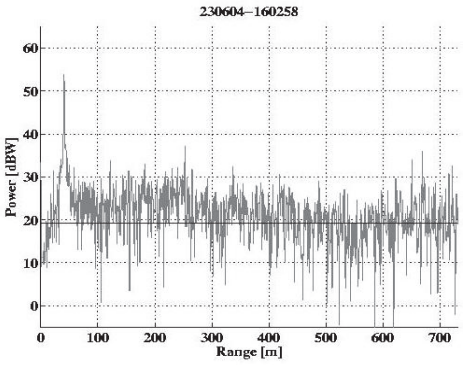

(a) The reference measurement; the engine was switched off during this measurement.

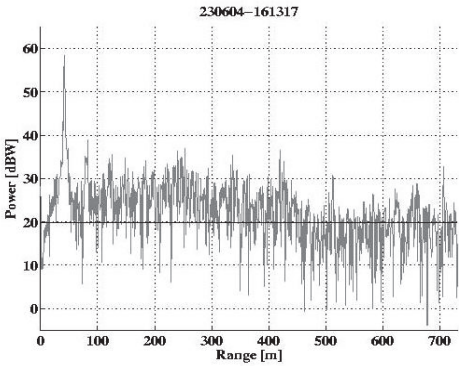

(b) The response to the reflector while the engine was running at 2100 rpm.

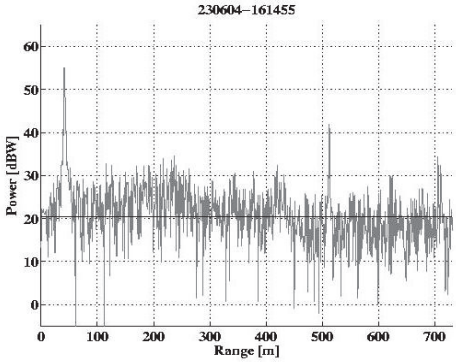

(c) The response to the reflector while the engine was running at 2300 rpm.

Figure 7.9: The effect of engine vibrations on the range spectrum.

MiniSAR INS is an increase of the average noise level of 3 to 4 dB.
The signal peak power is 57 dB lower than expected. By going along the reasoning in section 7.2, the following losses should be taken into account: at least 6 dB caused by spectral leakage (mainly in azimuth direction), a 10 dB loss due to a loss of coherency, a 5 dB difference due to system uncertainties, and finally a 5 dB loss because of reflector inaccuracies. That leaves around 30 dB unaccounted for. Thus the performance seems to deteriorate slightly when the system is onboard the glider.

Effect of Engine Vibrations

In order to investigate the possible effect of engine vibrations, some measurements were carried out on the ground. During these measurements, the glider was stationary and the 40 dBm^2 reflector was set up at a range of 40 m. A reference measurement of the response to the reflector was made while the engine was switched off. The measurement was repeated while the engine was running at 2100 revolutions per minute (rpm) and 2300 rpm. The measured range spectrums are presented in Fig. 7.9.
By comparing Fig. 7.9(a) through Fig. 7.9(c) it can be seen that the response becomes noisier if the engine is switched on. However, the increase of the average noise level is only 0.5 to 1 dB. Furthermore, around 500 m and 700 m harmonics appear. These harmonics are however outside the measurement range.

7.4 Demonstrator System Simulation

In order to further investigate the performance of the FM-CW SAR demonstrator system, a detailed system simulation was developed. The characteristics of all components making up the receiver chain (see Fig. 6.5) were taken into account in the simulation. However, some components are only roughly specified, especially the filter characteristics of some components. The system characteristics applied in the simulation may therefore differ to some extend from the actual system characteristics.
The simulation was adapted to reflect the ground-based and airborne measurement geometries. In the next subsections, the results of the simulation will be presented.

Simulation Ground-Based Measurements

In the simulation of the ground-based measurements, the system settings and the measurement geometry, as described in section 7.1, were taken into account. Furthermore, in the simulation, a sinusoidal sweep nonlinearity of frequency $f_m = 1.5PRF$ and amplitude $\Delta f_e = 12.5$ MHz was introduced. These parameters were chosen in such a way that the simulated nonlinearity matches the actual sweep nonlinearity as shown in Fig. 7.3(a).

The simulated range spectrum in the case that n_e is one is presented in Fig. 7.10(b), the actual measurement is shown in Fig. 7.10(a). By comparing the results it can be seen that the overall shape and the average noise level agree very well. However, in the simulated range spectrum the response to the reflector is clearly visible, whereas in the measured range spectrum, the response is barely noticeable. This strengthens the idea that somehow signal power is lost in the demonstrator system.
The signal peak power of the simulated response is 14 dBW, that is 13 dB lower than the

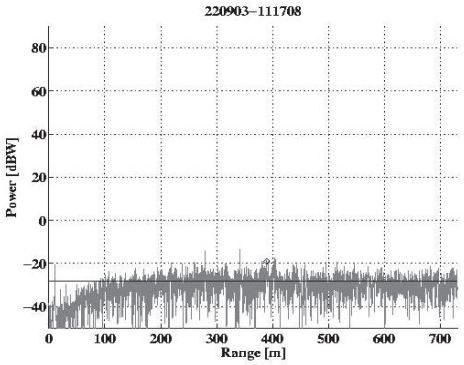

(a) The measured range spectrum when n_e is equal to one.

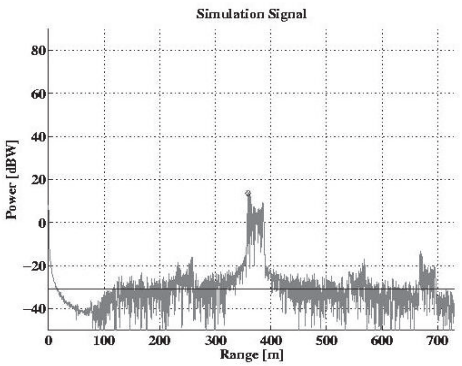

(b) The simulated range spectrum when n_e is equal to one.

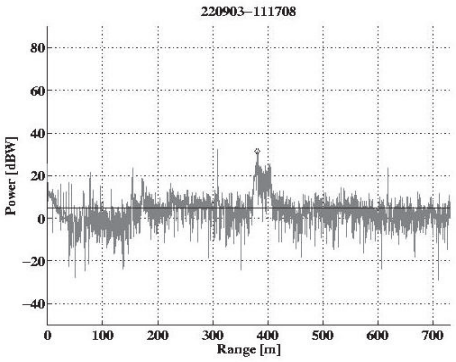

(c) The measured range spectrum when n_e is equal to 1024.

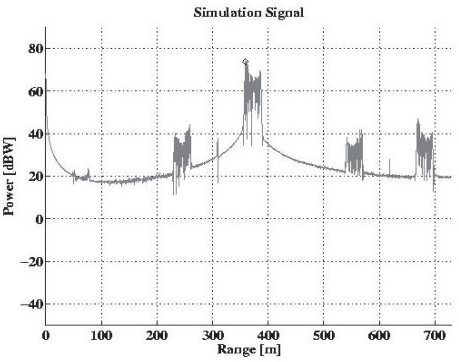

(d) The simulated range spectrum when n_e is equal to 1024.

Figure 7.10: A comparison between the actually measured (left) and the simulated (right) range spectrums.

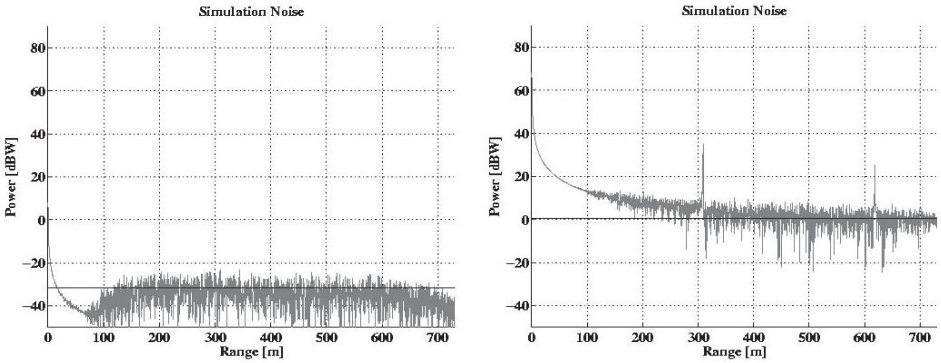

(a) The simulated noise spectrum in the case that n_e is equal to one.

(b) The simulated noise spectrum in the case that n_e is equal to 1024.

Figure 7.11: The results of the simulation of the noise spectrum. The average noise level is indicated by the solid line.

expected value listed in table 7.1. This discrepancy can be explained by the 10 dB loss due to spectral leakage and the small differences between the simulated and the actual system characteristics.
Another difference is the fact that the direct coupling is more pronounced in the simulated range spectrum. This is caused by differences between the filter characteristics; in the actual IF filter, the attenuation at very low frequencies is much higher than in the simulated IF filter.

The simulated range spectrum in the case that n_e is 1024 is shown in Fig. 7.10(d). Now some apparent dissimilarities exist between the simulated and the measured range spectrums.
The harmonics at 310 m and 620 m are less pronounced in the simulated range spectrum, since the average level is very high. What is more, spurious responses are present around the harmonics (the spurious responses are also slightly observable in Fig. 7.10(b)). In the simulation, the spurious responses are solely due to the quantized nature of the frequency sweep. If a continuous sweep is applied, the spurious responses, as well as the harmonics, completely disappear.
The peaks of the simulated and measured responses are located at slightly different ranges. This is due to differences between the simulated and the actual sweep nonlinearities. The signal peak power of the simulated response is 74 dBW, that is again 13 dB lower than the expected value.
The average level of the simulated range spectrum is very high. This is due to the coherent sidebands of the response and the spurious responses. In order to investigate the actual noise level, the noise spectrums were therefore simulated.
The simulated noise spectrums are presented in Fig. 7.11. The average noise levels are -31.7 dBW and 0.6 dBW for the cases that n_e is one and n_e is 1024 respectively, which

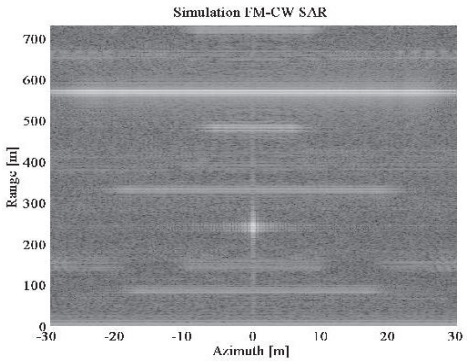

Figure 7.12: The simulated FM-CW SAR image.

corresponds well to the expected values. Note that in the noise spectrum the harmonics are evident.

Simulation Ground-Based Measurements Conclusion

In the simulation, the harmonics at 310 m and 620 m are solely due to the quantized nature of the frequency sweep. In the actual system, they are most likely due to a combination of several effects. Nevertheless, the part of the system generating the sweep control signal (the D/A board and the low-pass filter) should be designed with care. For instance, it may be possible to shift the harmonics to higher frequencies, outside the frequency band of interest, if the update rate can be chosen sufficiently high.

Furthermore, the simulation proved that it is important to filter out the direct-coupled signal carefully, even though its main spectral component is far outside the frequency band of interest. Since it is a relatively strong signal, the direct coupling may saturate the A/D board or other components if it is not filtered out properly.

Simulation Airborne Measurements

In the simulation of the airborne measurements, the system settings and the measurement geometry as reviewed in section 7.3 were taken into account[‡]. A sinusoidal sweep nonlinearity of frequency $f_m = 1.5PRF$ and amplitude $\Delta f_e = 85$ kHz was introduced. This small sweep nonlinearity reflects the residual nonlinearity if the linearized modulation is applied.

The simulated FM-CW SAR image is shown in Fig. 7.12. The response to the reflector is visible in the middle of the scene at a range of about 240 m. In addition, several spurious responses are present. In the simulation, the spurious responses are again solely due the quantized nature of the frequency sweep.

The range and azimuth cross sections of the simulated FM-CW SAR response are presented in Fig. 7.13, the cross sections of the actual measurement are shown as well. As can be seen, the simulated range response exhibits several maximums. This is due to interference with the

[‡]Note that in the simulation, the input range of the A/D board had to be increased in order to accommodate the strong echoes.

spurious responses; if a continuous sweep is applied, the range response exhibits just a single maximum. What is more, due to the sidebands of the spurious responses, the overall level is higher than in the actual measurement.
The signal peak power in the simulation is 68 dBW, that is around 30 dB lower than the expected value, see table 7.4. The discrepancy is partly due to the interference with the spurious responses; if a continuous sweep is applied, the peak power is 82 dBW. Furthermore, signal peak power is lost due to spectral leakage in azimuth as well as range direction.

Recapitulation: An overview of the ground-based and airborne measurements was given. Furthermore, a thorough performance analysis was made. From this analysis it was concluded that the measured signal peak power is significantly lower than the expected signal power. Some possible causes, such as oscillator instabilities, were discussed. However, the discrepancy could not be explained completely. During the airborne campaign, the performance of the demonstrator system was good in terms of resolution, in terms of SNR the performance again lagged behind the expectations.
The system simulation showed that a careful design of the generation of the sweep control signal is critical in order to prevent harmonics and spurious responses.

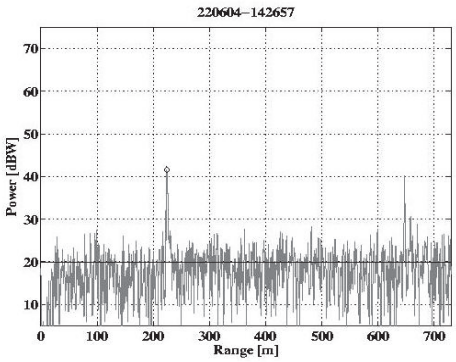

(a) The cross section in range direction of the measured response.

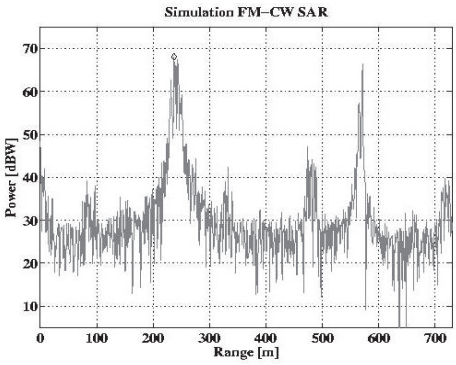

(b) The cross section in range direction of the simulated response.

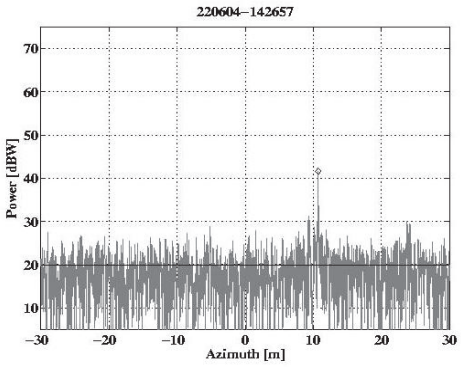

(c) The cross section in azimuth direction of the measured response.

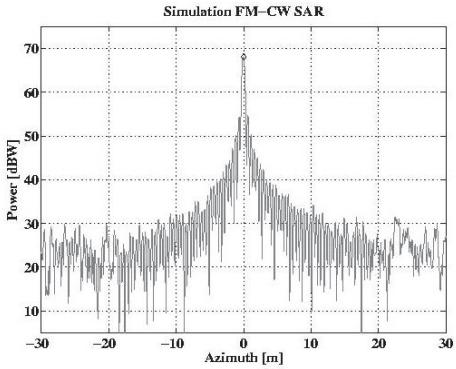

(d) The cross section response in azimuth direction of the simulated response.

Figure 7.13: Range and azimuth cross sections of the measured and simulated FM-CW SAR responses.

Chapter 8

Conclusion and Recommendations

The main objective of this study was to prove the feasibility of FM-CW SAR under operational circumstances. The practicability of FM-CW SAR was proven by the development of a fully operational airborne demonstrator system. Moreover, the successful airborne campaign proved that an FM-CW SAR system can indeed be operated in an efficient and cost effective manner from a small aircraft.
The platform motion during the transmission of a sweep and the reception of the corresponding echo was expected to be one of the major problems. However, the Doppler frequency shift induced by the platform motion could be effectively compensated by applying a modified range migration compensation algorithm. In the end, the main problems encountered in the course of the development were the 'conventional' problems of FM-CW radar systems: the direct coupling, the frequency sweep linearization, and the synchronization.
Although its main spectral component is far outside the frequency band of interest, it is important to filter out the direct coupling properly. Otherwise it may saturate the A/D board or other components, since it is a relatively strong signal. Moreover, the sweep control signal generation should be designed carefully in order to prevent harmonics in the frequency band of interest.
As a whole, the FM-CW SAR demonstrator system performed most satisfactory. The use of the PXI chassis and the software-programmable A/D and D/A boards offered a very flexible solution. As a result, the MiniSAR INS could be easily integrated in the existing demonstrator system. Merely the 35 GHz front end did not live up to the expectations in terms of the SNR.
The signal power is much lower than theoretically calculated. This is partly due to spectral leakage and loss of coherency over periods of the order of the SAR observation time. However, the discrepancy could not be completely explained. Meaningful measurements were made difficult by the fact that the front end is a black box; the subcomponents are only roughly specified and their outputs cannot be measured. The calibration measurements were further complicated by the fact that the required measurement equipment applicable at 35 GHz was not available. The least that is required in order to enable more reliable calibration measurements is a calibrated reflector.

Recommendations

As mentioned, the demonstrator system performed to satisfaction; just the front end did not meet the expectations. Therefore, in order to improve the performance of the demonstrator system, the front end should be replaced.

Currently, other off-the-shelf front ends are available, [115]. (Note that the antennas of the Epsilon-Lambda front end can be reused.) However, looking back, the in-house development of the RF subsystem has the significant advantage that it offers complete control over the system design.

A new design could be based on a VCO again; VCOs with superior phase noise characteristics are available, [68]. However, with respect to phase noise and frequency sweep linearity, the use of a direct digital synthesizer (DDS) is preferable, [116]. A Ka-band FM-CW radar based on a DDS has already been reported, [117].

Related Work

That FM-CW SAR is indeed a promising concept is further illustrated by the fact that other groups have started working on the subject as well, [118]. Moreover, the results obtained with the operational MISAR system, [119]-[120], prove the usefulness of an airborne FM-CW SAR system when indeed a dedicated RF design is made.

At the IRCTR the work on the subject continues with the development of more sophisticated FM-CW SAR processing algorithms, including MTI algorithms, [121]. Furthermore, preparations have been made for the development of a miniaturized P-band FM-CW SAR based on a DDS, [122]-[123].

Appendix A

Limits to Uncompensated Motion Errors

In this appendix, the derivations of the upper limits to uncompensated motion errors will be given. The derivations were taken from [92].
In order to investigate the effect of different velocity components, the actual platform velocity is decomposed in an along-track component v_{at} and a cross-track component v_{ct}, see Fig. A.1. The cross-track velocity component is directed normal to the ideal flight track in the slant-range plane. The $\mathrm{d}v_{at}$ component denotes the along-track velocity error.

Along-Track Velocity Error

The deviation in range due to a deviation in along-track velocity can be found by differentiating range with respect to the along-track velocity. However, the quality of the final SAR image depends on phase deviations rather than range deviations. Therefore, the phase of the echo signal should be differentiated with respect to along-track velocity. With the aid of (2.11) and (2.13), the derivative of the phase of the echo signal with respect to along-track velocity can be derived:

$$\frac{\mathrm{d}\varphi}{\mathrm{d}v_{at}} = \frac{4\pi}{\lambda}\frac{\mathrm{d}R}{\mathrm{d}v_{at}} = \frac{4\pi}{\lambda}\frac{t^2 v_{at}}{R_0}. \tag{A.1}$$

As can be seen, an along-track velocity error leads to a phase error that is proportional to the time squared. The maximum of the quadratic phase error occurs in the middle of the SAR observation time, that is:

$$\delta Az_{sar} = \frac{\lambda R_0}{2L_{sar}} = \frac{\lambda R_0}{2vT_{sar}} \Longrightarrow \frac{T_{sar}}{2} = \frac{\lambda R_0}{4v_{at}}\delta Az_{sar}. \tag{A.2}$$

Then, by substituting (A.2) in (A.1), it follows that:

$$\mathrm{d}v_{at} = \frac{4v_{at}\delta Az_{sar}^2}{\pi\lambda R_0}\mathrm{d}\varphi. \tag{A.3}$$

Finally, when a maximum phase deviation of $\pi/4$ is allowed, (A.3) can be rewritten as:

$$\mathrm{d}v_{at} \leq \frac{v_{at}}{\lambda R_0}\delta Az_{sar}^2. \tag{A.4}$$

Cross-Track Velocity Error

A cross-track velocity error causes a shift of the illuminated area in azimuth direction, as is

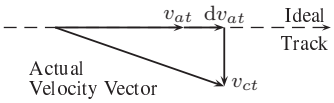

Figure A.1: The arrangement of the velocity components in the slant-range plane.

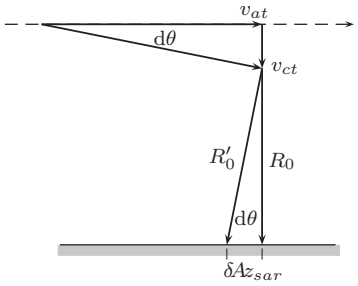

Figure A.2: The effect of a cross-track velocity component.

depicted in Fig. A.2. This azimuth displacement should be smaller than a resolution cell. From Fig. A.2, it can be seen that:

$$\tan(\mathrm{d}\theta) = \frac{v_{ct}}{v_{at}} = \frac{\delta Az_{sar}}{R_0}, \tag{A.5}$$

which can be rewritten to obtain the upper bound to the cross-track velocity error:

$$v_{ct} \leq \frac{v_{at}}{R_0}\delta Az_{sar}. \tag{A.6}$$

Cross-Track Acceleration Error

The phase deviation due to cross-track acceleration can be written as:

$$\Delta\varphi = \frac{4\pi}{\lambda}\Delta R = \frac{4\pi}{\lambda}\frac{a_{ct}t^2}{2}. \tag{A.7}$$

From (A.7) it can be seen that cross-track acceleration results in a phase deviation that is proportional to the time squared. Again the maximum of the quadratic phase error occurs at half the SAR observation time, thus with the aid of (A.2), (A.7) can be rewritten as:

$$a_{ct} = \frac{8v_{at}^2\delta Az_{sar}^2}{\pi\lambda R_0^2}\Delta\varphi. \tag{A.8}$$

When a maximum phase deviation of $\pi/4$ is allowed, it follows that:

$$a_{ct} \leq \frac{2v_{at}^2}{\lambda R_0^2}\delta Az_{sar}^2. \tag{A.9}$$

Low-Frequency Sinusoidal Motion Error

Low-frequency sinusoidal motion may be approximated as either linear or quadratic. When the sinusoidal motion is approximately linear, a cross-track velocity component exists. The main effect is therefore a shift of the illuminated area in azimuth direction and the upper bound to the cross-track velocity error is again given by (A.6).

When the sinusoidal motion is approximately quadratic, the main effect is a phase deviation.

The phase deviation depends on the range deviation throughout the SAR observation time. In this case of a sinusoidal flight track, the range deviation can be written as:

$$\Delta R(t) = A_e \cos\big(2\pi f_e t\big), \tag{A.10}$$

where A_e and f_e are the amplitude and the frequency of the sinusoidal motion respectively. The cross-track velocity can be obtained by differentiating the range deviation with respect to time:

$$v_{ct}(t) = \frac{\mathrm{d}\Delta R(t)}{\mathrm{d}t} = -2\pi f_e A_e \sin\big(2\pi f_e t\big), \tag{A.11}$$

and finally the cross-track acceleration can be found by differentiating the cross-track velocity with respect to time:

$$a_{ct}(t) = \frac{\mathrm{d}v_{ct}(t)}{\mathrm{d}t} = -(2\pi f_e)^2 A_e \cos\big(2\pi f_e t\big). \tag{A.12}$$

As can be seen from (A.12) and (A.11), the maximum of the cross-track velocity is equal to the maximum of the cross-track acceleration divided by $2\pi f_e$ (the sine and cosine terms are one). For the cross-track acceleration, an upper limit has already been defined in (A.9). This upper limit can be converted to an upper limit to the cross-track velocity by dividing by $2\pi f_e$:

$$v_{ct} \leq \frac{v^2}{\pi f_e \lambda R_0^2} \delta A z_{sar}^2. \tag{A.13}$$

With the aid of (A.2), (A.13) can be reduced to:

$$v_{ct} \leq \frac{\lambda}{4\pi f_e T_{sar}^2}. \tag{A.14}$$

High-Frequency Sinusoidal Motion Error

High-frequency sinusoidal motion results in paired echoes around the main response. In order to obtain a sidelobe peak level to mainlobe peak level ratio of p, the range deviation should be bounded by:

$$\Delta R \leq \frac{\lambda\sqrt{p}}{2\pi}. \tag{A.15}$$

Following a similar method as in the previous subsection, the upper bound to the cross-track velocity can be found by multiplying (A.15) with $2\pi f_e$:

$$v_{ct} \leq \lambda f_e \sqrt{p}. \tag{A.16}$$

Appendix B

Derivation of the Range Migration Term

In this appendix, the development of the range migration term, expressed in terms of range and Doppler frequency shift, will be given. The development is taken from [99]. Throughout the SAR observation time, the range to the target can be written as:

$$R(Az_n) = \sqrt{R_0^2 + Az_n^2} = R_0 + R_m(Az_n), \tag{B.1}$$

where the azimuth positions Az are defined on the interval $[-\frac{1}{2}L_{sar}, \frac{1}{2}L_{sar}]$. Due to the range migration term R_m, the response of a target may migrate through several range cells during the SAR observation time. In order to focus the final SAR image, the range migration term should therefore be compensated. The compensation can be performed by shifting the range cells in the time domain by using R_m. However, this compensation is only valid for a single point target located in the middle of the SAR image at a range R_0. For any other target, this compensation is not applicable and the image will be geometrically distorted by the compensation.
The relation between the range migration term and the Doppler frequency shift is unique for each target position. The range migration compensation can therefore be carried out in the range-Doppler domain, if the range migration term can be expressed in terms of range and Doppler frequency shift only.
The range migration term can be expressed as:

$$R_m(Az_n) = \sqrt{R_0^2 + Az_n^2} - R_0, \tag{B.2}$$

which can be rewritten as:

$$Az_n = \sqrt{(R_m + R_0)^2 - R_0^2}. \tag{B.3}$$

The Doppler frequency shift given as (note that $Az_n = vT_n$):

$$f_d(Az_n) = \frac{2}{\lambda}\frac{\mathrm{d}R_m}{\mathrm{d}T_n} = \frac{2v}{\lambda}\frac{Az_n}{\sqrt{R_0^2 + Az_n^2}} = \frac{2v}{\lambda}\frac{\sqrt{R_m^2 + 2R_mR_0}}{R_m + R_0}, \tag{B.4}$$

which can be rewritten as:

$$R_m^2\Big(1 - \frac{f_d^2\lambda^2}{4v^2}\Big) + 2R_mR_0\Big(1 - \frac{f_d^2\lambda^2}{4v^2}\Big) - R_0^2\frac{f_d^2\lambda^2}{4v^2} = 0. \tag{B.5}$$

The Doppler frequency shift can also be written as:

$$f_d(Az_n) = \frac{2v}{\lambda}\frac{Az_n}{\sqrt{R_0^2 + Az_n^2}} = \frac{2v}{\lambda}\frac{Az_n}{R} = \frac{2v}{\lambda}\sin\big(\Phi\big), \tag{B.6}$$

or:

$$\sin\big(\Phi\big) = \frac{f_d\lambda}{2v}. \tag{B.7}$$

Subsequently, the substitution of (B.7) into (B.5) results in:

$$R_m^2\cos^2\big(\Phi\big) + 2R_mR_0\cos^2\big(\Phi\big) - R_0^2\Big(1 - \cos^2\big(\Phi\big)\Big) = 0, \tag{B.8}$$

which can be solved for R_m:

$$R_m(R, f_d) = R - R\cos\big(\Phi\big), \tag{B.9}$$

where:

$$\cos\big(\Phi\big) = \sqrt{1 - \Big(\frac{f_d\lambda}{2v}\Big)^2}. \tag{B.10}$$

Appendix C

Derivation of the Range Correlation Factor

In this appendix, the derivation of the range correlation factor will be given.
The range correlation effect has already been studied by many authors, [60]-[63]. In these studies, the range correlation effect is analyzed by assuming that the phase of the oscillator output signal is sinusoidally modulated:

$$s_t(t) = V_t \cos(2\pi f_c t + D_m \sin(2\pi f_m t)), \tag{C.1}$$

where f_m is the frequency offset relative to the carrier and the peak angular deviation D_m is assumed to be small. The echo signal follows as a time-delayed and attenuated version of (C.1):

$$s_r(t) = V_r \cos(2\pi f_c (t - \Delta t) + D_m \sin(2\pi f_m (t - \Delta t))). \tag{C.2}$$

Subsequently, the echo signal is demodulated with a fraction of the transmitted signal, resulting in the beat signal. The phase of the down-conversion component of the beat signal is given as:

$$\varphi_b(t) = 2\pi f_c \Delta t + 2D_m \sin(\pi f_m \Delta t) \cdot \cos(2\pi f_m (t - \frac{\Delta t}{2})). \tag{C.3}$$

From (C.3) can be seen that, after demodulation, the peak angular deviation is modified by:

$$K = 2\sin(\pi f_m \Delta t). \tag{C.4}$$

When the phase noise sidebands of the oscillator's output are thought of as an infinite number of sinusoidal sources, the power spectral density (PSD) of the beat signal can be found by multiplying the original PSD by the range correlation factor K^2.
Thus the phase noise of the beat signal, or *residual phase noise*, is a function of the frequency offset and the time delay (see (C.4)). For short delay times, the residual phase noise power is reduced significantly. This is particularly true for the direct-coupling between the transmitting and receiving antennas.
Thus far, the range correlation factor K was derived by assuming a deterministic model for the oscillator phase noise. However, in practice, noise is a stochastic process. In [64]-[67] another approach is therefore proposed. In this approach, the oscillator phase noise is

represented by a stochastic process.
The LO signal, which is a fraction of the transmitted signal, is defined as:

$$s_{LO}(t) = V_{LO} \exp\left[\,\mathrm{j}2\pi f_c t + \,\mathrm{j}\phi(t)\right], \tag{C.5}$$

in which $\phi(t)$ represents the phase noise. It is assumed that $\phi(t)$ is a stationary stochastic process of zero mean.
The echo signal can again be written as an attenuated and time-delayed version of the transmitted signal:

$$s_r(t) = V_r \exp\left[\,\mathrm{j}2\pi f_c(t-\Delta t) + \,\mathrm{j}\phi(t-\Delta t)\right]. \tag{C.6}$$

Subsequently, the down-conversion component of the beat signal follows as:

$$s_b(t) \approx V_b \exp\left[\,\mathrm{j}2\pi f_c \Delta t\right] \cdot (1 + \,\mathrm{j}\Delta\phi(t)), \tag{C.7}$$

where $\Delta\phi(t)$ is the residual phase noise:

$$\Delta\phi(t) = \phi(t) - \phi(t-\Delta t). \tag{C.8}$$

The approximation made in (C.7) is valid when the variance of the phase noise is small.
Consequently, the PSD of the beat signal (C.7) should be developed. The PSD of the beat signal can be found by applying a Fourier transform to its autocorrelation function. The autocorrelation function of (C.7) is given as:

$$\mathcal{R}_b(\tau) = V_b^2\left(1 + \mathcal{R}_{\Delta\phi}(\tau)\right), \tag{C.9}$$

and subsequently, by applying a Fourier transform to (C.9), the PSD of (C.7) follows as:

$$S_b(f) = V_b^2\delta(f) + V_b^2 S_{\Delta\phi}(f), \tag{C.10}$$

in which $S_{\Delta\phi}$ is the PSD of the residual phase noise. In order to investigate the range correlation effect, the PSD of the residual phase noise $S_{\Delta\phi}$ should now be expressed in terms of the PSD of the original oscillator phase noise S_ϕ.
The autocorrelation function of the residual phase noise is given as:

$$\begin{aligned}\mathcal{R}_{\Delta\phi}(\tau) &= \mathrm{E}\left[\{\phi(t+\tau) - \phi(t-\Delta t+\tau)\}\{\phi(t) - \phi(t-\Delta t)\}\right] \\ &= 2\mathcal{R}_\phi(\tau) - \mathcal{R}_\phi(\tau+\Delta t) - \mathcal{R}_\phi(\tau-\Delta t).\end{aligned} \tag{C.11}$$

The autocorrelation function of the residual phase noise $\mathcal{R}_{\Delta\phi}$ is now expressed in terms of the autocorrelation function of the original oscillator phase noise $\mathcal{R}_\phi$. Subsequently, by applying a Fourier transform to (C.11), the PSD of the residual phase noise is found in terms of the PSD of the oscillator phase noise. The application of a Fourier transform to (C.11) results in:

$$S_{\Delta\phi}(f) = 2S_\phi(f)(1 - \cos(2\pi f\Delta t)) = 4S_\phi(f)\sin^2(\pi f\Delta t). \tag{C.12}$$

From (C.12) can be seen that the PSD of the original oscillator phase noise is modified by K^2 after demodulation with a fraction of the transmitted signal. Thus, the usage of the stochastic model leads to the same range correlation factor.

Appendix D

Calculation of the Error Spectrums of Motion Sensors

In the design stage of the project, an extensive survey of off-the-shelf motion sensors was made, [108]. In order to be able to select a suitable combination of gyroscopes and accelerometers, their performance should be evaluated with the aid of the upper limits set to the different classes of motion errors.
In [92] a method is described to evaluate the performance of motion sensors in terms of the limits set to the different motion errors. In this appendix this method will be briefly reviewed and the selected motion sensors will be evaluated.
Various components contribute to the cross-track velocity depending upon the system configuration. However, the exact system configuration was not yet known at the time that the motion sensors were selected. Throughout the selection process, it was assumed that a 20 cm lever arm would be present between the MC and the APC in the along-track direction. The system configuration is defined in Fig. D.1.
Angular motion gives rise to cross-track velocity components only when the lever arm does not coincide with the axis of rotation. Therefore, in this configuration, platform roll variations do not contribute to the cross-track velocity. Platform yaw and pitch variations induce, on the other hand, cross-track velocity components. If the yaw and pitch variations are assumed to be sinusoidal and by taking the system configuration into account, the cross-track velocity component due to yaw variations can be written as, [87]:

$$v_{ct}^{yw}(t) = 2\pi f_{yw} A_{yw} l_{at} \sin\big(\theta_3\big) \cos\big(2\pi f_{yw} t\big) \qquad [\mathrm{ms}^{-1}], \tag{D.1}$$

in which A_{yw} and f_{yw} are the amplitude and the frequency of the yaw variation respectively and l_{at} is the length of the lever arm.
The cross-track velocity component due to pitch variations follows as, [87]:

$$v_{ct}^{p}(t) = 2\pi f_p A_p l_{at} \cos\big(\theta_3\big) \cos\big(2\pi f_p t\big) \qquad [\mathrm{ms}^{-1}], \tag{D.2}$$

where A_p is the amplitude and f_p is the frequency of the pitch variation.
Lateral motion of the platform also gives rise to cross-track velocity components. Motion in the z-direction is referred to as vertical motion, whereas motion in the y-direction is referred to as horizontal motion.

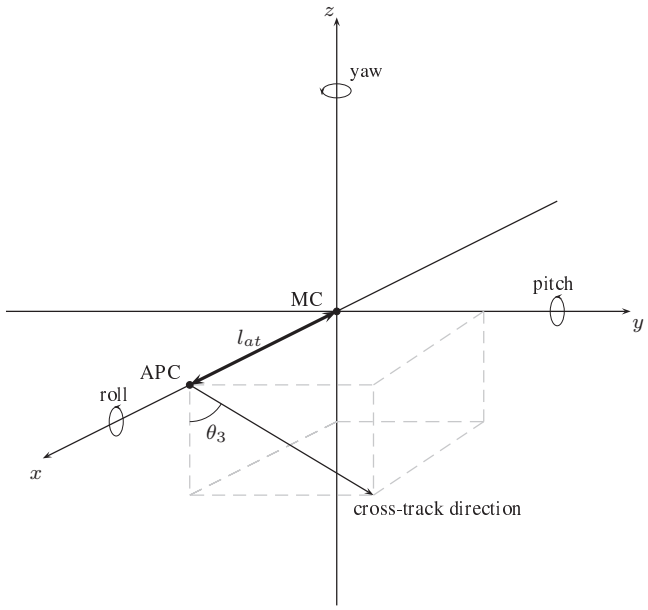

Figure D.1: Definition of the x, y, and z directions and the roll, yaw, and pitch rotation axes. The x-direction coincides with the along-track or azimuth direction, whereas the y-direction coincides with the range direction. The cross-track direction is defined perpendicular to the x-axis in the slant-range plane.

By assuming that the vertical velocity component is sinusoidal, the contribution to the cross-track velocity follows as:

$$v_{ct}^{v}(t) = A_v \cos\big(\theta_3\big) \cos\big(2\pi f_v t\big) \qquad [\mathrm{ms}^{-1}], \tag{D.3}$$

in which A_v and f_v are the amplitude and the frequency of the vertical velocity respectively. If it is assumed that the horizontal velocity is sinusoidal, the cross-track velocity component due to the horizontal velocity component is given as:

$$v_{ct}^{h}(t) = A_h \sin\big(\theta_3\big) \cos\big(2\pi f_h t\big) \qquad [\mathrm{ms}^{-1}], \tag{D.4}$$

where A_h is the amplitude and f_h is the frequency of the horizontal velocity.
Now the bounds defined in (2.21), (2.23), and (2.24) can be used to set upper limits to the amplitudes of (D.1) through (D.4). The upper bounds to the amplitudes as a function of frequency are presented in Fig. 6.2.
Subsequently, the errors in the angle and velocity assessment due to sensor noise and quantization noise should be expressed in terms of a frequency spectrum. When that has been done, the performance of the motion sensors can be evaluated with the aid of the bounds set to the amplitudes of (D.1) through (D.4).

In [89] the power spectral densities of the angle and velocity errors are derived in terms of sensor noise and quantization noise. The PSD of the error in the angle is given as, [89]:

$$\Phi_a(f) = \frac{\Phi_{ng}}{(2\pi f)^2} + \Phi_{aq} \qquad [\mathrm{rad}^2\mathrm{s}], \tag{D.5}$$

in which Φ_{ng} is the random noise of the gyroscope and Φ_{aq} is the angle quantization. The PSD of the error in the lateral velocity components is given as, [89]:

$$\Phi_v(f) = \frac{g^2\Phi_{ng}}{(2\pi f)^4} + \frac{\Phi_{na} + g^2\Phi_{aq}}{(2\pi f)^2} + \Phi_{vq} \qquad [\mathrm{m}^2\mathrm{s}^{-1}], \tag{D.6}$$

where $g = 9.81\,\mathrm{ms}^{-2}$, Φ_{na} is the random noise of the accelerometer, and Φ_{vq} is the velocity quantization.
Subsequently, the power spectral densities of the angle and velocity errors can be compared to the upper limits plotted in Fig. 6.2. However, the bounds are in terms of root mean square (RMS) spectrums. Therefore, the power spectral densities of the different errors should be converted to RMS spectrums. The RMS spectrum can be derived from the PSD by using, [89]:

$$\Phi_{rms} = \sqrt{\frac{\Phi_{psd}}{T_{sar}}}. \tag{D.7}$$

The performance of different combinations of sensors can now be evaluated by calculating the error spectrums. The wide variety of designations and units used by the manufacturers to specify sensor noise complicates this comparison.
Note that this is only a very rough method to investigate the performance of the motion sensors, [87]. Since the different motion components are assumed to be sinusoidal, the effect of wideband motion is not taken into consideration. Moreover, the combined effect of angular and lateral motion is not taken into account.

Bibliography

[1] H. D. Griffiths, "Synthetic Aperture Processing for Full-Deramp Radar Altimeters," *Electronic Letters,* vol. 24, no. 7, pp. 371-373, Mar. 1988.

[2] B. Purseyyed and H. D. Griffiths, "A Synthetic Aperture Altimeter," in *Proc. IEEE Int. Geoscience Remote Sensing Symp. IGARSS '88,* Edinburgh, Scotland, 13-16 Sep., 1988, pp. 981-982.

[3] H. D. Griffiths, "New Ideas in FM Radar," *Electronics and Communication Engineering Journal,* pp. 185-194, Oct. 1990.

[4] N. A. Cheadle, W. Lewis, H. Lee, and R. A. York, "Calibration of a Wideband FMCW Radar Used for Microwave SAR Imaging," in *Proc. 28^{th} Asilomar Conf. Signals, Systems, Computers '94,* Pacific Grove, U.S.A., 31 Oct.-2 Nov., 1994, vol. 1, pp. 141-144.

[5] C. Chatzakis and N. K. Uzunoglu, "Analysis of a Head-On Looking SAR," in *Proc. 4^{th} European Conf. Synthetic Aperture Radar EUSAR '02,* Cologne, Germany, 4-6 Jun., 2002, pp. 489-492.

[6] H. D. Griffiths, "Conceptual Design of an Ultra High-Resolution mm-Wave Synthetic Aperture Radar," in *Proc. IEEE Radar Conf. '96,* Ann Arbor, U.S.A., 13-16 May, 1996, pp. 255-260.

[7] G. Connan, H. D. Griffiths, and P. V. Brennan, "FMCW-SAR Development for Internal Wave Imaging," in *Proc. MTS/IEEE OCEANS '97,* Halifax, Canada, 6-9 Oct., 1997, vol. 1, pp. 73-78.

[8] G. Connan, H. D. Griffiths, P. V. Brennan, D. Renouard, E. Barthlmy, and R. Garello, "Experimental Imaging of Internal Waves by a mm-Wave Radar," in *Proc. MTS/IEEE OCEANS '98,* Nice, France, 28 Sep.-1 Oct., 1998, vol. 2, pp. 619-623.

[9] G. Connan, H. D. Griffiths, P. V. Brennan, and R. Garello, "W-Band Radar Measurements of Laboratory Water Waves," in *Proc. MTS/IEEE OCEANS '99,* Seatlle, U.S.A., 13-16 Sep., 1999, vol. 3, pp. 1333-1337.

[10] G. Connan, R. Garello, H. D. Griffiths, and P. V. Brennan, "Millimeter-Wave Radar Back-Scattering from Water Waves," in *Proc. IEEE Int. Radar Conf. '00,* Alexandria, U.S.A., 7-12 May, 2000, pp. 347-351.

[11] M. Soumekh, "FM-CW SAR and Phased Array Spatial-Velocity Imaging," in *Proc. Int. Conf. Image Processing ICIP '94,* Austin, U.S.A., 13-16 Nov., 1994, vol. 1, pp. 471-475.

[12] M. Soumekh, *Fourier Array Imaging*. Englewood Cliffs: Prentice Hall Inc., 1994.

[13] M. Soumekh, "Airborne Synthetic Aperture Acoustic Imaging," *IEEE Trans. Image Processing,* vol. 6, no. 11, pp. 1545-1554, Nov. 1997.

[14] M. Soumekh, "Bistatic Synthetic Aperture Radar Imaging Using Wide-Bandwidth Continuous Wave Sources," in *Proc. SPIE Conf. Radar Processing, Technology, and Applications III,* San Diego, U.S.A., Jul. 1998, pp. 99-109.

[15] M. Soumekh, "Wide-Bandwidth Continuous-Wave Monostatic/Bistatic Synthetic Aperture Radar Imaging," in *Proc. Int. Conf. Image Processing ICIP '98,* Chicago, U.S.A., 4-7 Oct., 1998, vol. 3, pp. 361-365.

[16] Y. Yamaguchi, M. Sengoku, T. Abe, W. M. Boerner, "FM-CW Radar Applied to the Detection of Buried Objects in Snowpack," *IEEE Antennas and Propagation Society Int. Symp. Digest,* vol. 2, 1990, pp. 738-741.

[17] Y. Yamaguchi, Y. Maruyama, A. Kawakami, M. Sengoku, and T. Abe, "Detection of Objects Buried in Wet Snowpack by an FM-CW Radar," *IEEE Trans. Geosci. Remote Sensing,* vol. 29, no. 2, pp. 201-208, Mar. 1991.

[18] Y. Yamaguchi, M. Mitsumoto, M. Sengoku, and T. Abe, "Human Body Detection in Wet Snowpack by an FM-CW Radar," *IEEE Trans. Geosci. Remote Sensing,* vol. 30, no. 1, pp. 186-189, Jan. 1992.

[19] Y. Yamaguchi, M. Mitsumoto, A. Kawakami, M. Sengoku, and T. Abe, "Detection of Objects by Synthetic Aperture FM-CW Radar," *Electronics and Communications in Japan,* part 1, vol. 75, no. 3, pp. 85-93, 1992.

[20] Y. Yamaguchi, M. Mitsumoto, M. Sengoku, and T. Abe, "Synthetic Aperture FM-CW Radar Applied to the Detection of Objects Buried in Snowpack," *IEEE Antennas and Propagation Society Int. Symp. Digest,* vol. 2, 1992, pp. 1122-1125.

[21] Y. Yamaguchi, T. Nishikawa, W. M. Boerner, M. Sengoku, and H. J. Eom, "On Radar Polarimetry in FM-CW Radar," in *Proc. IEEE Int. Geoscience Remote Sensing Symp. IGARSS '93,* Tokyo, Japan, 18-21 Aug., 1993, vol. 2, pp. 368-370.

[22] Y. Yamaguchi, M. Mitsumoto, M. Sengoku, and T. Abe, "Synthetic Aperture FM-CW Radar Applied to the Detection of Objects Buried in Snowpack," *IEEE Trans. Geosci. Remote Sensing,* vol. 32, no. 1, pp. 11-18, Jan. 1994.

[23] Y. Yamaguchi, T. Nishikawa, M. Sengoku, W. M. Boerner, and H. J. Eom, "Fundamental Study on Synthetic Aperture FM-CW Radar Polarimetry," *IEICE Trans. Commun.,* vol. E77-B, no. 1, pp. 73-80, Jan. 1994.

[24] Y. Yamaguchi, T. Nishikawa, M. Sengoku, and W. M. Boerner, "2-D Polarimetric Imaging by an FM-CW Radar," *IEEE Antennas and Propagation Society Int. Symp. Digest,* vol. 3, 1994, pp. 1998-2003.

[25] Y. Yamaguchi, T. Nishikawa, M. Sengoku, and W. M. Boerner, "Two-Dimensional and Full Polarimetric Imaging by a Synthetic Aperture FM-CW Radar," *IEEE Trans. Geosci. Remote Sensing,* vol. 33, no. 2, pp. 421-427, Mar. 1995.

[26] Y. Yamaguchi and T. Moriyama, "Polarimetric Detection of Objects Buried in Snowpack by a Synthetic Aperture FM-CW Radar," *IEEE Trans. Geosci. Remote Sensing,* vol. 34, no. 1, pp. 45-51, Jan. 1996.

[27] Y. Yamaguchi, M. Nakamura, and H. Yamada, "Decomposition of Radar Target Based on the Scattering Matrix Obtained by FM-CW Radar," *IEICE Trans. Commun.,* vol. E80-B, no. 10, pp. 1564-1569, Oct. 1997.

[28] T. Moriyama, Y. Yamaguchi, and H. Yamada, "Three-Dimensional Fully Polarimetric Imaging in Snowpack by a Synthetic Aperture FM-CW Radar," *IEICE Trans. Commun.,* vol. E83-B, no. 9, pp. 1963-1968, Sep. 2000.

[29] A. Meta and P. Hoogeboom, "High Resolution Airborne FM-CW SAR: Digital Signal Processing Aspects," in *Proc. IEEE Int. Geoscience Remote Sensing Symp. IGARSS '03,* vol. VI, Toulouse, France, 21-25 Jul., 2003, pp. 4074-4076.

[30] A. Meta and P. Hoogeboom, "Time Analysis and Processing of FM-CW SAR Signals," in *Proc. Int. Radar Symp. IRS '03,* Dresden, Germany, 30 Sep.-2 Oct., 2003, pp. 263-268.

[31] A. Meta and P. Hoogeboom, "High resolution Airborne FM-CW SAR: Preliminary Results," in *Proc. 5^{th} European Conf. Synthetic Aperture Radar EUSAR '04,* Ulm, Germany, 25-27 May, 2004, pp. 183-186.

[32] L. P. Ligthart and L. R. Nieuwkerk, "FM-CW Delft Atmospheric Research Radar," *IEE Proc. Part F,* vol. 127, no. 6, pp. 421-426, Dec. 1980.

[33] L. P. Ligthart and L. R. Nieuwkerk, "An X-Band Solid-State FM-CW Weather Rader," *IEE Proc. Part F,* vol. 137, no. 6, pp. 418-426, Dec. 1990.

[34] S. H. Heijnen, W. F. van der Zwan, and L. P. Ligthart, "Technical Aspects of a New S-Band Atmospheric Profiler," in *Proc. 31^{st} European Microwave Conf. EUMC '01,* London, United Kingdom, 25-27 Sep., 2001.

[35] P. Hoogeboom, P. Snoeij, P. J. Koomen, and H. Pouwels, "The PHARUS Project, Results of the Definition Study including the SAR Testbed PHARS," *IEEE Trans. Goesci. Remote Sensing,* vol. 30, no. 4, pp. 723-735, Jul. 1992.

[36] M. P. G. Otten and J. S. Groot, "Development of a Generic SAR Processor in the Netherlands," in *Proc. 1^{st} Int. Airborne Remote Sensing Conf. and Exhibition '94,* Strasbourg, France, 12-15 Sep., 1994, vol. II, pp. 338-345.

[37] M. P. G. Otten, "Extending the Capabilities of the PHARUS System," in *Proc. 3 rd European Conf. Synthetic Aperture Radar EUSAR '00,* Munich, Germany, 23-25 May, 2000, pp. 801-804.

[38] P. Steeghs, D. van Halsema, and P. Hoogeboom, "MINISAR: a Miniature, Lightweight, Low Cost, Scalable SAR System," in *Proc. CEOS SAR Calibration/Validation Workshop '01,* Tokyo, Japan, 2-5 Apr., 2001, pp. 125-128.

—Chapter 2—

[39] F. J. Harris, "On the use of Windows for Harmonic Analysis with Discrete Fourier Transform," *Proc. IEEE,* vol. 66, no. 1, pp. 51-83, Jan. 1978.

[40] M. I. Skolnik, *Introduction to Radar Systems*, London: McGraw-Hill Inc., 1980.

[41] A. G. Stove, "Linear FM-CW Radar Techniques," *IEE Proc. Part F Radar Signal Process.,* vol. 139, no. 5, pp. 343-350, Oct. 1992.

[42] A. G. Stove, "Erratum to Linear FM-CW Radar Techniques," *IEE Proc. Part F Radar Signal Process.,* vol. 140, no. 2, pp. 137, 1992.

[43] K. S. Kulpa, "Novel Method of Decreasing Influence of Phase Noise on FM-CW Radar," in *Proc. CIE Int. Conf. Radar '01,* 15-18 Oct., 2001, pp. 319-323.

[44] T. H. Lee, "Oscillator Phase Noise: a Tutorial," in *Proc. IEEE Custom Integrated Circuits Conf. '99,* San Diego, U.S.A., 16-19 May, 1999, pp. 373-380.

[45] J. L. Stewart, "Frequency Modulation Noise in Oscillators," *Proc. IRE,* vol. 44, pp. 372-376, Mar. 1956.

[46] W. A. Edson, "Noise in Oscillators," *Proc. IRE,* vol. 48, pp. 1454-1466, Aug. 1960.

[47] J. A. Mullen, "Background Noise in Nonlinear Oscillators," *Proc. IRE,* vol. 48, pp. 1467-1473, Aug. 1960.

[48] E. Hafner, "The Effects of Noise in Oscillators," *Proc. IEEE,* vol. 54, no. 2, pp. 179-198, Feb. 1966.

[49] S. Hamilton, "FM and AM Noise in Microwave Oscillators," *Microwave Journal*, vol. 21, pp. 105-109, Jun. 1978.

[50] H. D. Griffiths, "The Effect of Phase and Amplitude Errors in FM Radar," in *Proc. IEE Colloquium High Time-Bandwidth Product Waveforms in Radar and Sonar,* 1 May, 1991, pp. 9/1-9/5.

[51] P. van Genderen, "The Effect of Phase Noise in a Stepped Frequency Continuous Wave Ground Penetrating Radar," in *Proc. CIE Int. Conf. Radar '01,* Beijing, China, 15-18 Oct., 2001, pp. 581-584.

[52] M. E. Adamski, K. S. Kulpa, M. Nałęcz, A. Wojtkiewicz, "Phase Noise in Two-Dimensional Spectrum of Video Signal in FM-CW Homodyne Radar," in *Proc. XIIIth Int. Conf. Microwaves Radar Wireless Communications MIKON '00,* Wrocław, Poland, 22-24 May, 2000, vol. 2, pp. 645-648.

[53] K. V. Puglia, "Phase Noise Analysis of Component Cascades," in *IEEE Microwave,* vol. 3, no. 4, pp. 71-75, Dec. 2002.

[54] D. B. Leeson, "A Simple Model of Feedback Oscillator Noise Spectrum," *Proc. IEEE,* vol. 54, pp. 329-330, Feb. 1966.

[55] G. Sauvage, "Phase Noise in Oscillators: a Mathematical Analysis of Leeson's Model," *IEEE Trans. Instrum. Meas.,* vol. 26, no. 4, pp. 408-410, Dec. 1977.

[56] A. Hajimiri and T. H. Lee, "A General Theory of Phase Noise in Electrical Oscillators," *IEEE J. Solid-State Circuits,* vol. 33, no. 2, pp. 179-194, Feb. 1998.

[57] M. K. Nezami, "Evaluate the Impact of Phase Noise on Receiver Performance," *Microwaves & RF*, pp. 165-172, May 1998.

[58] A. Hajimiri and T. H. Lee, "Corrections to: A General Theory of Phase Noise in Electrical Oscillators," *IEEE J. Solid-State Circuits,* vol. 33, no. 6, pp. 928, Jun. 1998.

[59] T. H. Lee and A. Hajimiri, "Oscillator Phase Noise: a Tutorial," *IEEE J. Solid-State Circuits,* vol. 35, no. 3, pp. 326-336, Mar. 2000.

[60] W. P. Robins, *Phase Noise in Signal Sources,* London: Peter Peregrinus, 1982.

[61] S.J. Goldman, "Oscillator Phase Noise Proves Important to Pulse-Doppler Radar Systems," *J. Microwave Systems News,* vol. 14, no. 2, pp. 88-100, Feb. 1984.

[62] S.J. Goldman, "Analyze Effects of System Delay Lines," *Microwaves & RF,* vol. 26, no. 6, pp. 149-156, Jun. 1987.

[63] S.J. Goldman, *Phase Noise Analysis in Radar Systems using Personal Computers,* New York: John Wiley and Sons, 1989.

[64] R. S. Raven, "Requirements on Master Oscillators for Coherent Radar," *Proc. IEEE,* vol. 54, no. 2, pp. 237-243, Feb. 1966.

[65] M. P. Burt and M. C. Budge, "Range Correlation Effects on Phase Noise Spectra," in *Proc. 25th Southeastern Symp. System Theory SSST '93,* Tuscaloosa, U.S.A., 7-9 Mar., 1993, pp. 492-496.

[66] M. C. Budge and M. P. Burt, "Range Correlation Effects in Radars," in *Proc. IEEE Nat. Radar Conf. '93,* Lynnfield, 20-22 Apr., 1993, pp. 212-216.

[67] M. C. Budge and M. P. Burt, "Range Correlation Effects on Phase and Amplitude Noise," in *Proc. Southeastcon '93,* 1993.

[68] R. A. Strangeway, T. Koryu Ishii, and J. S. Hyde, "Low-Phase-Noise Gunn Diode Oscillator Design," *IEEE Trans. Microwave Theory Tech.,* vol. 36, no. 4, pp. 792-794, Apr. 1988.

[69] M. Vossiek, T. .v. Kerssenbrock, and P. Heide, "Signal Processing Methods for Millimetrewave FMCW Radar with High Distance and Doppler Resolution," in *Proc. 27^{th} European Microwave Conf. EUMC 97,* 1997, vol. 2, pp. 1127-1132.

[70] M. Vossiek, T. v. Kerssenbrock, and P. Heide, "Novel Nonlinear FM-CW Radar for Precise Distance and Velocity Measurements," in *Proc. IEEE MTT-S Int. Microwave Symp. Digest,* Baltimore, U.S.A., 7-12 Jun., 1998, vol. 2, pp. 511-514.

[71] Z. Zhu, W. Yu, X. Zhang, and X. Qiu, "A Correction Method to Distortions in FM-CW Imaging System," in *Proc. IEEE Aerospace Electronics Conf. NEACON '96,* Dayton, U.S.A., 20-23 May, 1996, vol. 1, pp. 323-326.

[72] S. O. Piper, "FM-CW Range Resolution for MMW Seeker Applications," in *Proc. Southeastcon '90,* New Orleans, U.S.A., 1-4 Apr., 1990, pp. 156-160.

[73] S. O. Piper, "Homodyne FM-CW Radar Range Resolution Effects with Sinusoidal Nonlinearities in the Frequency Sweep," in *Proc. IEEE Int. Radar Conf. '95,* Alexandria, U.S.A., 8-11 May, 1995, pp. 563-567.

[74] W. D. Jing, H. Xiang, and R. W. Jie, "Analysis of the Influence of the FM Nonlinearity on the Range Resolution of LFMCW Radar," in *Proc. Asia Pacific Microwave Conf. APMC '99,* Singapore, 30 Nov.-3 Dec., 1999, vol. 3, pp. 714-717.

[75] K. S. Kulpa, A. Wojtkiewicz, M. Nałęcz, and J. Misiurewicz, "The Simple Method for Analysis of Nonlinear Frequency Distortions in FM-CW Radar," in *Proc. $XIII^{th}$ Int. Conf. Microwaves Radar Wireless Communications MIKON '00,* Wrocław, Poland, 22-24 May, 2000, vol. 1, pp. 235-238.

[76] M. Pichler, A. Stelzer, P. Gulden, and M. Vossiek, "Influence of Systematic Frequency-Sweep Nonlinearity on Object Distance Estimation in FM-CW/FS-CW Radar Systems," in *Proc. 33^{rd} European Microwave Conf. EUMC '03,* Munich, Germany, 7-9 Oct., 2003, vol. 3, pp. 1203-1206.

[77] H.-G. Park, B. Kim, and Y.-S. Kim, "VCO Nonlinearity Correction Scheme for a Wideband FM-CW Radar," *Microwave and Optical Technology Letters,* vol. 25, no. 4, pp. 266-269, May 2000.

[78] M. Christmann, M. Vossiek, M. Smith, and G. Rodet, "SAW Based Delay Locked Loop Concept for VCO Linearization in FM-CW Radar Sensors," in *Proc. 33^{rd} European Microwave Conf. EUMC '03,* Munich, Germany, 7-9 Oct., 2003, vol. 3, pp. 1135-1138.

[79] J. A. Scheer, and J. L. Kurtz, *Coherent radar performance estimation*, Boston: Artech House Inc., 1993.

[80] S. O. Piper, "FM-CW Linearizer Bandwidth Requirements," in *Proc. IEEE Nat. Radar Conf. '91,* Los Angeles, U.S.A., 12-13 Mar., 1991, pp. 142-146.

[81] S. O. Piper, "Receiver Frequency Resolution for Range Resolution in Homodyne FM-CW Radar," in *Proc. Nat. Telesystems Conf. '93,* Atlanta, U.S.A., 16-17 Jun., 1993, pp. 169-173.

[82] N. Levanon, *Radar Principles,* New York: John Wiley, 1988.

[83] W. G. Carrara, R. S. Goodman, and R. M. Majewski, *Spotlight Synthetic Aperture Radar,* Boston: Artech House Inc., 1995.

[84] D. J. DiFilippo, G. E. Haslam, W. S. Widnall, "Evaluation of a Kalman Filter for SAR Motion Compensation," in *Proc. IEEE Position, Location, Navigation Symp. PLANS '88,* Orlando, U.S.A., 29 Nov.-2 Dec., 1988, pp. 259-268.

[85] T. A. Kennedy, "The Design of SAR Motion Compensation Systems Incorporating Strapdown Inertial Measurement Units," in *Proc. IEEE Nat. Radar Conf. '88,* Ann Arbor, U.S.A., 20-21 Apr., 1988, pp. 74-78.

[86] T. A. Kennedy, "Strapdown Inertial Measurement Units for Motion Compensation for Synthetic Aperture Radars," *IEEE Aerosp. Electron. Syst. Mag.,* vol. 3, no. 10, pp. 32-35, Oct. 1988.

[87] G. van der Burg, "SAR Image Degradation by Motion Induced Phase Errors," National Aerospace Laboratory, Amsterdam, Tech. Rep. NLR-CR-90164-L, 1990.

[88] T. A. Kennedy, "A Technique for Specifying Navigation System Performance Requirements in SAR Motion Compensation Applications," in *Proc. Nat. Radar Conf. '91,* Los Angeles, U.S.A., 12-13 Mar., 1991, pp. 118-126.

[89] J. H. Breeman, "Motion Compensation for SAR using an Inertial System," National Aerospace Laboratory, Amsterdam, Tech. Rep. NLR-CR-91419-L, 1991.

[90] S. Buckreuss, "Motion Compensation for Airborne SAR based on Inertial Data, RDM, and GPS," in *Proc. IEEE Int. Geoscience Remote Sensing Symp. IGARSS '94,* Pasadena, U.S.A., 1994, vol. 4, pp. 1971-1973.

[91] S. Méric and G. Chassay, "Investigations of Image Quality Parameters, Applications for Motion Estimation," in *Proc. 2nd European Conf. Synthetic Aperture Radar EUSAR '98,* Friedrichshafen, Germany, 25-27 May, 1998, pp. 149-152.

[92] M. R. Muller, "Keuze IMU-sensoren ten behoeve van baanbepaling MiniSAR," TNO Physics and Electronics Laboratory, The Hague, Tech. Rep. FEL-02-S139, May 2002.

—Chapter 3—

[93] L. W. Couch, *Digital and Analog Communication Systems*, New York: Macmillan Publishing Company, 1993.

[94] J. C. Kirk, "Imaging Radar," State of the Art Limited, Course Documentation, Feb. 1988.

[95] E. J. Kelly and R. P. Wishner, "Matched-Filtering Theory for High-Velocity, Accelerating Targets, *IEEE Trans. Mil. Electron.,* vol. 9, no. 1, pp. 56-69, Jan. 1965.

[96] D. E. Barrick, "FM-CW Radar Signals and Digital Processing," National Oceanic and Atmospheric Administration, Boulder, Tech. Rep. AD-774-829, Jul. 1973.

—Chapter 4—

[97] R. Bamler, "A Comparison of Range-Doppler and Wavenumber Domain SAR Focusing Algorithms," *IEEE Trans. Geosci. Remote Sensing,* vol. 30, no. 4, pp. 706-713, Jul. 1992.

[98] A. M. Smith, "A New Approach to Range-Doppler SAR Processing," *Int. J. Remote Sensing,* vol. 12, no. 2, pp. 235-251, 1991.

[99] W. L. van Rossum and M. P. G. Otten, "High Resolution SAR," TNO Physics and Electronics Laboratory, The Hague, Tech. Rep. FEL-01-A156, Jun. 2001.

[100] C. V. Jakowatz, D. E. Wahl, P. H. Eichel, D. C. Ghiglia, P. A. Thompson, *Spotlight-Mode Synthetic Aperture Radar: a Signal Processing Approach,* Boston: Kluwer Academic Publishers, 1996.

—Chapter 5—

[101] A. W. M. van den Enden and N. A. M. Verhoeckx, *Discrete-Time Signal Processing, an Introduction,* Englewood Cliffs: Prentice Hall Inc., 1989.

[102] "FFT Window Functions," Bores Signal Processing, Surrey, Tech. Note. Available: http://www.bores.com/

[103] G. R. Curry, *Radar System Performance Modelling,* Boston: Artech House Inc., 2001.

—Chapter 6—

[104] J. J. M. de Wit, "Description and First Evaluation of the FM-CW SAR Demonstrator System," TU Delft - IRCTR, Delft, Tech. Rep. IRCTR-S-010-04, Jan. 2004.

[105] J. J. M. de Wit and P. Hoogeboom, "SAR: a Novel Application for FM-CW Radars," in *Proc. 31st European Microwave Conf. EUMC '01,* London, United Kingdom, 25-27 Sep., 2001, vol. 3, pp. 51-54.

[106] J. J. M. de Wit and P. Hoogeboom, "High-Resolution Airborne FM-CW SAR: Design and Processing Aspects," in *Proc. 4th European Conf. Synthetic Aperture Radar EUSAR '02,* Cologne, Germany, 4-6 Jun., 2002, pp. 163-166.

[107] "GPS World Receiver Survey," *J. GPS World,* pp. 28-42, Jan. 2002.

[108] D. Ribeiro and I. Gulmus, "Radar aardobservatie," TU Delft - IRCTR, Delft, Tech. Rep. IRCTR-A-18-02 HTS, Jun. 2002.

[109] J. F. M. Lorga, Q. P. Chu, and J. A. Mulder, "Tightly-Coupled IMU/GPS Carrier-Phase Navigation System," in *Proc. ION 2003 National Technical Meeting,* Anaheim, U.S.A., 22-24 Jan., 2003, pp. 385-396.

[110] J. F. M. Lorga, W. L. van Rossum, D. van Halsema, Q. P. Chu, and J. A. Mulder, "The Development of a SAR Dedicated Navigation System: From Scratch to the First Test Flight," in *Proc. IEEE Position, Location, Navigation Symp. PLANS '04,* Monterey, U.S.A., 26-29 Apr., 2004, pp. 249-258.

[111] J. F. M. Lorga, Q. P. Chu, W. L. van Rossum, and J. A. Mulder, "Developing and Testing a Tightly Coupled GPS/IMU Navigation System," in *Proc. ESA Workshop Satellite Navigation User Equipment Navitec '04,* Noordwijk, the Netherlands, 8-10 Dec., 2004.

[112] H. Duiker and R. Brouwers, "Softwareontwikkeling voor dataopslag en aansturing van een FM-CW SAR prototype," TU Delft - IRCTR, Delft, Tech. Rep. IRCTR-AH-002-03, Jan. 2003.

[113] D. Kalloemisier, "Remote control software voor de FM-CW SAR demonstrator," TU Delft - IRCTR, Delft, Tech. Rep. IRCTR-SH-013-03, Jun. 2003.

—Chapter 7—

[114] K. Sarabandi, L. E. Pierce, Y. Oh, M. C. Dobson, F. T. Ulaby, A. Freeman, and P.Dubois, "Cross-Calibration Experiment of JPL AIRSAR and Truck-Mounted Polarimetric Scatteromter," *IEEE Trans. Geosci. Remote Sensing,* vo. 32, no. 5, pp. 975-985, Sep. 1994.

—Chapter 8—

[115] "94 GHz FMCW Radar Module Part No. FMCW-10/94/200/10," Elva-1, St. Petersburg, Tech. Note., Dec. 2001. Available: http://www.elva-1.spb.ru/

[116] A. G. Stove, "Modern FMCW Radar - Techniques and Applications," in *Proc. 1st European Radar Conf. EuRAD '04,* Amsterdam, the Netherlands, 14-15 Oct., 2004, pp. 149-152.

[117] A. Elterich and R. Schmalenberger, "FM-CW mmW Radar Seeker," in *Proc. Int. Radar Symp. IRS '03,* Dresden, Germany, 30 Sep.-2 Oct., 2003, pp. 475-480.

[118] M. Nałęcz, K. Kulpa, R. Rytel-Andrianik, S. Plata, and B. Dawidowicz, "Data Recording and Processing in FM-CW SAR System," in *Proc. Int. Radar Symp. IRS '04,* Warszawa, Poland, 19-21 May, 2004, pp. 171-175.

[119] M. Edrich, "A High-Resolution Millimeter-Wave FMCW Airborne SAR with Minimum SWP," in *Proc. 5th European Conf. Synthetic Aperture Radar EUSAR '04,* Neu-Ulm, Germany, 25-27 May, 2004, vol. 1, pp. 287-290.

[120] M. Edrich, "Design Overview and Flight Test Results of the Miniaturised SAR Sensor MISAR," in *Proc. 1st European Radar Conf. EuRAD '04,* Amsterdam, the Netherlands, 14-15 Oct., 2004, pp. 205-208.

[121] A. Meta and P. Hoogeboom, "Development of Signal Processing Algorithms for High Resolution Airborne Millimeter Wave FMCW SAR," in *Proc. IEEE Int. Radar Conf. '05,* Arlington, U.S.A., 9-12 May, 2005. To be published.

[122] J. Figueras i Ventura, "Design of a Small, Low Cost, P-Band Airborne Polarimetric Synthetic Aperture Radar," TU Delft - IRCTR, Delft, Tech. Rep. IRCTR-A-005-04, Feb. 2004.

[123] J. Figueras i Ventura and P. Hoogeboom, "Design of a Small, Low Cost, P-Band Airborne Polarimetric Synthetic Aperture Radar," in *Proc. 1st European Radar Conf. EuRAD '04,* Amsterdam, the Netherlands, 14-15 Oct., 2004, pp. 213-216.

Acknowledgment

I would like to express my gratitude to all the colleagues at the IRCTR and at TNO Defence, Security, and Safety who helped me in one way or another.

First of all, I would like to thank my promotors prof. ir. P. Hoogeboom and prof. dr. ir. L. P. Ligthart for giving me the opportunity to carry out my Ph.D. work at the IRCTR and for keeping me on track throughout the years.

I am especially indebted to P. Hakkaart and W. F. van der Zwan for their crucial contribution to the ground-based measurements and the airborne experiments. In addition, I would like to thank ir. P. J. F. Swart, ir. M. P. G. Otten, and dr. W. L. van Rossum for their day-by-day guidance and for patiently answering numerous questions. Furthermore, I really appreciated working together with A. Meta M.Sc. and J. F. M. Lorga M.Sc., during office hours and after. Finally, I would like to thank dr. ir. R. F. Bloemenkamp for reviewing my thesis.

The following students completed their internship or graduation assignment within the framework of the project: Irfan Gulmus, Danny Ribeiro, Hans Duiker, Remco Brouwers, Dinesh Kalloemisier, and (at TNO) Maurits Muller. Their work has been a great contribution.